UNIWERSYTET IM. ADAMA MICKIEWICZA
W POZNANIU

Spin-Dependent Transport in Magnetic Nanostructures with Coulomb Blockade

Ireneusz Weymann

Rozprawa doktorska

Promotor: prof. dr hab. Józef Barnaś

Zakład Fizyki Mezoskopowej
Wydział Fizyki
Uniwersytet im. Adama Mickiewicza w Poznaniu

Poznań 2005

Abstract

The present thesis is devoted to transport in magnetic nanostructures with Coulomb blockade. In the first part spin-polarized transport in ferromagnetic single-electron transistors and double-island devices is analyzed in the sequential tunneling regime. The considerations are based on the master equation method. In calculations nonequilibrium spin accumulation is also taken into account. In the case of nonmagnetic islands it is shown that spin accumulation is crucial for occurrence of nonzero tunnel magnetoresistance. Nonequilibrium spin accumulation is also responsible for existence of negative differential conductance in transport characteristics of double-island devices. Furthermore, it is shown that the numerical results are in good agreement with experimental data.

In the second part transport through quantum dots coupled to ferromagnetic leads is analyzed by means of the real-time diagrammatic technique in the whole range of parameters. In calculations both the first-order and second-order tunneling processes are taken into account. It is shown that the behavior of tunnel magnetoresistance depends strongly on transport regimes, indicating different spin accumulation mechanisms. Moreover, a new zero-bias anomaly in differential conductance for antiparallel alignment of leads' magnetizations is found in the cotunneling regime for quantum dots occupied by a single electron. The anomalous behavior of conductance leads in turn to minimum in tunnel magnetoresistance at low bias voltage. The influence of intrinsic spin relaxation on the dot on transport characteristics in the cotunneling regime is also analyzed. Furthermore, the cotunneling transport in the case of quantum dot coupled to ferromagnetic leads with magnetic moments aligned arbitrarily with respect to each other is analyzed by means of the second-order perturbation theory.

Contents

Chapter 1

Introduction

1.1 Motivation

More than one century has elapsed since the discovery of a small negatively charged *corpuscule* by Joseph John Thomson [1] in 1897. The corpuscule, afterwards called an electron, carries an elementary charge of $-e$, with $e = 1.6019 \times 10^{-19}$ C, measured for the first time by Robert Millikan [2] in 1911. This property of electrons is permanently used in all conventional electronic devices, regardless of their size.

Recently, one can observe a common pursuit towards the miniaturization of electronic systems. According to the Moore's law the number of transistors per microchip is doubled every three years. It is however expected that the possibility of further miniaturization will be stopped due to the loss of chips' stability when the device components achieve critical dimensions in the nanometer range. Thus, the most challenging task facing contemporary science and technology is to implement structures, alternative to the silicon-based devices, whose extensions could be reduced substantially. *Mesoscopic* physics is a field of physics dealing with such *nanostructures* [3, 4, 5, 6, 7, 8, 9, 10]. This field is governed by a sensitive balance between the macroscopic physics described by classical mechanics and the microscopic physics, to which quantum mechanics is applied. The nanostructures consist generally of a central *mesoscopic* part coupled through tunnel barriers to external reservoirs. The central part can be molecules, metallic *nanograins*, metallic *islands* or *quantum dots*.

Electrons, fortunately, carry not only the elementary charge but also the spin. The concept of *spinning* electrons was first introduced by George Uhlenbeck and Abraham Goudsmit [11] in 1925. Whereas, in 1927 Paul Dirac [12] included systematically the electron spin in quantum mechanics. The electron spin provides an additional degree of freedom, which considerably broadens the range of applications and novel device proposals. This is especially promising for nanostructures in which some of the electrodes are made of ferromagnetic material.

The spin-based nanoelectronics – *spintronics* concerns a relatively new area of mesoscopic physics dealing with the interplay of charge and spin degrees of freedom [13, 14, 15, 16, 17, 18]. Although there is a great number of both theoretical and experimental works on the spintronic properties of mesoscopic systems, this flied is still not fully explored.

The goal of the present thesis is therefore to broaden the insight and gain the comprehension of transport properties of magnetic nanostructures with Coulomb blockade, in principal, ferromagnetic single-electron tunneling devices and quantum dots coupled to ferromagnetic leads.

1.2   Basic Concepts

In this dissertation the nanostructures in which transport takes place by tunneling processes are considered. Furthermore, because of extremely small dimensions of the central electrode, some novel effects can be observed in the corresponding transport characteristics.

1.2.1   Single-Electron Charging Effects

The central part is characterized by its charging energy, which corresponds to the energy needed for adding a single electron on it. If the charging energy is the most relevant energy scale, the system exhibits the *single-electron charging effects* [4, 19, 20, 21, 22, 23, 24, 25]. An electron can tunnel on the central electrode only when the energy provided by the transport voltage surpasses the corresponding charging energy. Otherwise, the current is exponentially suppressed and the system is in the *Coulomb blockade regime* [3, 26, 27]. Once the bias voltage is larger than the threshold voltage, the electrons can tunnel one by one through the system leading to the step-like current-voltage characteristics – *Coulomb staircase*, or the sawtooth-like gate voltage dependence of electric current – *Coulomb oscillations* [4, 19, 20, 23, 28].

In the considerations, henceforth, it is assumed that the electron charge is $-e$ (e is positive) and that the positive bias voltage corresponds to current flowing from the left to right junctions, whereas electrons flow in the opposite direction.

1.2.2   Sequential Tunneling and Cotunneling

Out of the Coulomb blockade regime the electric current is dominated by first-order tunneling processes, when electrons tunnel by consecutive tunneling events. This transport regime is known as *sequential tunneling regime* [3, 4]. An example of first-order process is sketched in Fig. 1.1a. Although in the Coulomb blockade regime the sequential tunneling is exponentially suppressed, the current can still be mediated by higher-order tunneling processes involving correlated tunneling
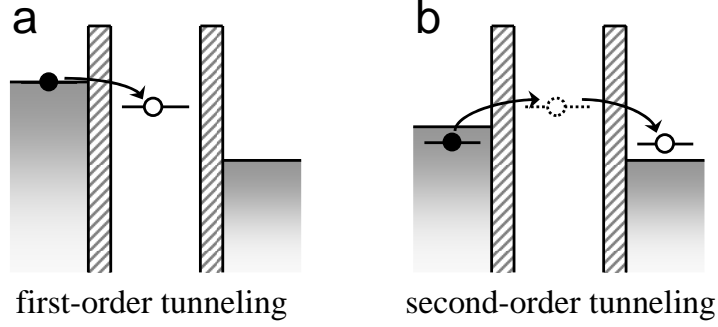
Figure 1.1: A sketch illustrating process of (a) sequential tunneling and (b) cotunneling.

of two or more electrons *via* intermediate virtual states [29, 30, 31]. The former processes are known as *cotunneling*. An exemplary cotunneling process is illustrated in Fig. 1.1b.

1.2.3 Tunnel Magnetoresistance

When the electrodes are made of ferromagnetic material, the system exhibits further interesting phenomena resulting from the interplay of charge and spin degrees of freedom [32, 33]. In particular, the tunneling current flowing through the system depends on the mutual alignment of magnetic moments of ferromagnetic electrodes, giving rise to the *spin-valve* effect or, more commonly, the *tunnel magnetoresistance* (TMR) effect [34, 35]. A simple theoretical model of TMR was introduced by M. Jullière [36] in 1975. Jullière considered a single ferromagnetic tunnel junction and assumed that the magnetic moments of the leads can form either parallel or antiparallel configurations, see Fig. 1.2a. In the parallel configuration the majority (minority) electrons of the left lead tunnel to the majority (minority) electron band in the right lead, as illustrated in Fig. 1.2b. Whereas, in the antiparallel configuration the majority (minority) electrons from the left lead tunnel to the minority (majority) electron band in the right lead. This situation is shown in Fig. 1.2c. Thus, one can express the electric current I flowing in the parallel (I_P) and antiparallel (I_AP) magnetic configurations as

$$I_\mathrm{P} \quad \sim \quad \rho_\mathrm{L+}\rho_\mathrm{R+} + \rho_\mathrm{L-}\rho_\mathrm{R-} \; , \tag{1.1}$$

$$I_\mathrm{AP} \quad \sim \quad \rho_\mathrm{L+}\rho_\mathrm{R-} + \rho_\mathrm{L-}\rho_\mathrm{R+} \; , \tag{1.2}$$

where $\rho_{r\sigma}$ is the density of states for the majority ($\sigma = +$) or minority ($\sigma = -$) electron band in the lead r. In the following it is assumed that the density of states is independent of energy within the electron band.
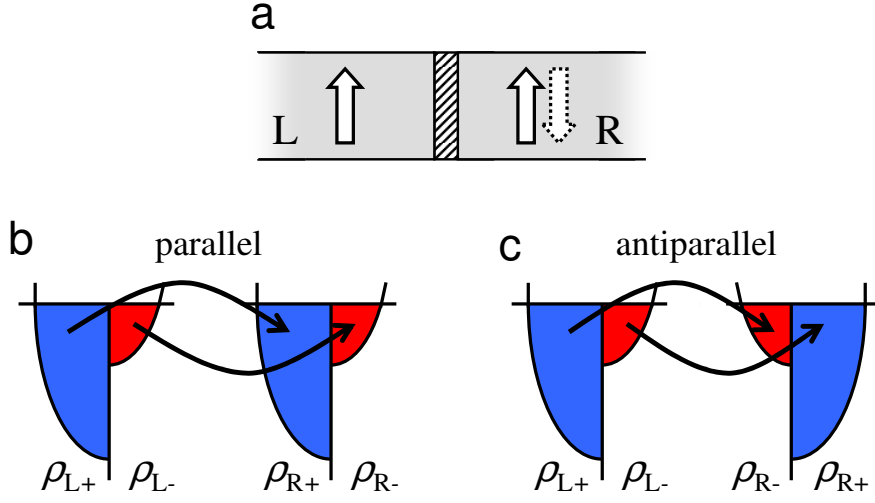
Figure 1.2: Single ferromagnetic tunnel junction (a) and sketch of densities of states for the majority ρ_{r+} (blue) and minority ρ_{r-} (red) electron band in the lead r ($r = $ L, R) for the parallel (b) and antiparallel (c) magnetic configurations.

The tunnel magnetoresistance is defined phenomenologically as

$$\text{TMR} = \frac{R_{\text{AP}} - R_{\text{P}}}{R_{\text{P}}} = \frac{I_{\text{P}} - I_{\text{AP}}}{I_{\text{AP}}} \; , \tag{1.3}$$

where R_{P} and R_{AP} are the total system resistances in the parallel and antiparallel configurations, respectively. Using Eqs. (1.1) and (1.2) and expressing the spin-dependent densities of states in terms of spin polarization of the lead r, p_r, defined as

$$p_r = \frac{\rho_{r+} - \rho_{r-}}{\rho_{r+} + \rho_{r-}} \; , \tag{1.4}$$

one can find for the TMR effect

$$\text{TMR} = \frac{2 p_{\text{L}} p_{\text{R}}}{1 - p_{\text{L}} p_{\text{R}}} \equiv \text{TMR}^{\text{Jull}} \; . \tag{1.5}$$

1.3   Outline

This dissertation is devoted to spin-polarized transport in nanostructures with Coulomb blockade. The sequel is divided into two parts. The first part addresses the problem of tunneling through ferromagnetic systems consisted of nanoscopic islands coupled to external reservoirs. In particular, chapter 2 presents a review of transport in ferromagnetic single-electron transistors, whereas chapter 3 deals with spin-dependent tunneling in double-island devices. In both cases numerical

results are presented and discussed in the absence and presence of nonequilibrium spin accumulation on the islands. It is shown that spin accumulation may give rise to negative differential conductance and modifies the TMR effect substantially.

The second part of the thesis concerns the spin-polarized transport through quantum dots coupled to ferromagnetic leads. Chapter 4 presents the numerical results and their discussion in the case when the magnetic moments of the leads are magnetized collinearly with respect to each other. The model considered is presented in section 4.1. Section 4.2 describes the real-time diagrammatic technique used in calculations, whereas section 4.3 covers the Averin-Nazarov approach. The numerical results on the first-order and second-order transport are presented in section 4.4. The behavior of tunnel magnetoresistance is analyzed in various transport regimes. It is shown that the magnitude of TMR strongly depends on the transport regime. In particular, a parity effect in TMR in the linear response is predicted. Moreover, it is shown that in the case of the Coulomb blockade regime with odd number of electrons the TMR effect has a minimum at zero bias. This minimum is a consequence of the zero-bias peak in differential conductance in the antiparallel magnetic configuration. The discussion and presentation of properties and mechanism of the zero-bias anomaly in differential conductance is given in section 4.5. The influence of magnetic field on the zero-bias peak is also discussed. In section 4.6 in turn we analyze the impact of intrinsic spin relaxation on the dot on second-order tunneling through quantum dots. It is shown that both the minimum in TMR at low bias voltage and the zero-bias anomaly in differential conductance disappear in the limit of fast spin relaxation.

Cotunneling transport in the Coulomb blockade regime in the case of quantum dots coupled to ferromagnetic leads with noncollinear alignment of the leads' magnetic moments is analyzed in chapter 5. The dependence of both the second-order current and TMR in the case of empty and singly-occupied quantum dot is analyzed as a function of the angle between the leads' magnetizations. It is shown that transport properties strongly depend on the relative alignment of magnetic moments of the leads.

Finally, the conclusions are given in chapter 6.

1.4   Acknowledgements

real-time diagrammatic technique.

I thank all colleagues from Mesoscopic Physics Division, especially, my thanks go to Wojciech Rudziński and Piotr Tomczak (Quantum Physics Division).

Finally, I want to thank my fiancée, family and all friends for their support during my studies.

Part I

Spin-Polarized Transport through Metallic Islands

In the first part of the present thesis transport through systems built of metallic islands is considered. First, the case of single-electron transistors is reviewed and, second, transport through double-island devices is discussed. These devices consist of central mesoscopic electrodes, the so-called *islands*, coupled through tunnel barriers to external reservoirs and to each other[1]. Furthermore, a gate voltage may be attached capacitively to each island. The capacitance C of a typical island is of the order of 10^{-18} F [39, 40, 41]. Consequently, its charging energy, $E_C = e^2/(2C)$, corresponding to the addition of a single electron on the island, may establish a new relevant energy scale. If the charging energy is larger than the thermal energy, $E_C \gg k_B T$, where T denotes temperature and k_B is the Boltzmann constant, the effects due to discreteness of charge become observable in the system transport characteristics, as discussed in section 1.2.1. First of all, the current is blocked below a certain threshold voltage, leading to the Coulomb blockade[2]. Furthermore, the single-electron charging leads to the step-like current-voltage dependence and oscillations of electric current when sweeping the gate voltage. The former effect is known in the literature as Coulomb staircase, whereas the latter one as Coulomb oscillations. These phenomena will be presented and discussed in the following sections.

The respective electrodes, of which the single-electron devices consist, can be built of either nonmagnetic or ferromagnetic materials[3]. Electronic transport in nonmagnetic tunnel junctions was already extensively studied in the past two decades [3, 4, 37, 38, 45, 46, 47, 48, 49, 50, 51]. However, it was only several years ago when the attention was drawn to electron tunneling in magnetic systems [32, 33, 34, 35, 52, 53, 54], which became possible owing to recent progress in nanotechnology. Magnetic multi-junctions seem to be of great importance for future electronics based on spin-dependent electronic transport (spintronics). Some of the effects that make those devices very promising have been known for a long time. In 1975 Jullière [36] discovered that the total resistance of a simple junction decreases when the magnetic configuration of the electrodes switches from antiparallel to parallel alignment, as described in section 1.2.3. Furthermore, it was shown theoretically that some qualitatively new effects may also arise from the interplay of charging effects and spin degrees of freedom such as, for example, oscillations of TMR with increasing bias voltage, spin accumulation, enhancement of TMR in the Coulomb blockade regime, etc. [32, 33, 55, 56, 57, 58, 59, 60, 61, 62]. The enhancement of TMR in the cotunnel-

---

[1]An important example and convenient model system is a single-electron transistor, which is built of one island coupled *via* tunnel barriers to external reservoirs [37, 38].

[2]The first-order tunneling processes are exponentially suppressed, however, the current can still be mediated by higher-order tunneling processes, see section 1.2.2.

[3]The ferromagnetic electrodes can be made either from ferromagnetic transition metals (like Ni, Co, Fe) or from other conducting ferromagnetic systems [34, 35, 42, 43]. For a review on first-order transport through both nonmagnetic and ferromagnetic single-electron transistors see Ref. [44].

ing regime and the oscillations of TMR as a function of the transport voltage were also observed experimentally [41, 42, 43, 63]. Another interesting feature of magnetic mesoscopic junctions is that they can be used as sources of spin-polarized current, in which the polarization degree can be controlled by an external gate voltage [64, 65, 66].

Chapter 2

Transport in Single-Electron Transistors

This chapter reviews the issues of spin-dependent transport in ferromagnetic single-electron transistors (FM SETs). A SET consists of one central nanoscopic island coupled through tunnel barriers to source and drain electrodes. The two following cases are considered, namely, the first one when all the electrodes are ferromagnetic and the second case when the source and drain electrodes are ferromagnetic, whereas the island is nonmagnetic. In the latter situation, a non-equilibrium spin accumulation induced on the island is crucial for the observation of a nonzero TMR effect.

2.1 Description of Model and Method

The schematics of single-electron transistors considered in this chapter are illustrated in Fig. 2.1. Part (a) presents a device whose all three electrodes are ferromagnetic (FM/FM/FM SET), whereas part (b) shows a system with ferromagnetic source and drain electrodes, while the island is nonmagnetic (FM/NM/FM SET). In general, the magnetic moments of the electrodes may be aligned in an arbitrary way with respect to each other. Here, however, only the collinear alignments of magnetic moments, namely, the parallel (P) and antiparallel (AP) magnetic configurations are considered. They are specified in Fig. 2.1. In the case of the first system, in both configurations the magnetic moments of external electrodes point in the same direction, while magnetic moment of the island is either parallel or antiparallel to them. Whereas in the case of the second system, in the parallel configuration the magnetic moments of external electrodes are aligned while in the antiparallel configuration they are anti-aligned. The two magnetic alignments can be easily achieved by sweeping magnetic field through the hysteresis loop, provided the respective ferromagnetic components have different coercive fields.

a

$C_\mathrm{L}, R_\mathrm{L}$ $-ne$ $C_\mathrm{R}, R_\mathrm{R}$

V_L —   — V_R

C_g

V_g

b

$C_\mathrm{L}, R_\mathrm{L}$ $-ne$ $C_\mathrm{R}, R_\mathrm{R}$

V_L —   — V_R

C_g

V_g
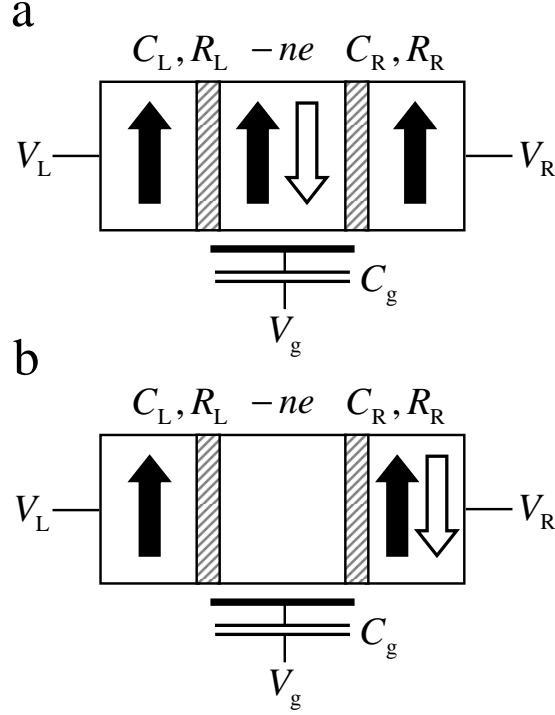
Figure 2.1: Schematics of ferromagnetic single-electron transistors. The parallel and antiparallel magnetic configurations of the system are also specified. The island is separated from external electrodes by tunnel barriers. Each barrier is characterized by its resistance R_r and capacitance C_r ($r = \mathrm{L}, \mathrm{R}$). The system is symmetrically biased, $V_\mathrm{L} = V/2$, $V_\mathrm{R} = -V/2$, and there is also a gate voltage V_g applied to the island.

The considerations are restricted to the sequential tunneling regime, which implies that the higher-order tunneling processes are not taken into account. This is justified when the resistances of both barriers are much larger than the quantum resistance, $R_r \gg R_Q = h/e^2$. As a consequence, the charge on the island is well localized and the *orthodox* tunneling theory is applicable [3, 4]. Further, only spin-conserving tunneling processes through the two barriers are considered. Moreover, the island is assumed to be relatively large, which implies that the effects due to quantization of the corresponding energy levels can be neglected. For smaller islands, however, the discrete energy spectrum may modify transport characteristics and has to be considered [67, 68, 69].

In order to calculate electric current, the method based on the master equation is employed. This method takes into account the fact that the net transition rate between the charge states with n and $n+1$ excess electrons on the island vanishes in a stationary state. Thus, the probability $P(n, V)$ to find the island in a state with n additional electrons when a bias voltage V is applied can be determined

11

from the following recursion relation [45, 46]

$$P(n+1,V) \sum_{\sigma} [y^{\sigma}(n+1,V)] = P(n,V) \sum_{\sigma} [x^{\sigma}(n,V)] , \qquad (2.1)$$

where $x^{\sigma}(n,V) = \sum_{r=\mathrm{L,R}} \Gamma_{r\mathrm{I}}^{\sigma}(n,V)$ and $y^{\sigma}(n,V) = \sum_{r=\mathrm{L,R}} \Gamma_{\mathrm{I}r}^{\sigma}(n,V)$, corresponding to transition rates for tunneling to and off the island, respectively. Here, $\Gamma_{r\mathrm{I}}^{\sigma}(n,V)$ is the spin-dependent rate for tunneling of electrons with spin σ from reservoir r to the island, whereas $\Gamma_{\mathrm{I}r}^{\sigma}(n,V)$ denotes the rate for tunneling backward. The rates can be expressed by means of the Fermi golden rule as

$$\Gamma_{r\mathrm{I}(\mathrm{I}r)}^{\sigma}(n,V) = \frac{1}{e^2 R_{r\sigma}} \frac{\Delta E_{r\mathrm{I}(\mathrm{I}r)}^{\sigma}(n,V)}{\exp\left[\Delta E_{r\mathrm{I}(\mathrm{I}r)}^{\sigma}(n,V)/k_{\mathrm{B}}T\right] - 1} , \qquad (2.2)$$

where $\Delta E_{r\mathrm{I}(\mathrm{I}r)}^{\sigma}(n,V)$ describes a change in the system electrostatic energy caused by corresponding tunneling event when in the initial state there were n additional electrons on the island. In the above equation $R_{r\sigma}$ denotes the spin-dependent tunnel resistance of the r-th junction and is given by

$$R_{r\sigma} = \frac{\hbar}{2\pi e^2 \rho_{r\sigma}\rho_{\mathrm{I}\sigma}|t_{r\sigma,\mathrm{I}\sigma}|^2} . \qquad (2.3)$$

The spin dependence of the resistance is a consequence of spin-dependent density of electron states at the Fermi level in the respective electrodes between which the junction is formed and the corresponding tunneling matrix elements. In particular, in the above case it is due to the spin-dependent density of states of the r-th lead $\rho_{r\sigma}$ and the island $\rho_{\mathrm{I}\sigma}$, as well as tunneling matrix elements $t_{r\sigma,\mathrm{I}\sigma}$.

In the following, the different magnetic configurations of devices are considered, therefore it is crucial to define the respective reference systems. Thus, it is assumed that the global quantization axis is aligned along the net spin of the left electrode (see Fig. 2.1), whereas local quantization axes are aligned along net spins of respective electrodes. Furthermore, the majority (minority) electrons in the local reference systems are labelled by $+$ ($-$), and the spin-up (spin-down) electrons in the global reference system are denoted by $\uparrow$ ($\downarrow$). In the parallel configuration all the magnetic moments point in the same direction, consequently the majority electrons are the spin-up ones and the minority electrons are the spin-down ones. In the case of the system shown in Fig. 2.1a, the antiparallel configuration is obtained by flipping the magnetic moment of the island. Now, the spin-up (spin-down) electrons correspond to the minority (majority) electron band in the island.

In these considerations it is further assumed that the energy relaxation time is much smaller than the time between two successive tunneling events, while no such restriction is imposed on the spin relaxation time which can be arbitrary. In a general case, due to the spin dependence of tunneling processes, a nonequilibrium

magnetic moment accumulates on the island, which leads to spin splitting of the corresponding Fermi level. Thus, the change in the system electrostatic energy, $\Delta E_{r\mathrm{I(I}r)}^{\sigma}(n,V)$, caused by tunneling of an electron with spin σ, is given by

$$\Delta E_{r\mathrm{I(I}r)}^{\sigma}(n,V) = \frac{e^2}{2C} \pm eU_r(n,V) \pm \Delta E_{\mathrm{F}}^{\sigma}\,, \qquad (2.4)$$

where $C = C_{\mathrm{L}} + C_{\mathrm{R}} + C_{\mathrm{g}}$, with C_{L} and C_{R} being the capacitances of the two junctions, and C_{g} denoting the gate capacitance. $U_r(n,V)$ is a voltage drop between the r-th electrode and the island

$$U_r(n,V) = C^{-1}\left[ne - Q_0 + (C_{r'} + C_{\mathrm{g}})\,V_r - C_{r'}V_{r'} - C_{\mathrm{g}}V_{\mathrm{g}}\right]\,, \qquad (2.5)$$

where V_r is the electrostatic potential of the r-th electrode and $r' \neq r$ ($r' = \mathrm{L}, \mathrm{R}$), whereas Q_0 represents the offset charge [4, 45, 60]. Finally, $\Delta E_{\mathrm{F}}^{\sigma}$ is the spin dependent shift of the Fermi energy on the island due to spin accumulation. The ratio of the Fermi level shifts for spin-up and spin-down electrons depends on the corresponding ratio of the densities of states.

When a transport voltage V is applied to the left and right electrodes, electrons can tunnel one by one through the barriers giving rise to a flowing current. The electric current flowing through the left junction can be then calculated from the following formula

$$I_{\mathrm{L}} = -e \sum_{\sigma} \sum_{n=-\infty}^{\infty} \left[\Gamma_{\mathrm{LI}}^{\sigma}(n,V) - \Gamma_{\mathrm{IL}}^{\sigma}(n,V)\right] P(n,V)\,. \qquad (2.6)$$

In the stationary state the currents flowing through each junction are equal, $I_{\mathrm{L}} = I_{\mathrm{R}} = I$.

2.2   Numerical Results

In the following section we present the numerical results on spin accumulation, electric current, its spin polarization, and resulting tunnel magnetoresistance. The two limiting cases are considered – the limit of fast spin relaxation and the limit of slow spin relaxation on the island. In the former case the spin of an electron tunneling to the island relaxes before a next tunneling event takes place. In the latter case, on the other hand, the electron spin is conserved for a time much longer than the time between successive tunneling events.

2.2.1   Limit of Fast Spin Relaxation for FM SET with Ferromagnetic Island

In the limit of fast spin relaxation, SETs with nonmagnetic islands behave like nonmagnetic junctions, exhibiting no TMR effect. Therefore, in this limit only
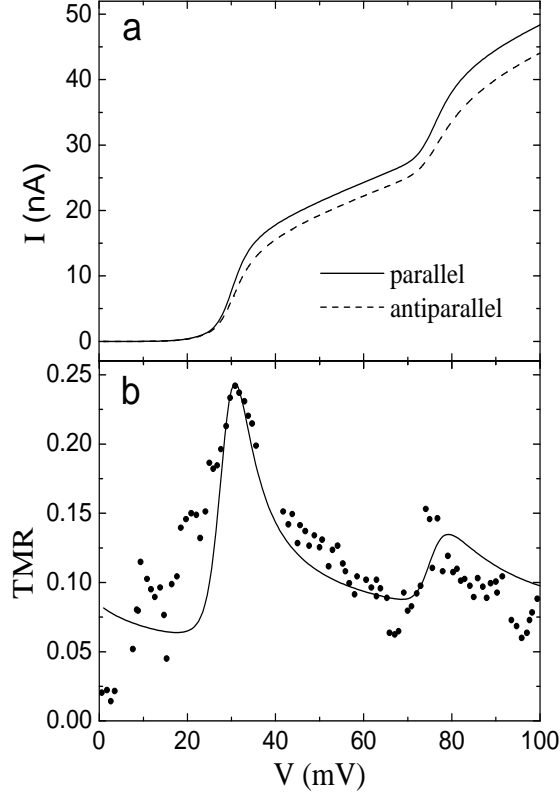
Figure 2.2: The current in the parallel and antiparallel magnetic configurations (a) and the resulting TMR (b) as a function of the bias voltage for FM/FM/FM SET. The parameters are: $T = 9$ K, $R_{L\uparrow}^P = 0.65$ MΩ, $R_{L\downarrow}^P = 0.065$ MΩ, $R_{R\uparrow}^P = 5$ MΩ, $R_{R\downarrow}^P = 2.5$ MΩ, $R_{r\downarrow}^{AP} = R_{r\uparrow}^{AP} = (R_{r\uparrow}^P R_{r\downarrow}^P)^{1/2}$ (for $r = $ L, R), the capacitances: $C_L = 0.1$ aF, $C_R = 1$ aF, $C_g = 5.1$ aF, $V_g = 0$, and $Q_0 = 0.025e$. The dots in part (b) present the experimental data taken from Ref. [41].

the calculations for FM SETs with ferromagnetic islands are presented. It is assumed that the spin-dependent resistances for the parallel ($R_{r\sigma}^P$) and antiparallel ($R_{r\sigma}^{AP}$) configurations fulfill the condition $R_{r\sigma}^P R_{r\bar{\sigma}}^P = R_{r\sigma}^{AP} R_{r\bar{\sigma}}^{AP}$. Since there is no spin accumulation on the island in the limit of fast spin relaxation, there is no associated spin splitting of the Fermi level either, $\Delta E_F^\sigma = 0$.

The current flowing through the system in the parallel and antiparallel configurations and the resulting TMR are displayed in Fig. 2.2. For both magnetic configurations the $I - V$ curves reveal the well-known Coulomb steps. Moreover, these two curves are different; current flowing in the parallel configuration is generally larger than current flowing in the antiparallel configuration, see Fig. 2.2a. This difference leads in turn to nonzero TMR effect, as shown in Fig. 2.2b. It can also be seen that TMR oscillates as a function of the bias voltage. Furthermore, the amplitude of these oscillations decreases as the transport voltage increases.
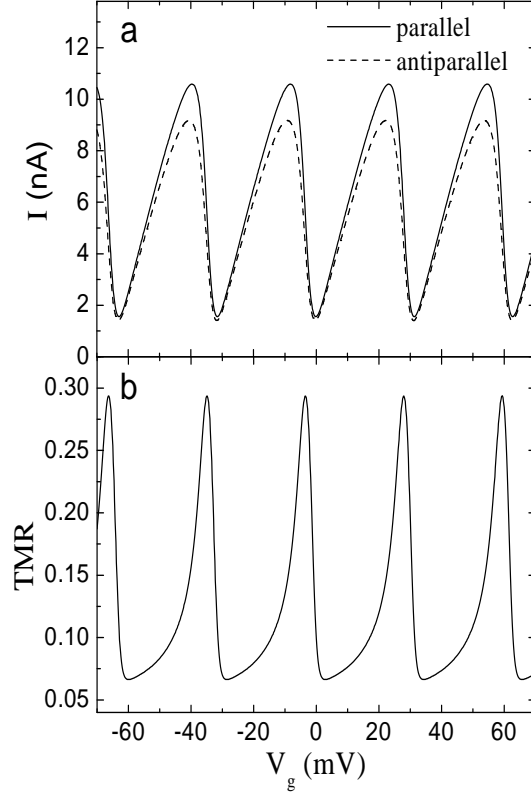
Figure 2.3: The current in the parallel and antiparallel magnetic configurations (a) and the resulting TMR (b) as a function of the gate voltage calculated for $V = 25$ mV. The other parameters are the same as in Fig. 2.2.

For parameters assumed here, TMR reaches local maxima at the voltages corresponding to the positions of the Coulomb steps. The global maximum value, however, appears at the first step, i.e., at the threshold voltage. It is also worth noting that the enhancement of TMR at the Coulomb steps remarkably decreases when the temperature is increased and, at $k_{\mathrm{B}}T \approx E_{\mathrm{C}}$, the effects due to discrete charging disappear [60].

Recently, the oscillatory behavior of the TMR effect with increasing transport voltage was observed experimentally by Ernult *et al.* [41]. The experimental data taken from Ref. [41] are displayed in Fig. 2.2b and marked by dots.

The above characteristics were calculated in the case of vanishing gate voltage. From the application point of view, however, the gate voltage characteristics seem to be more important. In Fig. 2.3a we present the Coulomb oscillations of electric current as a function of gate voltage, calculated for the parallel and antiparallel configurations. The curves are calculated for the bias voltage equal to 25 mV, which corresponds to the first Coulomb step, see Fig. 2.2a. Once the Fermi level of the island lies in the energy window due to applied bias voltage, the

current is increased, otherwise, it is suppressed. This results in the oscillatory dependence of electric current on the gate voltage, as shown in Fig. 2.3a. The periodic variation of the current with the gate voltage leads in turn to periodic behavior of the TMR. This is presented in Fig. 2.3b.

2.2.2 Limit of Slow Spin Relaxation for FM SET with Nonmagnetic Island

In the case of FM SETs with nonmagnetic islands, nonzero TMR can exist only when the spin relaxation time is sufficiently long, significantly longer than the time between successive tunneling events[1]. If this is the case, a nonequilibrium magnetic moment builds up on the island due to spin accumulation. This moment is responsible for the occurrence of TMR. In other words, the island becomes magnetized in a nonequilibrium situation, and the created moment depends on the bias and gate voltages. It is worth noting that spin accumulation may occur not only due to spin-dependent sequential tunneling, but also due to spin-dependent cotunneling processes [59, 72].

For arbitrary spin relaxation times the splitting of the Fermi level can be determined from the current conservation condition for each spin orientation separately [58, 73]

$$\frac{1}{e}(I_{\mathrm{R}}^{\sigma} - I_{\mathrm{L}}^{\sigma}) - \frac{\rho_{\mathrm{I}}\Omega_{\mathrm{I}}}{\tau_{\mathrm{sf}}}\Delta E_{\mathrm{F}}^{\sigma} = 0 \,, \tag{2.7}$$

where ρ_{I} is the density of states of the nonmagnetic island, Ω_{I} is the island's volume, and τ_{sf} denotes the spin relaxation time on the island. I_{L}^{σ} and I_{R}^{σ} are the currents flowing through the left and right junctions in the spin channel σ. The last term in Eq. (2.7) takes into account intrinsic spin-flip processes on the island. In the limit of slow spin relaxation, $\tau_{\mathrm{sf}} \to \infty$, Eq. (2.7) reduces to $I_{\mathrm{L}}^{\sigma} = I_{\mathrm{R}}^{\sigma}$. From this condition it is possible to calculate self-consistently the shifts of the Fermi levels for both spin orientations. Since the density of states at the Fermi level in a nonmagnetic island is independent of the spin orientation, it is justifiable to assume $\Delta E_{\mathrm{F}}^{\sigma} = -\Delta E_{\mathrm{F}}^{\bar{\sigma}}$. Apart from this, in the case of FM SETs with nonmagnetic islands the resistances in the antiparallel configuration are $R_{\mathrm{L}\sigma}^{\mathrm{AP}} = R_{\mathrm{L}\sigma}^{\mathrm{P}}$ and $R_{\mathrm{R}\sigma}^{\mathrm{AP}} = R_{\mathrm{R}\bar{\sigma}}^{\mathrm{P}}$, see Fig. 2.1b.

Figure 2.4 presents the basic transport characteristics of FM SET with nonmagnetic island as a function of the bias voltage calculated in the limit of slow spin relaxation. The splitting of the Fermi level is displayed in Fig. 2.4a for both magnetic configurations. It is clear that the splitting takes place only in the antiparallel alignment, while in the parallel configuration there is no spin accumulation. However, this is true only in the case when both junctions are characterized by equal spin asymmetry factors. When the spin asymmetries are different, spin

---

[1]The longest spin relaxation times were measured for aluminium and copper [70, 71]. For example, the relaxation time for copper was estimated to be of the order of 10^{-7} s.
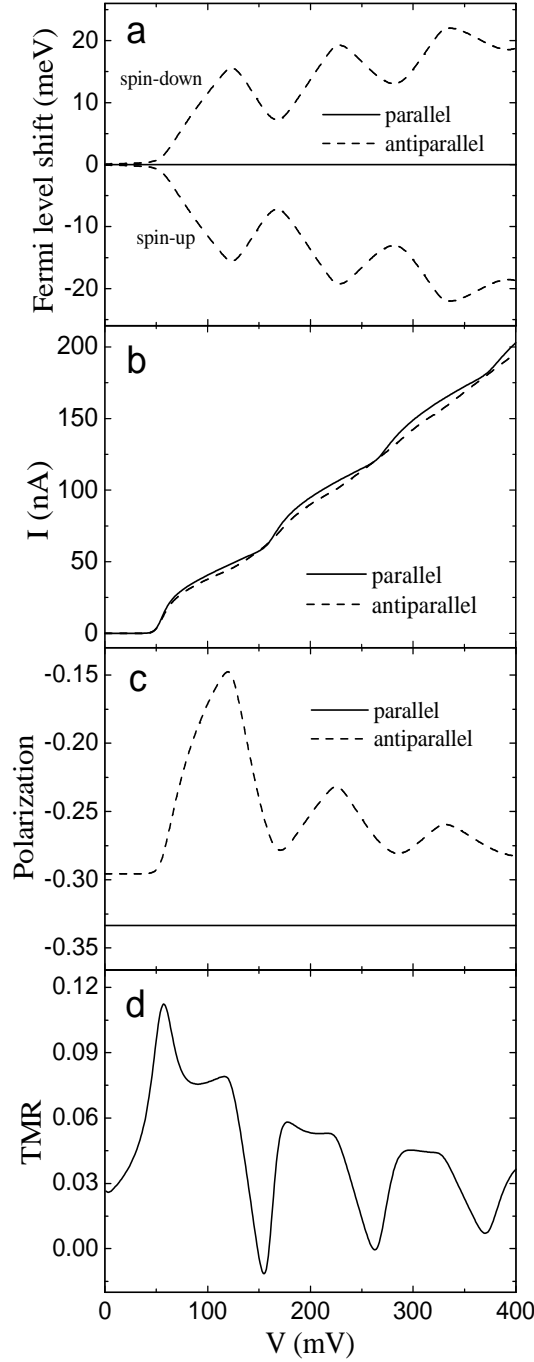
Figure 2.4: Basic characteristics of FM/NM/FM SET as a function of the bias voltage in the limit of slow spin relaxation on the island: (a) spin splitting of the Fermi level, (b) $I - V$ characteristics, (c) spin polarization of electric current, and (d) tunnel magnetoresistance. The parameters are: $k_{\mathrm{B}}T = 0.05\,E_{\mathrm{C}}$, $R_{\mathrm{L}\uparrow}^{\mathrm{P}} = 5$ MΩ, $R_{\mathrm{L}\downarrow}^{\mathrm{P}} = 2.5$ MΩ, $R_{\mathrm{R}\uparrow}^{\mathrm{P}} = 0.3$ MΩ, $R_{\mathrm{R}\downarrow}^{\mathrm{P}} = 0.15$ MΩ, the capacitances: $C_{\mathrm{L}} = C_{\mathrm{R}} = C_{\mathrm{g}} = 1$ aF, $V_{\mathrm{g}} = 0$, and $Q_0 = 0$.

accumulation also occurs in the parallel configuration. As illustrated in Fig. 2.4a, the behavior of the Fermi level splitting with increasing transport voltage can be decomposed into two components. One component monotonically increases, while the second one oscillates with increasing the bias voltage. This oscillatory behavior can be understood in the following way. Let us assume that the voltage is slightly above that corresponding to a certain Coulomb step and begins to increase. Then, the spin accumulation also increases, until a local maximum value is reached. The local maximum occurs at a voltage, at which the chemical potential of the depleted spin channel approaches the value which allows the next charge state on the island. This, in turn, enhances tunneling rate (onto the island) of electrons corresponding to the depleted spin channel, and consequently reduces the spin splitting of the Fermi level. When the voltage increases further, a local minimum in the spin accumulation is then reached at a voltage, where the chemical potential of the second (accumulated) spin channel approaches the value which allows the next charge state on the island. The same scenario repeats at each Coulomb step leading to the oscillatory behavior of the spin accumulation. Because only the first-order tunneling processes are considered, there is no spin accumulation in the Coulomb blockade regime, as can be seen in Fig. 2.4a. In real situations, however, the higher-order tunneling processes, which dominate transport when sequential tunneling is exponentially suppressed, may lead to finite spin accumulation in the Coulomb blockade [59, 65].

The current as a function of the bias voltage for the parallel and antiparallel configurations is shown in Fig. 2.4b. As before, there are characteristic Coulomb steps, although now they are more complex. In both configurations the electric current is spin polarized. Generally, the polarization degree of the current flowing through the r-th junction can be defined as

$$\eta_r = \frac{I_r^\uparrow - I_r^\downarrow}{I_r^\uparrow + I_r^\downarrow}, \tag{2.8}$$

where $I_r^\uparrow$ and $I_r^\downarrow$ are the currents flowing in the spin-up and spin-down channels. In the slow spin relaxation limit, the polarization of electric current is constant, i.e., the same for both junctions. The spin polarization calculated for both magnetic configurations is shown in Fig. 2.4c. The polarization degree is constant in the parallel configuration (where there is no spin accumulation) and becomes voltage dependent for the antiparallel alignment. Moreover, in the antiparallel configuration it oscillates with increasing bias voltage and the amplitude of these oscillations decreases as the bias is increased. The TMR effect corresponding to the $I - V$ curves shown in Fig. 2.4b is presented in Fig. 2.4d. Now, the bias dependence is more complex than it was in the case of FM SETs with magnetic islands. This difference is a result of the bias dependence of spin accumulation.

The same transport characteristics as in Fig. 2.4, but calculated as a function of the gate voltage, are shown in Fig. 2.5. As previously, there is no spin splitting
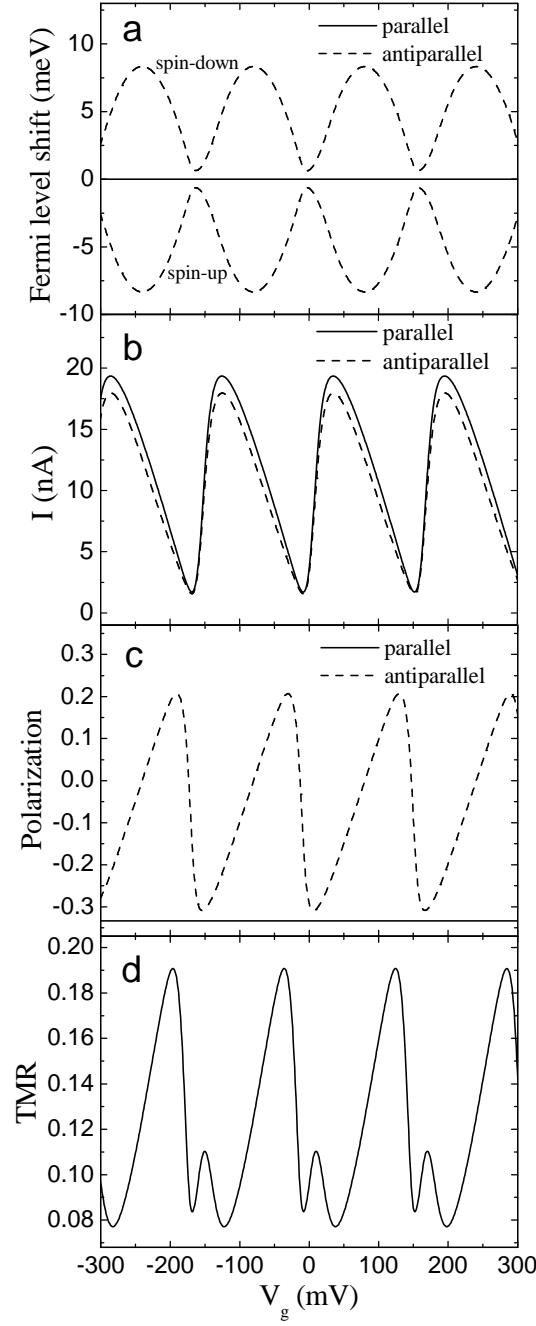
Figure 2.5: Characteristics the same as in Fig. 2.4, but shown as a function of the gate voltage for the bias voltage of 50 mV. The other parameters are the same as in Fig. 2.4.

of the Fermi level in the parallel configuration, while the splitting in the antiparallel configuration varies periodically with the gate voltage, as shown in Fig. 2.5a.
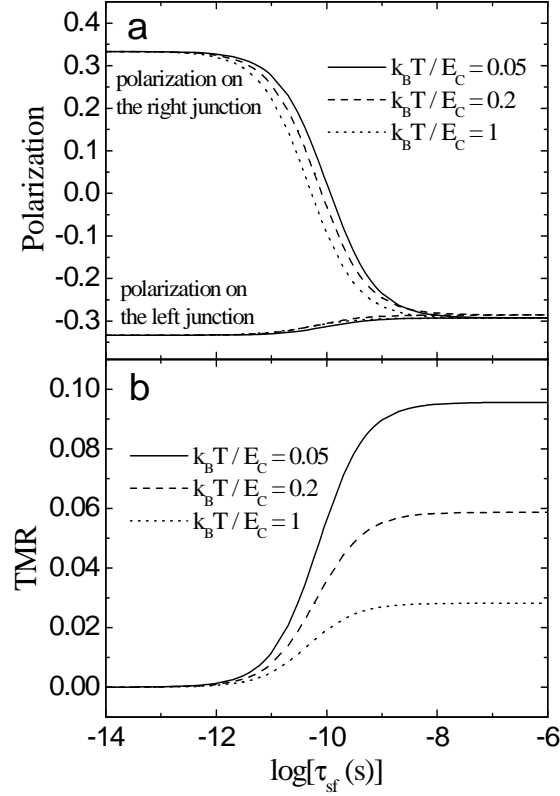
Figure 2.6: Spin polarization of the current flowing through both junctions (a) and TMR (b) as a function of the spin relaxation time calculated for indicated temperatures and for $V = 50$ mV, $\rho_I \Omega_I = 1000$/eV. The other parameters are the same as in Fig. 2.4.

The current flowing through the system in the parallel and antiparallel configurations (Fig. 2.5b) changes periodically with the gate voltage, leading to the Coulomb oscillations. The corresponding TMR, shown in Fig. 2.5d, also varies periodically with the gate voltage. It is interesting to note that some additional peaks appear in TMR, which were absent in the case shown in Fig. 2.3b. Furthermore, it can be seen that the spin polarization of the current in the antiparallel configuration oscillates as a function of the gate voltage changing its sign, as illustrated in Fig. 2.5c. Thus, by applying a gate voltage, one may control the nonequilibrium magnetic polarization of the island and also the spin polarization of the flowing current [65].

2.2.3   General Case

In the preceding subsection the typical transport characteristics of FM SETs with nonmagnetic islands in the limit of slow spin relaxation were presented. It

is, however, also interesting to analyze the crossover from the slow to fast spin relaxation limits. In the case of SETs with nonmagnetic islands TMR vanishes in the fast spin relaxation limit. The transport characteristics for arbitrary relaxation time can be calculated from Eq. (2.7). They are presented in Fig. 2.6. The spin polarization of the current flowing through the left and right junctions plotted as a function of the spin relaxation time is shown in Fig. 2.6a. The results are calculated for three different temperatures and for the antiparallel configuration. One can note that in the slow spin relaxation limit, the spin polarization is the same for both junctions. However, once the spin relaxation time becomes shorter, the spin polarizations become different and in the fast spin relaxation limit they are opposite. The behavior of TMR at the crossover from fast to slow spin relaxation limits is displayed in Fig. 2.6b. As the relaxation time becomes shorter tunnel magnetoresistance decreases and finally vanishes in the fast spin relaxation limit. It can also be seen that the TMR decreases with increasing temperature, the crossover between the limits of $\tau_{\mathrm{sf}} = 0$ and $\tau_{\mathrm{sf}} = \infty$, on the other hand, only slightly depends on temperature. In the case of spin polarization of electric current shown in Fig. 2.6a, both the spin polarization and the crossover are almost independent of temperature. The crossover from fast to slow spin relaxation limits takes place for spin relaxation time comparable to the time between two successive tunneling events, which can be estimated to be of the order of 10^{-10} s.

Chapter 3

Transport in Double-Island Devices

In the previous chapter the basic characteristics of ferromagnetic single-electron transistors were analyzed. In the following, we present and discuss the results on spin-polarized electronic transport through a double-island structure which is coupled through tunnel barriers to external electrodes. Furthermore, we also take into account nonequilibrium spin accumulation on the islands, calculated in a self-consistent way, which gives rise to new and nontrivial behavior of electric current and the TMR effect [74]. Although the research on transport in ferromagnetic double-island devices is in its early stage, in was already shown that such devices could serve as, for example, magnetoresistive elements in spintronics with gate-controlled magnitude of tunnel magnetoresistance [75] or as spin pumps [76].

3.1 Description of Model

A schematic of a double-island device is displayed in Fig. 3.1. The device consists of two nanoscopic islands separated from each other and coupled to external reservoirs by tunnel barriers. There are also gate voltages attached capacitively to the islands. Generally, both the islands and external electrodes can be built of either nonmagnetic or ferromagnetic materials [34, 43, 76]. In the following, it is assumed that at least two electrodes are ferromagnetic. Furthermore, their magnetic moments can form only collinear configurations. Consequently, two different magnetic configurations can be defined: the parallel and antiparallel ones. The system is described by its electrostatic energy which can be expressed as [75, 77]

$$
\begin{aligned}
E(n_1, n_2) &= E_{C_1}\left(n_1 - \frac{Q_{g1}}{e}\right)^2 + E_{C_2}\left(n_2 - \frac{Q_{g2}}{e}\right)^2 \\
&\quad + 2E_{C_M}\left(n_1 - \frac{Q_{g1}}{e}\right)\left(n_2 - \frac{Q_{g2}}{e}\right),
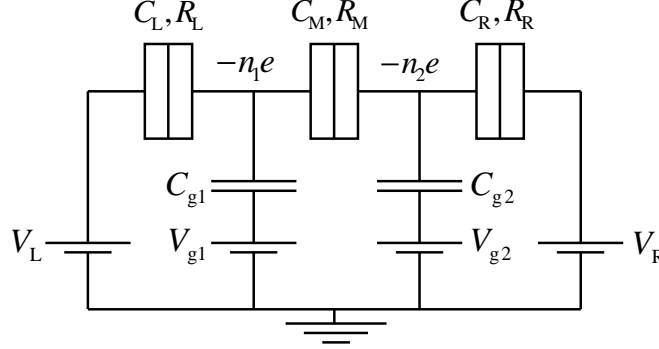\end{aligned}
\tag{3.1}
$$

Figure 3.1: Schematic of a double-island device. The first (1) and second (2) islands are capacitively coupled to two gate voltages, V_{g1} and V_{g2}, and separated from each other and from the left and right electrodes by tunnel barriers. The system is symmetrically biased, $V_L = V/2$ and $V_R = -V/2$.

where $n_{1(2)}$ is the number of excess electrons on the first (second) island and $Q_{g1(g2)}$ describes the respective charge induced by applied voltages, $Q_{g1(g2)} = C_{L(R)}V_{L(R)} + C_{g1(g2)}V_{g1(g2)}$. E_{C_1} and E_{C_2} denote the charging energies of the corresponding islands, whereas E_{C_M} describes the electrostatic energy of coupling between the islands

$$E_{C_1(C_2)} = \frac{e^2}{2C_{1(2)}}\left(1 - \frac{C_M^2}{C_1 C_2}\right)^{-1}, \tag{3.2}$$

$$E_{C_M} = \frac{e^2}{2C_M}\left(\frac{C_1 C_2}{C_M^2} - 1\right)^{-1}, \tag{3.3}$$

with $C_{1(2)}$ being the total capacitance of the first (second) island, $C_{1(2)} = C_{L(R)} + C_{g1(g2)} + C_M$, and C_M denoting the capacitance of the middle junction. The electrostatic energy, Eq. (3.1), is given with accuracy to terms irrelevant of n_1 and n_2. This, however, does not affect the final result because one is mainly interested in energy change between different charge states. Thus, the terms independent of electron numbers cancel. In real systems there may be a finite cross coupling between the first (second) gate voltage and the second (first) island [78]. In the following, however, it is assumed that the capacitance corresponding to this coupling is negligible.

In our considerations only the first-order tunneling processes are taken into account. The calculations are based on the master equation method and tunneling rates are given by the Fermi golden rule. The details and assumptions of the formalism were presented in the previous chapter. The main difference is that in the case of double-island devices the charge state of the system is defined by two numbers, (n_1, n_2), instead of one, as was in the case of single-electron transistors. This however complicates only the numerical part of the analysis.

23

In order to calculate the stationary current through the system it is necessary to determine the probabilities $P(n_1, n_2, V)$ of finding the system in the charge state with n_1 and n_2 additional electrons on the first and second islands, respectively, when a bias voltage V is applied. The corresponding probabilities can be calculated in a recursive way from the following steady-state master equation

$$
\begin{aligned}
0 \;=\; & -\sum_\sigma \Big[\Gamma_{\mathrm{L1}}^\sigma(n_1, n_2, V) + \Gamma_{\mathrm{1L}}^\sigma(n_1, n_2, V) + \Gamma_{12}^\sigma(n_1, n_2, V) \\
& +\Gamma_{21}^\sigma(n_1, n_2, V) + \Gamma_{\mathrm{2R}}^\sigma(n_1, n_2, V) + \Gamma_{\mathrm{R2}}^\sigma(n_1, n_2, V) \Big] P(n_1, n_2, V) \\
& +\sum_\sigma \Gamma_{\mathrm{L1}}^\sigma(n_1 - 1, n_2, V) P(n_1 - 1, n_2, V) \\
& +\sum_\sigma \Gamma_{\mathrm{1L}}^\sigma(n_1 + 1, n_2, V) P(n_1 + 1, n_2, V) \\
& +\sum_\sigma \Gamma_{12}^\sigma(n_1 + 1, n_2 - 1, V) P(n_1 + 1, n_2 - 1, V) \\
& +\sum_\sigma \Gamma_{21}^\sigma(n_1 - 1, n_2 + 1, V) P(n_1 - 1, n_2 + 1, V) \\
& +\sum_\sigma \Gamma_{\mathrm{R2}}^\sigma(n_1, n_2 - 1, V) P(n_1, n_2 - 1, V) \\
& +\sum_\sigma \Gamma_{\mathrm{2R}}^\sigma(n_1, n_2 + 1, V) P(n_1, n_2 + 1, V) \,, \qquad (3.4)
\end{aligned}
$$

and are fully determined using the normalization, $\sum_{n_1, n_2} P(n_1, n_2, V) = 1$. The corresponding transition rates are given by Eq. (2.2), while the respective changes in the total system electrostatic energy read

$$
\begin{aligned}
\Delta E_{\mathrm{L1}}^\sigma(n_1, n_2) &= E(n_1 + 1, n_2) - E(n_1, n_2) + eV_{\mathrm{L}} + \Delta E_{\mathrm{F1}}^\sigma \,, & (3.5) \\
\Delta E_{12}^\sigma(n_1, n_2) &= E(n_1 - 1, n_2 + 1) - E(n_1, n_2) - \Delta E_{\mathrm{F1}}^\sigma + \Delta E_{\mathrm{F2}}^\sigma \,, & (3.6) \\
\Delta E_{\mathrm{2R}}^\sigma(n_1, n_2) &= E(n_1, n_2 - 1) - E(n_1, n_2) - eV_{\mathrm{R}} - \Delta E_{\mathrm{F2}}^\sigma \,, & (3.7)
\end{aligned}
$$

if an electron with spin σ tunnels from the left lead to the first island, from the first island to the second one, and from the second island to the right lead, respectively, whereas for tunneling backward they are given by

$$
\begin{aligned}
\Delta E_{\mathrm{1L}}^\sigma(n_1, n_2) &= E(n_1 - 1, n_2) - E(n_1, n_2) - eV_{\mathrm{L}} - \Delta E_{\mathrm{F1}}^\sigma \,, & (3.8) \\
\Delta E_{21}^\sigma(n_1, n_2) &= E(n_1 + 1, n_2 - 1) - E(n_1, n_2) + \Delta E_{\mathrm{F1}}^\sigma - \Delta E_{\mathrm{F2}}^\sigma \,, & (3.9) \\
\Delta E_{\mathrm{R2}}^\sigma(n_1, n_2) &= E(n_1, n_2 + 1) - E(n_1, n_2) + eV_{\mathrm{R}} + \Delta E_{\mathrm{F2}}^\sigma \,. & (3.10)
\end{aligned}
$$

Here, $\Delta E_{\mathrm{F1}}^\sigma$ and $\Delta E_{\mathrm{F2}}^\sigma$ denote the corresponding shifts of the chemical potentials for spin σ electrons in the first and second islands. In order to describe the spin asymmetry of barriers, an asymmetry factor of barrier r, α_r, defined as $\alpha_r = R_{r\uparrow}/R_{r\downarrow}$, is introduced. The asymmetry factor corresponds to the ratio of the

respective spin-dependent densities of states. In particular, for FM/NM junctions it is given by $\alpha = \rho_\downarrow/\rho_\uparrow$, whereas for FM/FM junctions $\alpha = \rho_\downarrow^2/\rho_\uparrow^2$, provided that the two ferromagnetic electrodes are built of the same materials. The total resistance of barrier r is denoted by R_r and equal to $1/R_r = 1/R_{r\uparrow} + 1/R_{r\downarrow}$. When a bias voltage is applied to the system, a nonequilibrium spin accumulation may appear on the islands. Generally, the shift of the Fermi level for each spin direction may be different. In the following discussion, it is assumed that the ratio of the Fermi level shifts for the spin-up and spin-down electrons, defined as $\beta_j = -\Delta E_{\mathrm{F}j}^\uparrow/\Delta E_{\mathrm{F}j}^\downarrow$, fulfills the relation $\beta_j = \rho_{\mathrm{I}j\uparrow}/\rho_{\mathrm{I}j\downarrow}$, for the first ($j = 1$) and second ($j = 2$) islands, respectively, with $\rho_{\mathrm{I}j\sigma}$ being the spin-dependent density of states of the j-th island. As a consequence, for nonmagnetic islands one directly gets, $\beta_1 = \beta_2 = 1$.

Having found the probabilities $P(n_1, n_2, V)$, one can calculate electric current from the following formula

$$
I_{\mathrm{L}} = -e \sum_\sigma \sum_{n_1,n_2=-\infty}^{\infty} \left[\Gamma_{\mathrm{L}1}^\sigma(n_1, n_2, V) - \Gamma_{\mathrm{1L}}^\sigma(n_1, n_2, V) \right] P(n_1, n_2, V) \,. \quad (3.11)
$$

The above equation corresponds to the current flowing through the left junction, which in the stationary state is equal to currents flowing through the middle (I_{M}) and right junctions (I_{R}).

3.2 Numerical Results in the Absence of Spin Accumulation

Transport characteristics of a system built of two ferromagnetic islands and non-magnetic external electrodes are shown in Fig. 3.2. Different magnetic configurations of the system are specified in the inset of Fig. 3.2c. It is assumed that the relaxation time in the islands is much shorter than the time between two successive tunneling events. As a consequence, there is no spin accumulation on the islands. Because there is an asymmetry between junction resistances, the charge accumulates on the islands, as displayed in Fig. 3.2a. First of all, it can be seen that with increasing bias voltage, the amount of excess charge on the islands also increases. Because of the barrier asymmetry, it is easier for electrons to tunnel on the second island from the right lead than out of the second island to the first one. As a consequence, the electrons accumulate on the second island. On the other hand, it is easier for electrons to tunnel out of the first island to the left lead than from the second island to the first island. Thus, the number of excess electrons on the first island decreases with increasing the bias voltage – there are holes accumulated on the first island. This is the case in both magnetic configurations. The electric current flowing through the system in the parallel and
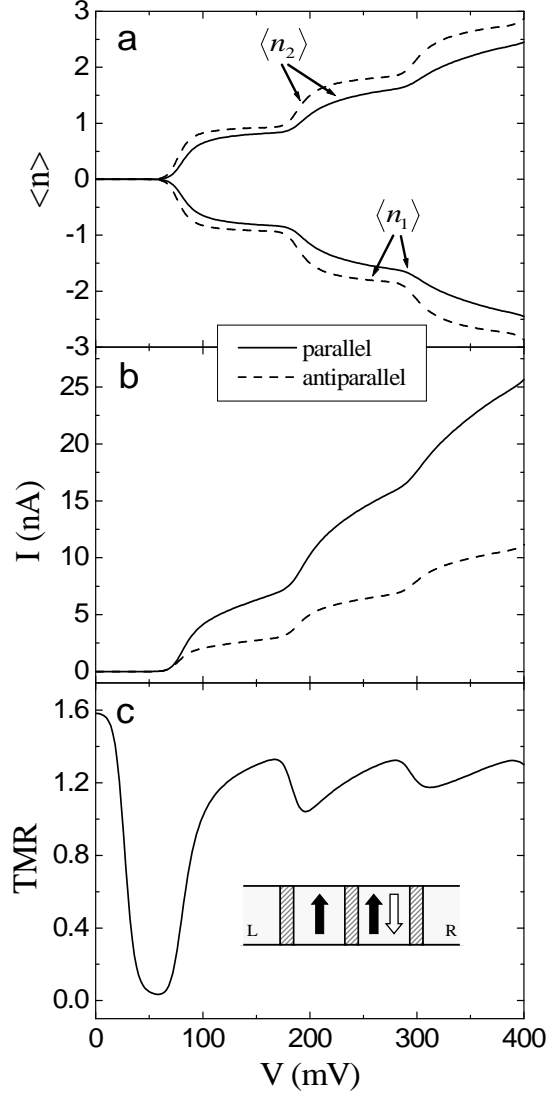
Figure 3.2:   The average electron number on the islands (a), currents (b) in the parallel and antiparallel configurations and the resulting TMR (c) as a function of the bias voltage. The parameters are: $C_1 = C_2 \equiv C = 3C_M = 3$ aF, $k_B T/(e^2/2C) = 0.05$. The spin asymmetries of resistances in the parallel configuration are $\alpha_L = \alpha_R = 5$, $\alpha_M = 25$, whereas the total junction resistances are $R_L^P = R_R^P = R_M^P/10 = 1$ MΩ. In the antiparallel configuration, $R_{L\sigma}^{AP} = R_{L\sigma}^P$, $R_{M\uparrow}^{AP} = R_{M\downarrow}^{AP} = (R_{M\uparrow}^P R_{M\downarrow}^P)^{1/2}$, and $R_{R\sigma}^{AP} = R_{R\bar{\sigma}}^P$.

antiparallel configurations is shown in Fig. 3.2b. The Coulomb steps due to discrete charging are clearly evident. Furthermore, the current flowing through the system in the parallel configuration is generally larger than the current flowing in the antiparallel configuration. This difference in turn gives rise to nonzero tunnel
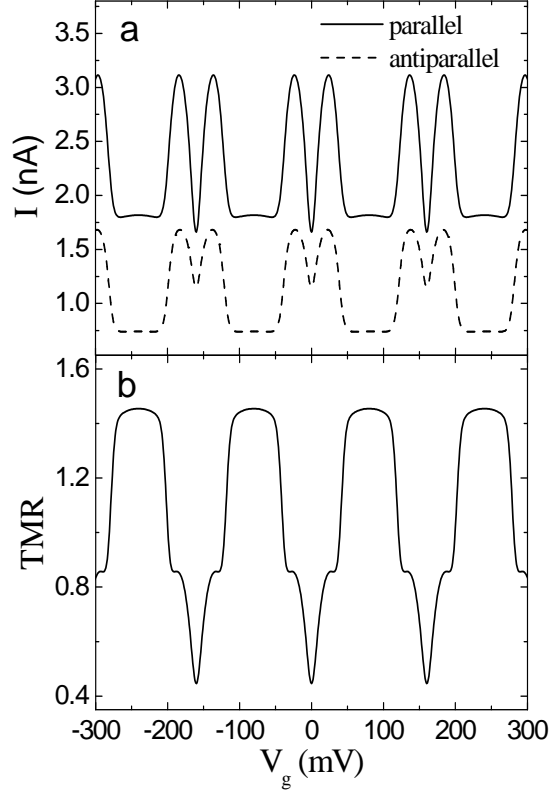
Figure 3.3: The current in the parallel and antiparallel configurations and resulting TMR as a function of gate voltages ($V_{g1} = V_{g2} = V_g$) for $V = 80$ mV. The other parameters are the same as in Fig. 3.2.

magnetoresistance, which is shown in Fig. 3.2c. The TMR effect oscillates as a function of the bias voltage and the amplitude of these oscillations decreases as the voltage is increased in a similar way as in the case of FM SETs, see Fig. 2.2b. Moreover, some dips occur in TMR at voltages corresponding to the steps in the current-voltage characteristics.

The current calculated for both magnetic configurations and the resulting TMR as a function of the gate voltage are displayed in Fig. 3.3. Figure was generated for $V = 80$ mV and the same voltage was applied to each gate $V_{g1} = V_{g2} = V_g$. The chosen value of the bias voltage corresponds to that slightly above the threshold voltage, see Fig. 3.2b. The Coulomb oscillations of electric current are presented in Fig. 3.3a. It is interesting to note that this dependence is different from that shown in Fig. 2.3a for single-electron transistor. Now there are two peaks for each period of Coulomb oscillations [77, 79]. The oscillations of current lead in turn to the oscillatory behavior of TMR as a function of gate voltage, as illustrated in Fig. 3.3b.

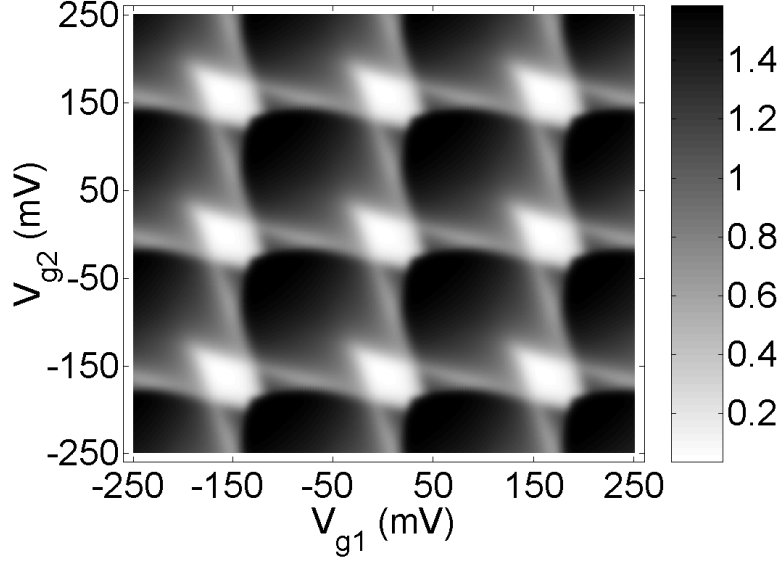The density plot of the TMR effect as a function of gate voltages is shown

Figure 3.4:   The tunnel magnetoresistance as a function of gate voltages for $V = 60$ mV. The other parameters are the same as in Fig. 3.2.

in Fig. 3.4. The results are shown for a constant and nonzero bias voltage. It can be seen that TMR varies periodically with both gate voltages. By changing gate voltages it is possible either to enhance or suppress the TMR to almost zero. Thus, the device can be used as a magnetoresistive element with gate-controlled amplitude of tunnel magnetoresistance [75].

3.3   Numerical Results in the Presence of Spin Accumulation

If the spin relaxation time is longer than the time between two successive tunneling events, a nonequilibrium magnetic moment appears on each island. In order to calculate the corresponding shifts of the Fermi level due to spin accumulation, one can use the spin current conservation equations, which for the first and second islands are given by

$$\frac{1}{e}(I_{\mathrm{M}}^{\sigma} - I_{\mathrm{L}}^{\sigma}) - \frac{\rho_{\mathrm{I}1\sigma}\Omega_{\mathrm{I}1}}{\tau_{\mathrm{sf}1}}\Delta E_{\mathrm{F}1}^{\sigma} = 0\,, \tag{3.12}$$

$$\frac{1}{e}(I_{\mathrm{R}}^{\sigma} - I_{\mathrm{M}}^{\sigma}) - \frac{\rho_{\mathrm{I}2\sigma}\Omega_{\mathrm{I}2}}{\tau_{\mathrm{sf}2}}\Delta E_{\mathrm{F}2}^{\sigma} = 0\,, \tag{3.13}$$

with $\rho_{\mathrm{I}j\sigma}$ being the spin-dependent density of states and $\Omega_{\mathrm{I}j}$ denoting the volume of the j-th island. The spin relaxation time of the j-th island is denoted by $\tau_{\mathrm{sf}j}$,

and I_r^σ is the current flowing through the r-th junction in the spin channel σ. From the above equations it is possible to calculate self-consistently the shifts of the Fermi level. For relaxation times much longer than the injection time, it is justifiable to assume that the spin currents through each junction have to be conserved, $I_L^\sigma = I_M^\sigma = I_R^\sigma$.

If the two islands are nonmagnetic, whereas the electrodes are ferromagnetic, one could expect no TMR effect. However, a finite TMR in such systems may appear due to nonequilibrium magnetic moment that builds up on the islands if the spin of tunneling electrons does not relax for sufficiently long time. In this situation the islands become magnetized, which in turn leads to nonzero tunnel magnetoresistance. When considering the case of zero temperature, assuming no charging effects and that the islands are built of the same materials, whereas the external electrodes are made from the same ferromagnets, one can write the spin currents in the antiparallel configuration as [72], $I_L^\uparrow \sim \rho_I \rho_\uparrow (-eV/2 - \Delta E_{F1}^\uparrow)$, $I_M^\uparrow \sim \rho_I^2 (\Delta E_{F1}^\uparrow - \Delta E_{F2}^\uparrow)$, $I_R^\uparrow \sim \rho_I \rho_\downarrow (-eV/2 + \Delta E_{F2}^\uparrow)$, for the spin-up electrons, and $I_L^\downarrow \sim \rho_I \rho_\downarrow (-eV/2 - \Delta E_{F1}^\downarrow)$, $I_M^\downarrow \sim \rho_I^2 (\Delta E_{F1}^\downarrow - \Delta E_{F2}^\downarrow)$, $I_R^\downarrow \sim \rho_I \rho_\uparrow (-eV/2 + \Delta E_{F2}^\downarrow)$, for the spin-down electrons. When assuming further that $\rho_\uparrow + \rho_\downarrow = 2\rho_I \equiv \rho$, it is possible to express the densities of states in terms of spin polarization p, given by Eq. (1.4), as $\rho_\uparrow = \rho(1+p)/2$ and $\rho_\downarrow = \rho(1-p)/2$. Using the spin current conservation in the limit of long relaxation time, one can determine the corresponding shifts of the Fermi levels, they read

$$\Delta E_{F1}^\uparrow = -\frac{eV}{6} - \frac{eV}{3} \frac{(3-p)p}{3-p^2} \,,$$

$$\Delta E_{F1}^\downarrow = -\frac{eV}{6} + \frac{eV}{3} \frac{(3+p)p}{3-p^2} \,,$$

$$\Delta E_{F2}^\uparrow = \frac{eV}{6} - \frac{eV}{3} \frac{(3+p)p}{3-p^2} \,,$$

$$\Delta E_{F2}^\downarrow = \frac{eV}{6} + \frac{eV}{3} \frac{(3-p)p}{3-p^2} \,.$$

It can be seen from the above equations that $\Delta E_{F1}^\sigma = -\Delta E_{F2}^{\bar\sigma}$, for $\sigma = \uparrow, \downarrow$. It is also interesting to note that ΔE_{F1}^σ and ΔE_{F2}^σ may change sign, depending on value of the spin polarization p. In a similar way one can show that for the parallel configuration there is no spin accumulation and the electrochemical potentials of the islands are $\Delta E_{F1}^\sigma = -eV/6$ and $\Delta E_{F2}^\sigma = eV/6$, irrespective of spin σ. Using calculated shifts of the Fermi level it is then easy to find the value of the TMR effect, it is given by TMR $= 2p^2/(3 - 3p^2)$. This value of TMR corresponds to one third of the Jullière's value. It is worth noting that in the case of single-electron transistors with nonmagnetic islands, TMR was found to be equal to a half of the Jullière's value [72]. Thus, TMR decreases as the number of islands is increased.

Once the charging effects become important and there is an asymmetry between barriers, the situation becomes more complex and analytical analysis is not
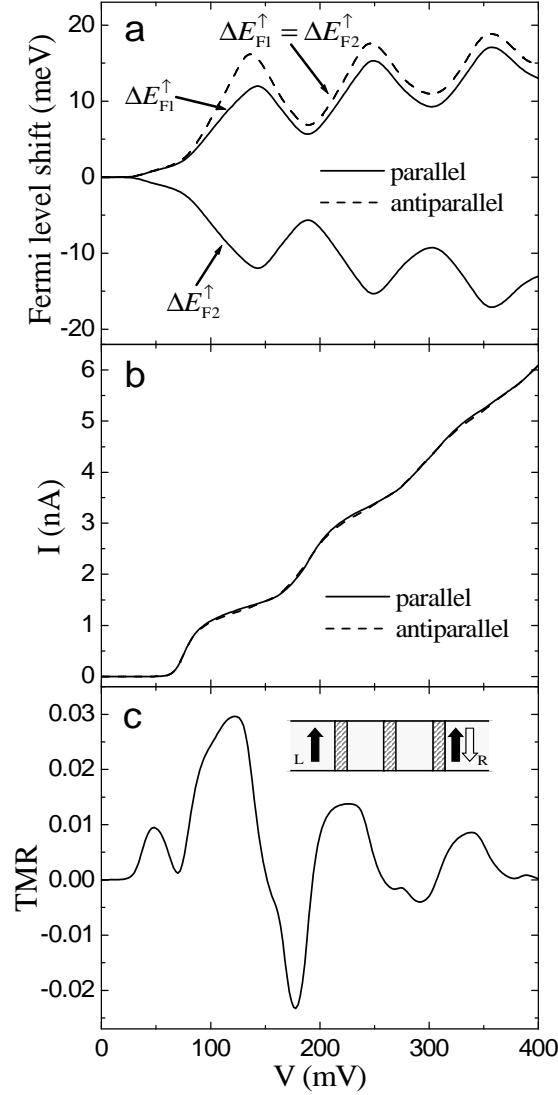
Figure 3.5: The shifts of the Fermi levels for spin-up electrons (a), currents in the parallel and antiparallel configurations (b) and TMR (c) as a function of the bias voltage. The parameters are: $C_1 = C_2 \equiv C = 3C_M = 3$ aF, $k_B T/(e^2/2C) = 0.05$, $\beta_1 = \beta_2 = 1$, $\tau_{sf1} \rightarrow \infty$, $\tau_{sf2} = \rightarrow \infty$, $\alpha_L = \alpha_R = 5$, $\alpha_M = 1$, whereas $R_L^P = R_R^P = R_M^P/50 = 1$ MΩ. In the antiparallel configuration, $R_{L\sigma}^{AP} = R_{L\sigma}^P$, $R_{R\sigma}^{AP} = R_{R\bar{\sigma}}^P$.

too straightforward. In this case, the associated spin accumulation is analyzed numerically. Figure 3.5 shows the shifts of the Fermi levels and currents in the parallel and antiparallel configurations, as well as the resulting TMR calculated in the limit of long spin relaxation time for the system built of ferromagnetic electrodes and nonmagnetic islands. The magnetic moments of external electrodes can form either parallel or antiparallel configurations, as illustrated in the
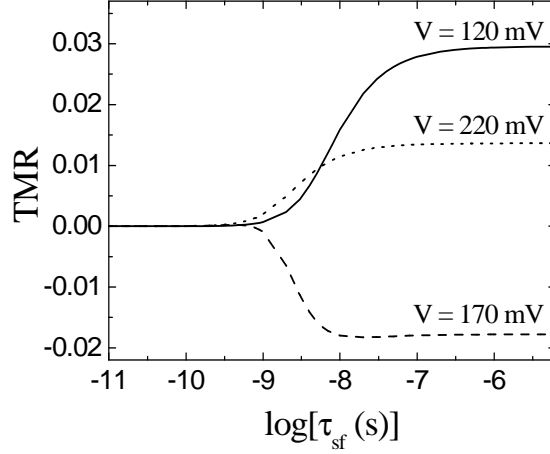
Figure 3.6:   TMR calculated for different values of bias voltage as a function of relaxation time for $\tau_{\text{sf1}} = \tau_{\text{sf2}} = \tau_{\text{sf}}$ and $\rho_{\text{I1}}\Omega_{\text{I1}} = \rho_{\text{I2}}\Omega_{\text{I2}} = 1000/\text{eV}$. The other parameters are the same as in Fig. 3.5.

inset of Fig. 3.5c. First of all, it can be seen that nonequilibrium spin accumulation, shown in Fig. 3.5a, exists not only in the antiparallel configuration but also in the parallel configuration. In the antiparallel configuration the shifts of the Fermi level for a given spin orientation are equal, whereas in the parallel configuration they are opposite. Furthermore, the effects due to discrete charging lead to an oscillatory behavior of the Fermi level shift, in a similar way as in the case of single-electron transistors with nonmagnetic islands discussed in the previous chapter. The currents flowing through the system in both magnetic configurations are shown in Fig. 3.5b. Characteristic Coulomb steps due to single-electron charging are clearly visible. Moreover, because of nonequilibrium spin accumulation induced on the islands, the currents flowing in the parallel and antiparallel configurations are different. This difference, in turn, leads to nonzero tunnel magnetoresistance, as displayed in Fig. 3.5c. It can be seen that TMR oscillates as a function of the bias voltage and the amplitude of these oscillations decreases with increasing the voltage. Furthermore, the TMR may change sign, depending on the value of transport voltage. These effects are clearly due to accumulated magnetic moments on the islands. If spin relaxation time becomes shorter than the time between successive tunneling events, spin accumulation disappears and, consequently, TMR also vanishes. This is shown in Fig. 3.6, where the TMR is plotted for several values of the bias voltage as a function of spin relaxation time. The values of bias voltage correspond to maximal and minimal values of TMR, see Fig. 3.5c. Moreover, it can also be seen that the crossover from the limit of fast relaxation time to the limit of short relaxation time takes place for τ_{sf} of the order of 10^{-8} s.

Transport characteristics as a function of the gate voltage are shown in Fig. 3.7
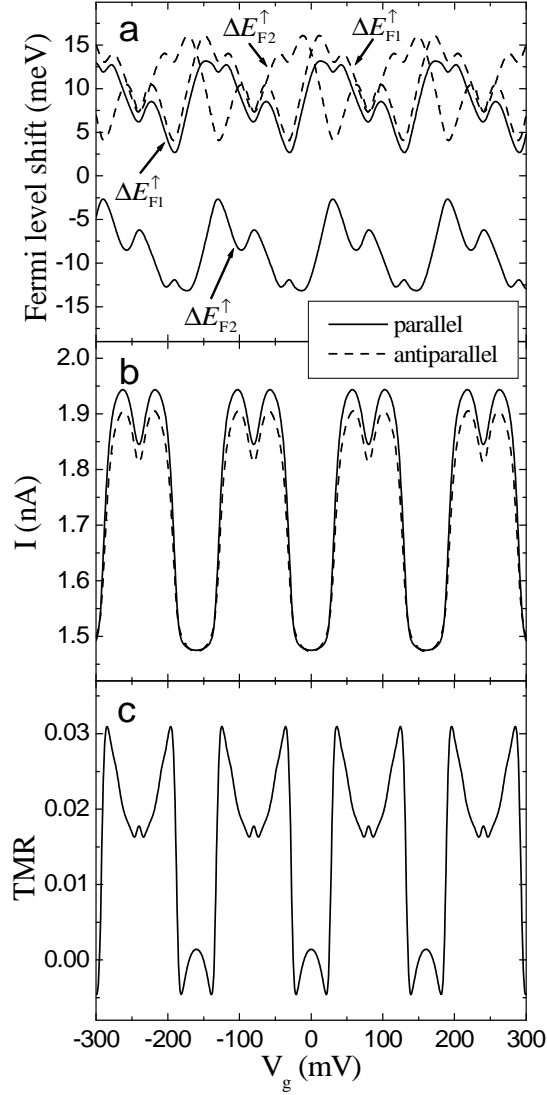
Figure 3.7:   The gate voltage dependence of the Fermi level shifts for spin-up electrons (a), currents in the parallel and antiparallel configurations (b) and resulting TMR (c) for $V_{g1} = V_{g2} = V_g$ and $V = 150\text{mV}$. The other parameters are the same as in Fig. 3.5.

for $V_{g1} = V_{g2} = V_g$ and for bias voltage $V = 150$ mV. The value of bias voltage corresponds to the middle of the first Coulomb step in the respective I-V curves. At this voltage the spin accumulation has local maximum, see Fig. 3.5a. The Fermi level shifts oscillate as a function of the gate voltage, as presented in Fig. 3.7a. The shifts of the Fermi level in the antiparallel configuration are symmetric with respect to $V_g = 0$, for the parallel configuration, however, their dependence on gate voltage is more complex. The Coulomb oscillations of elec-

Figure 3.8:   The density plot of TMR as a function of both gate voltages for $V = 170$ mV. The other parameters are the same as in Fig. 3.5.

tric current in the parallel and antiparallel magnetic configurations are depicted in Fig. 3.7b, whereas TMR is displayed in Fig. 3.7c. It can be seen that TMR exhibits an oscillatory behavior as a function of gate voltage. Moreover, TMR changes sign when sweeping the gate voltage. As a consequence, 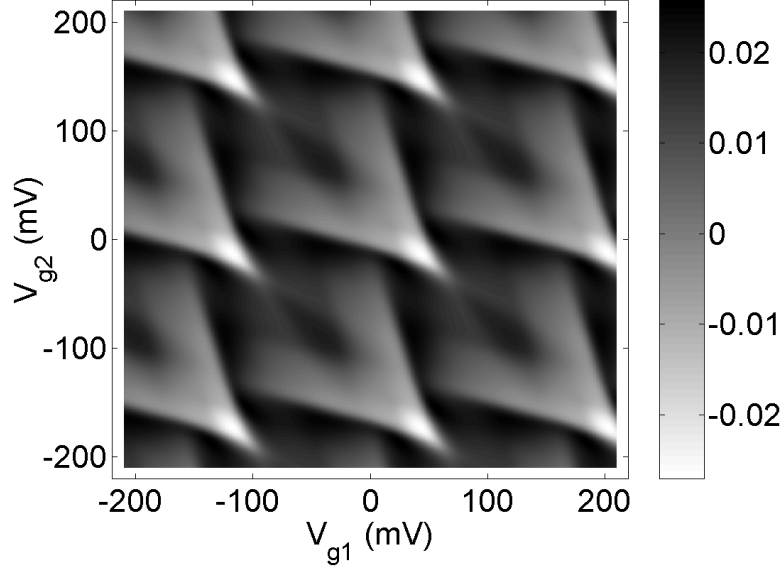by applying appropriate gate voltages, it is possible to tune the magnitude of TMR from positive to negative values. This is also shown in Fig. 3.8, which presents the density plot of tunnel magnetoresistance as a function of both gate voltages calculated for $V = 170$ mV. This value of bias voltage corresponds to the minimal value of TMR, see Fig. 3.5c.

Some further interesting effects appear in systems built of ferromagnetic islands with long spin relaxation time. In this situation, nonequilibrium magnetic moments due to spin accumulation can also appear on the islands. Because the islands are ferromagnetic, the ratio of the Fermi level shifts for spin-up and spin-down electrons is not equal to unity, as was in the case of nonmagnetic islands, but depends on the ratio of the corresponding spin-dependent densities of states of islands. Transport characteristics of system consisting of ferromagnetic islands and nonmagnetic leads are shown in Fig. 3.9. In particular, the shifts of the Fermi levels in the parallel and antiparallel configurations are shown in Fig. 3.9a, whereas the current is shown in Fig. 3.9b. As the current flowing in the antiparallel configuration presents a typical Coulomb staircase characteristic, the behavior of current flowing in the parallel configuration is more complex. It can be seen that once a Coulomb step is reached, the current starts decreasing in some range of bias voltage, thus, leading to negative differential conductance, as shown in
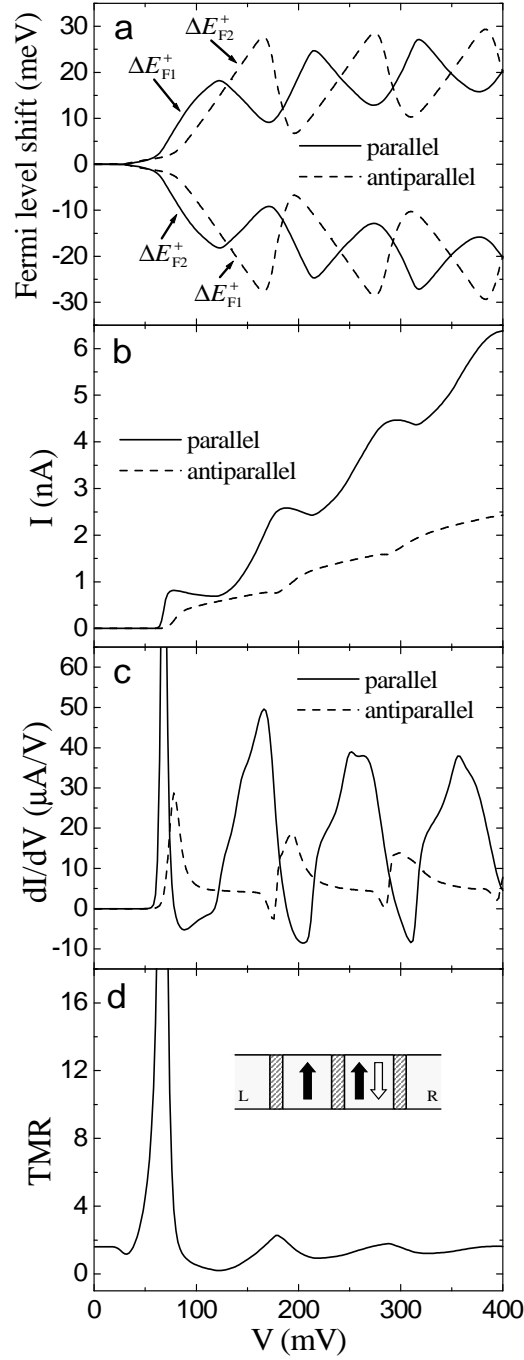
Figure 3.9: The shifts of the Fermi levels for majority-spin electrons (a), currents (b) and differential conductance (c) in the parallel and antiparallel configurations and the TMR effect (d) as a function of the bias voltage. The parameters are: $C_1 = C_2 \equiv C = 3C_M = 3$ aF, $k_B T/(e^2/2C) = 0.03$, $\beta_1 = \beta_2 = 0.2$, $\tau_{sf1} \to \infty$, $\tau_{sf2} \to \infty$, $\alpha_L = \alpha_R = 5$, $\alpha_M = 25$, whereas $R_L^P = R_R^P = R_M^P/50 = 1$ MΩ. In the antiparallel configuration, $R_{L\sigma}^{AP} = R_{L\sigma}^P$, $R_{M\uparrow}^{AP} = R_{M\downarrow}^{AP} = (R_{M\uparrow}^P R_{M\downarrow}^P)^{1/2}$, and $R_{R\sigma}^{AP} = R_{R\bar{\sigma}}^P$.
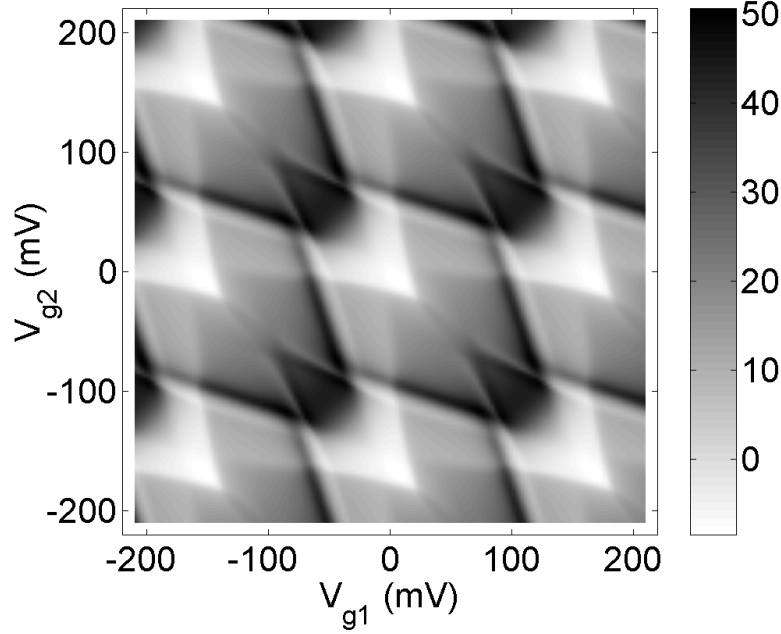
Figure 3.10: The density plot of differential conductance dI/dV (μA/V) in the parallel configuration as a function of both gate voltages for $V = 200$ mV. The other parameters are the same as in Fig. 3.9.

Fig. 3.9c. It is further clearly visible that negative differential conductance exists only in the parallel configuration and is absent in the antiparallel configuration. The occurrence of negative differential conductance, however, depends on the parameters of the system. As shown in the sequel, negative differential conductance may also exist in the antiparallel configuration. Moreover, it can be observed that differential conductance oscillates as a function of bias voltage and the oscillations reflect the step-like current-voltage dependence. Furthermore, it is worth noting that the period of conductance oscillations in the parallel configuration is slightly modified as compared to that in the antiparallel configuration. The effect of modified period of Coulomb staircase for different magnetic configurations is due to spin accumulation and was already predicted theoretically for single-electron transistors [55]. The TMR effect corresponding to I-V curves shown in Fig. 3.9b is displayed in Fig. 3.9d. The oscillatory behavior of TMR as a function of the bias voltage is clearly visible. Furthermore, the TMR exhibits a large maximum at transport voltage corresponding to the first Coulomb step, the amplitude of TMR, however, decreases with increasing bias voltage.

The conductance through the system can be tuned by applying gate voltages. This is illustrated in Fig. 3.10, where differential conductance in the parallel configuration is plotted as a function of both gate voltages for $V = 200$ mV. At this value of bias voltage the differential conductance becomes negative, see
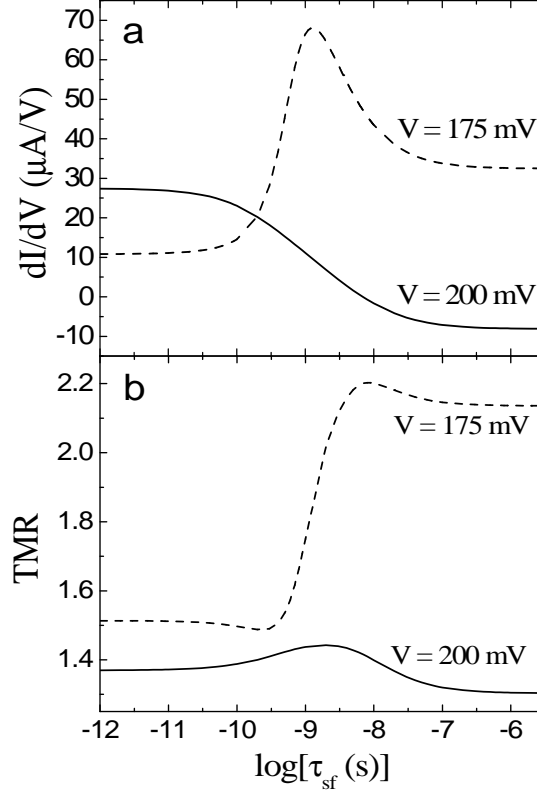
Figure 3.11:   The differential conductance in the parallel configuration (a) and the TMR effect (b) as a function of spin relaxation time for different values of the bias voltage and $\tau_{\mathrm{sf1}} = \tau_{\mathrm{sf2}} = \tau_{\mathrm{sf}}$, $\rho_{\mathrm{I\uparrow1}}\Omega_{\mathrm{I1}} = \rho_{\mathrm{I\uparrow2}}\Omega_{\mathrm{I2}} = 1000/\mathrm{eV}$. The other parameters are the same as in Fig. 3.9.

Fig. 3.9c. It can be seen that differential conductance varies periodically with gate voltages. Thus, by applying respective gate voltages one can change value of the differential conductance from positive to negative.

The negative differential conductance occurs due to nonequilibrium spin accumulation on the islands and disappears in the limit of fast spin relaxation time. Figure 3.11 presents differential conductance in the parallel configuration and the TMR effect as a function of the relaxation time for two values of the bias voltage. The first one, $V = 175$ mV, corresponds to the second Coulomb step, whereas the second one, $V = 200$ mV, corresponds to the voltage where differential conductance is negative, see Fig. 3.9. Consider first the case of $V = 175$ mV. As the relaxation time becomes longer, both the differential conductance and TMR increase, as illustrated in Fig. 3.11a and b. It is further interesting to note that this increase is nonmonotonic – there is a peak in differential conductance and a slight dip in the TMR effect at relaxation time corresponding to the time between successive tunneling events. For $V = 200$ mV, on the other hand, the differen-

tial conductance decreases and changes its sign as the relaxation time becomes longer – it is positive in the limit of fast relaxation, whereas in the limit of slow spin relaxation differential conductance becomes negative. Furthermore, it can be seen that the TMR effect is larger in the limit of fast spin relaxation than in the limit of slow spin relaxation. This behavior is opposite to the one observed for $V = 175$ mV. Moreover, at the crossover between those two limits there is a slight maximum in TMR. Thus, both differential conductance and the TMR effect exhibit distinctively different behavior as a function of the relaxation time, depending on value of the bias voltage and, consequently, spin accumulation.

Recently, several experiments on spin-polarized transport through granular systems were reported [42, 43, 54, 69, 80]. For example, in Ref. [54], the tunneling current was driven from a tip of scanning tunneling microscope through ferromagnetic grains to ferromagnetic electrode. Transport measurements of such devices showed pronounced Coulomb steps in the current-voltage characteristics. Moreover, negative differential conductance was observed. It was further proposed that the mechanism responsible for occurrence of negative differential conductance could be nonequilibrium spin accumulation. Such systems can be modelled theoretically by double-island devices whose two islands and the right electrode are ferromagnetic, whereas the left electrode is nonmagnetic, corresponding to nonmagnetic tip of scanning tunneling microscope, see the inset of Fig. 3.12c. Transport characteristics of such device are displayed in Fig. 3.12. The parameters used to generate this figure correspond to the parameters taken from Ref. [54]. In calculations the nonequilibrium spin accumulation was also taken into account. The shifts of the Fermi level for spin-up electrons are shown in Fig. 3.12a. The oscillations of spin accumulation are clearly evident. Furthermore, the Fermi level shifts on the islands are different in both magnetic configurations. Generally, spin accumulation on the first island is larger than the accumulation on the second island. The reason for this is the fact that the rate for electron tunneling from the first island to the left lead is smaller than the rate for tunneling of electrons to or from the second island, which is due to asymmetry of barriers. The currents flowing through the system in the parallel and antiparallel configurations are illustrated in Fig. 3.12b. The I-V curves present the typical Coulomb staircase characteristics. Moreover, negative differential conductance occurs in both magnetic configurations, however, it is more pronounced in the antiparallel configuration, as shown in Fig. 3.12c. It can be seen that negative differential conductance increases with increasing the bias voltage. These numerical results are in good agreement with experimental data presented in Ref. [54]. The resulting TMR effect is displayed in Fig. 3.12d. The oscillatory behavior of TMR with bias voltage is visible. Furthermore, it is interesting to note that TMR oscillates between negative and positive values.

In order to present more clearly the effect of spin accumulation on transport characteristics, in Fig. 3.13 we show the electric current for parallel and antiparallel configurations and resulting TMR calculated in the limit of fast spin
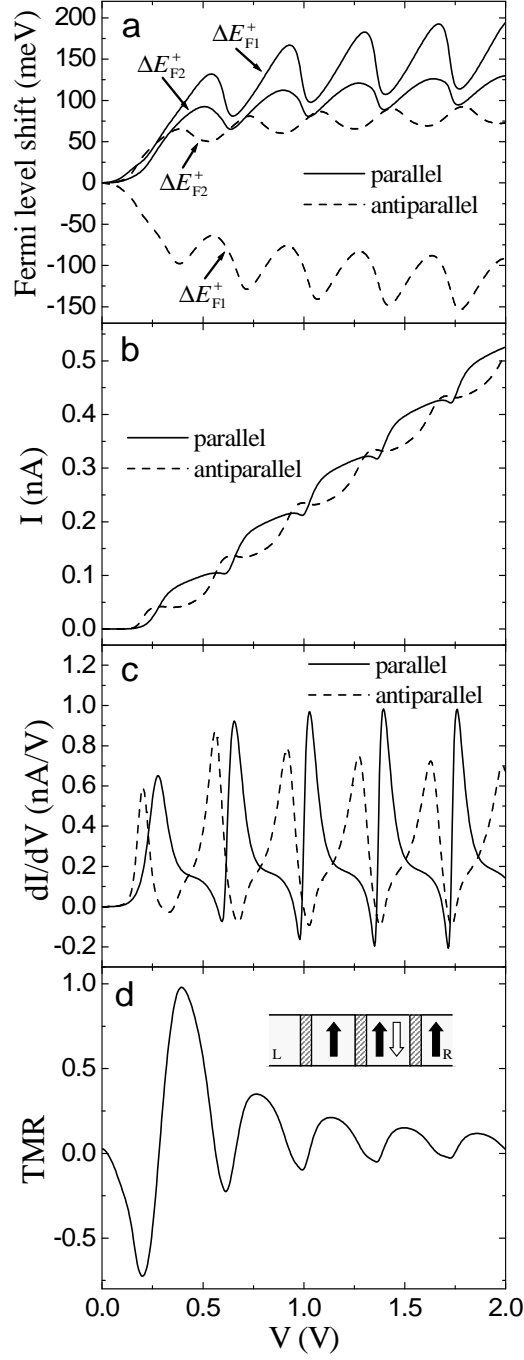
Figure 3.12: The shifts of the Fermi levels for majority-spin electrons (a), currents (b) and differential conductance (c) in the parallel and antiparallel configurations, and the resulting TMR (d) as a function of the bias voltage. The parameters are: $T = 140$ K, $C_L = 0.45$ aF, $C_M = 0.2$ aF, $C_R = 0.35$ aF, $C_{g1} = C_{g2} = 0$, $\alpha_L^2 = \alpha_M = \alpha_R = 25$, and $\beta_1 = \beta_2 = 0.2$, whereas $\tau_{sf1} = \tau_{sf2} = \infty$. The total junction resistances are $R_L = 3500$ MΩ, $R_M = R_R = 1$ MΩ. In the antiparallel configuration, $R_{L\sigma}^{AP} = R_{L\sigma}^{P}$, and $R_{r\uparrow}^{AP} = R_{r\downarrow}^{AP} = (R_{r\uparrow}^{P} R_{r\downarrow}^{P})^{1/2}$, for $r = M, R$.
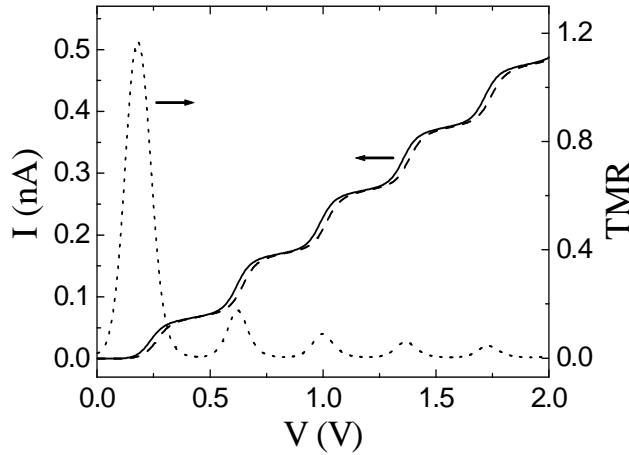
Figure 3.13:   The currents flowing in the parallel (solid line) and antiparallel (dashed line) configurations and resulting TMR (dotted line) as a function of the bias voltage in the limit of short relaxation time. The other parameters are the same as in Fig. 3.12.

relaxation time. In this limit there is no associated spin accumulation because the electron spin relaxes before next tunneling event takes place. First of all, it can be seen that the negative differential conductance vanishes in the limit of fast spin relaxation time and the current-voltage curves present typical Coulomb staircase characteristics. Furthermore, although the TMR effect still exhibits an oscillatory behavior as a function of bias voltage, its value is always positive and the amplitude of oscillations is much suppressed. The dependence of tunnel magnetoresistance on bias voltage displays small peaks at the Coulomb steps, otherwise TMR tends to zero.

In the case of analyzed systems, the negative differential conductance occurs due to nonequilibrium spin accumulation on the islands. It is however worth noting that the negative differential conductance may also exist in single-electron devices built of nonmagnetic materials [78, 81].

To summarize, one of the main effects caused by nonequilibrium spin accumulation on the islands is negative differential conductance. Furthermore, spin accumulation also influences TMR – it oscillates as a function of bias voltage between positive and negative values. These effects are clearly due to spin accumulation and disappear once the relaxation time becomes shorter than the time between successive tunneling events.

3.4   Spin Pumps

The possibility of pumping electrons one by one through nonmagnetic double-island devices was already proposed and demonstrated in the past decade [4, 82, 83]. In order to pump single electrons, one has to apply two gate voltages, shifted in phase by $\pi/2$, to the islands. In this case, by changing continuously the potentials of the islands, the electrons are pumped through the system one per cycle. Such device is called single-electron pump. If, in turn, the electrodes are made of ferromagnetic material the current is spin-polarized. The spin polarization of such current depends on the parameters of the system. Consequently, such device may be used for pumping electrons with a given spin orientation. The possibility of pumping single electrons in ferromagnetic double-island devices was proposed in Ref. [76]. In this work the process of pumping was obtained by applying alternating magnetic field which caused the shift of electrochemical potentials of the islands.

In this section we show that in the case of ferromagnetic double-island devices one can also pump electrons with given spin orientation by attaching two
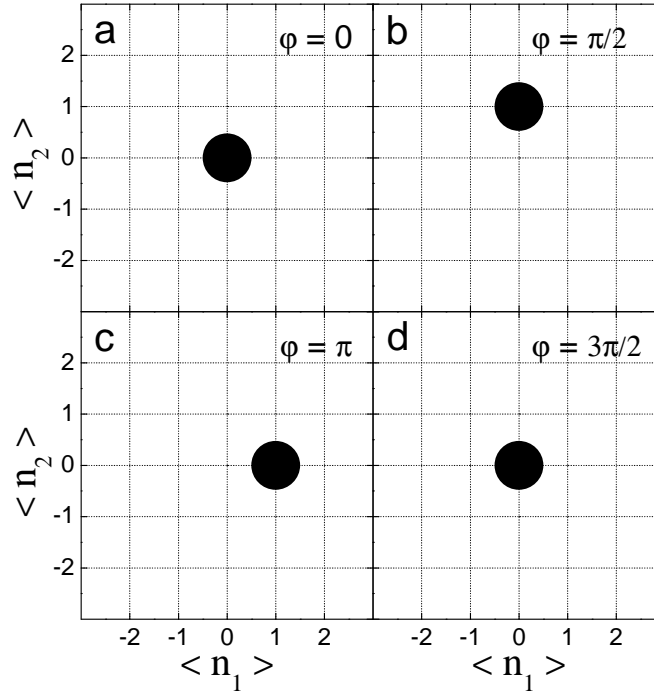

Figure 3.14: The average number of excess electrons on the islands in the linear response regime for $V_{g1} = V_{g0} + V_{gA} \cos \varphi$ and $V_{g2} = V_{g0} + V_{gA} \cos (\varphi + \pi/2)$, with $V_{g0} = 50$ mV and $V_{gA} = -70$ mV. The other parameters are the same as in Fig. 3.2.

alternating gate voltages to the islands. In the following, it is assumed that the frequency of the gate voltages is low as compared to the time between successive tunneling events, so that the system is always in a well-defined charge state (n_1, n_2). We consider the system built of two ferromagnetic islands and nonmagnetic leads, as illustrated in the inset of Fig. 3.2c, and assume that the leads are magnetized in parallel. Figure 3.14 displays the average electron number on the islands in the linear response regime at different phases of the gate voltages, $\varphi = 0, \pi/2, \pi, 3\pi/2$. The voltage V_{g0} is chosen in this way so that the system is close to the degeneracy point where three charge states are possible, namely, $(0, 0)$, $(0, 1)$ and $(1, 0)$. As can be seen in Fig. 3.14a, for $\varphi = 0$ there are no excess electrons on the islands and the system is in the charge state $(0, 0)$. Then, as the time goes by, an electron from the right lead tunnels into the second island and, consequently, the system is in the charge state $(0, 1)$. This situation occurs for $\varphi = \pi/2$, as shown in Fig. 3.14b. In turn in the case of $\varphi = \pi$, the charge state of the system changes into $(1, 0)$, see Fig. 3.14c. This happens by tunneling of an electron from the second island to the first one. Then, the electron from the first island tunnels further to the left lead and the system is again in the charge state $(0, 0)$, as illustrated in Fig. 3.14d for $\varphi = 3\pi/2$. This scenario repeats with each period of the gate voltage effectively giving rise to the process of single-electron pumping. Because the system is ferromagnetic the pumped current is spin-polarized. The spin-polarization of pumped electrons η, given by Eq. (2.8), depends on the parameters of the system, in particular, on the spin asymmetry of barriers. For the parameters assumed here $\eta = -2/3$.

Part II

Spin-Polarized Transport through Quantum Dots

In the previous part spin-polarized transport through single-electron devices was discussed. The central mesoscopic electrodes were assumed to have sufficiently small dimensions, so that the energy associated with addition of a single electron was the most relevant energy scale. The level quantization of the islands, however, was still negligible. If, nevertheless, the size of the island is reduced further, the energy spectrum becomes quantized and only a few discrete energy levels contribute to the conductance. In this case one arrives at slightly more sophisticated systems – the ones based on quantum dots (QDs) or molecules. Quantum dots are man-made structures consisting of a small number of free electrons, which can range from zero to a few hundreds [7]. The energy spectrum of quantum dots is quantized in a way resembling that of atoms, therefore, quantum dots are also frequently called *artificial atoms* [84, 85].

Quantum dots have already paved their way to become underlying devices of spintronics not only because of beautiful physics emerging in those systems, but, more importantly, due to possible future applications and due to the possibility of manipulation of a single spin [7, 40, 86, 87]. The transport properties of quantum dots coupled to nonmagnetic leads have already been extensively studied both theoretically and experimentally [7, 22, 27, 28, 86, 87, 88, 89]. Some further interesting effects occur in the case of quantum dots coupled to ferromagnetic leads. Certain aspects of spin-dependent transport through quantum dots have already been considered theoretically. For example, the TMR effect was thoroughly analyzed in the limit of sequential tunneling, and the influence of spin-flip relaxation processes in the dot on TMR was discussed [90, 91, 92]. Furthermore, the dependence of the first-order conductance through a quantum dot on the angle between magnetic moments of the leads was also considered [93, 94, 95, 96]. However, in some cases considerations taking into account only first-order processes are not sufficient. The first-order contribution is only dominant for transport voltages exceeding the threshold voltage, whereas for voltages below the threshold, the system is in the Coulomb blockade regime and the sequential tunneling is suppressed, see section 1.2.2. Although the first-order tunneling in the Coulomb blockade regime is prohibited by energy conservation, the current can still be mediated by higher-order processes such as cotunneling [22, 29, 30, 33]. The cotunneling current through quantum dots was studied both experimentally [97, 98, 99, 100] and theoretically [101, 102, 103, 104, 105, 106]. Contrarily to the case of metallic islands, the cotunneling current through quantum dots was found to be linear with the applied voltage [101]. It was shown that the second-order contribution leads to renormalization of the dot level and the dot-lead coupling strength [102]. Furthermore, the resonant tunneling regime in the case of quantum dots coupled to ferromagnetic leads was also considered [107, 108].

This part of the thesis presents a thorough analysis of transport through single-level quantum dots weakly coupled to ferromagnetic leads both in the se-

quential and cotunneling regimes in the full range of parameters[1]. In particular, it is shown that the tunnel magnetoresistance displays distinctively different behavior depending on the transport regime. Furthermore, a new zero-bias anomaly is found in differential conductance when the leads are magnetized antiparallel to each other. The effect of intrinsic spin relaxation on the dot on conductance in the Coulomb blockade regime is also analyzed. Moreover, the problem of cotunneling transport through quantum dots coupled to ferromagnetic leads with noncollinear alignment of magnetic moments is addressed.

The systems studied in this chapter may be realized experimentally in various ways, including ultrasmall aluminum nanoparticles [40], single molecules [109], self-assembled dots in ferromagnetic semiconductors [119], or carbon nanotubes [120, 121, 122, 123, 124].

---

[1]Another interesting situation occurs in the case when the dot is strongly coupled to external leads. The Kondo physics emerges then at sufficiently low temperatures [109, 110, 111, 112, 113, 114]. In order to analyze the Kondo effect [115], one needs to employ some nonperturbative methods such as, for example, the numerical renormalization group method [116, 117, 118]. These very interesting issues, however, go beyond the scope of the present thesis.

Chapter 4

Transport through Quantum Dots Coupled to Ferromagnetic Leads with Collinear Magnetizations

In this chapter transport through a single-level quantum dot weakly coupled to ferromagnetic leads is analyzed in the full range of parameters. It is assumed that magnetic moments of the electrodes are collinear. The considerations are based on the real-time diagrammatic technique and tunneling contributions of the first and second order in the tunnel-coupling strength are taken into account. The dot occupation probabilities, current and resulting tunnel magnetoresistance, as well as the differential conductance are calculated in both the linear and nonlinear response regimes. Furthermore, the impact of intrinsic spin relaxation processes in the dot on the conductance in the Coulomb blockade regime is analyzed.

4.1 Description of Model

A schematic of a single-level quantum dot is presented in Fig. 4.1. The dot is weakly coupled to two ferromagnetic electrodes whose magnetizations are collinear. Thus, the orientations of the lead magnetic moments can be either parallel or antiparallel. Extension to a noncollinear case, however, is straightforward. There is also a gate voltage attached to the dot.

The system is modelled by an Anderson-like Hamiltonian of the form [125]

$$H = H_{\mathrm{L}} + H_{\mathrm{R}} + H_{\mathrm{D}} + H_{\mathrm{T}} . \qquad (4.1)$$

The first and second terms represent the left and right reservoirs of noninteracting electrons, $H_r = \sum_{q\sigma} \varepsilon_{rq\sigma} c_{rq\sigma}^\dagger c_{rq\sigma}$, for $r = \mathrm{L}, \mathrm{R}$, where $c_{rq\sigma}^\dagger$ ($c_{rq\sigma}$) is the creation (annihilation) operator of an electron with wave number q and spin σ in the
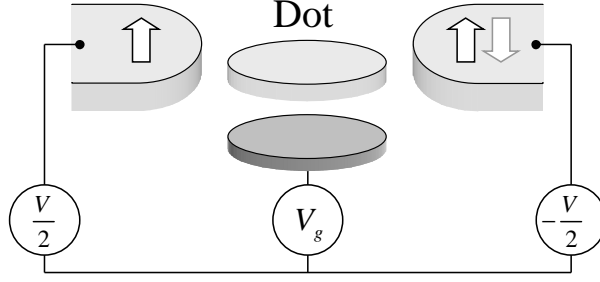
Figure 4.1: Schematic of a single-level quantum dot coupled to ferromagnetic leads. The magnetic moments of external electrodes can be aligned either in parallel or antiparallel. The system is symmetrically biased and there is a gate voltage attached to the dot.

lead r, whereas $\varepsilon_{rq\sigma}$ denotes the corresponding single-particle energy. The second part of the Hamiltonian, H_{D}, represents the dot and involves two terms. The first term describes noninteracting electrons on the dot, whereas the second term represents the Coulomb interaction described by the correlation energy U. The dot Hamiltonian can be then expressed as

$$H_{\mathrm{D}} = \sum_{\sigma=\uparrow,\downarrow} \varepsilon_\sigma d_\sigma^\dagger d_\sigma + U d_\uparrow^\dagger d_\uparrow d_\downarrow^\dagger d_\downarrow \,, \qquad (4.2)$$

where $\varepsilon_\sigma = \varepsilon \mp \Delta/2$ is the energy of an electron on the dot with spin σ and $d_\sigma^\dagger$ (d_σ) is the corresponding creation (annihilation) operator. The position of the dot level can be tuned by the gate voltage, but is independent of the symmetrically-applied transport voltage. Furthermore, the dot level may be spin-split due to for example a stray field of the electrodes or an external magnetic field. The corresponding level splitting is denoted by Δ, whereas ε is the energy of the spin-degenerate dot level ($\Delta = 0$). Because of the finite Coulomb energy U, there are four different states of the dot possible – empty dot ($\chi = 0$), singly occupied dot with a spin-up ($\chi = \uparrow$) or spin-down ($\chi = \downarrow$) electron, and doubly occupied dot ($\chi = \mathrm{d}$), where $|\chi\rangle$ are the corresponding eigenfunctions. This results in a four-by-four density matrix for the quantum dot subsystem.

Interaction between the leads and quantum dot is incorporated in the tunneling Hamiltonian, H_{T}, given by

$$H_{\mathrm{T}} = \sum_{r=\mathrm{L,R}} \sum_{q\sigma} \left(t_{rq\sigma} c_{rq\sigma}^\dagger d_\sigma + t_{rq\sigma}^* d_\sigma^\dagger c_{rq\sigma} \right) \,, \qquad (4.3)$$

where $t_{rq\sigma}$ are the tunnel matrix elements. Tunneling gives rise to an intrinsic broadening Γ^σ of the dot levels, $\Gamma^\sigma = \sum_{r=\mathrm{L,R}} \Gamma_r^\sigma$. The parameters $\Gamma_r^\uparrow$ and $\Gamma_r^\downarrow$ describe contributions to the level widths due to coupling of the dot to the lead r. The respective contribution Γ_r^σ can be expressed in terms of the Fermi golden

rule as $\Gamma_r^\sigma = 2\pi \sum_q |t_{rq\sigma}|^2 \delta(\omega - \varepsilon_{rq\sigma})$. Assuming the tunnel matrix elements $t_{rq\sigma}$ to be independent of the wave number, one gets

$$\Gamma_r^\sigma = 2\pi |t_{r\sigma}|^2 \rho_{r\sigma} \,, \tag{4.4}$$

with $\rho_{r\sigma}$ denoting the spin-dependent density of states in the lead r. In order to parameterize the system in the most intuitive way, the couplings are expressed in terms of the spin polarization p_r of the lead r, given by Eq. (1.4), as $\Gamma_r^{\uparrow(\downarrow)} = \Gamma_r(1 \pm p_r)$, where $\Gamma_r = (\Gamma_r^\uparrow + \Gamma_r^\downarrow)/2$. In general, the leads may have different spin polarizations and/or coupling strengths to the dot. In the following it is assumed $\Gamma_L = \Gamma_R \equiv \Gamma/2$ and $p_L = p_R \equiv p$.

4.2   Real-Time Diagrammatic Technique

In order to investigate transport properties of the system the real-time diagrammatic technique is employed [102, 126, 127, 128, 129]. A starting point for setting up a diagrammatic description is an expansion of an expectation value of an operator O at time t with respect to the tunneling Hamiltonian[1]

$$\langle O(t) \rangle = \tag{4.5}$$
$$\mathrm{Tr}\left\{ \rho_0 \sum_{n=0}^{\infty} (-i)^n \int_K d\tau_1 \int_K d\tau_2 \ldots \int_K d\tau_n T_K \left[H_T(\tau_1)_I H_T(\tau_2)_I \ldots H_T(\tau_n)_I O(t)_I \right] \right\},$$

where the integrals are with respect to the Keldysh contour and T_K is the time ordering operator, which orders all the following operators along the Keldysh contour in such way that the operators with later time (on the Keldysh contour) go at a leftmost position, for example, $T_K[H_T(\tau_1)_I H_T(\tau_2)_I] = H_T(\tau_1)_I H_T(\tau_2)_I$, for $\tau_1 > \tau_2$. The subscript "I" by the operators denotes that they are written in the interaction picture. It is assumed that the initial density matrix ρ_0 of the whole system factorizes into the density matrices for the quantum dot and the leads, $\rho_0 = \rho_0^D \rho_0^L \rho_0^R$. The electrons in the leads are described by Fermi functions, whereas the corresponding density matrix is given by the grand canonical distribution function. Thus, one can employ the Wick's theorem to the lead Fermi operators and integrate out the degrees of freedom of the leads. The Wick's theorem, however, can not be applied to the dot operators because the dot Hamiltonian, Eq. (4.2), is biquadratic with respect to Fermi operators. Thus, these terms have to be calculated explicitly. As a results, one obtains a reduced density matrix encompassing only the dot degrees of freedom, i.e., $\chi = 0, \uparrow, \downarrow, \mathrm{d}$.

The time evolution of the reduced system can be represented graphically as a sequence of irreducible diagrams on the Keldysh contour. An example of such time evolution is illustrated in Fig. 4.2, where the upper and lower branches of

---

[1]In particular, in the case considered here, the operators to be expanded are the current operator and the density matrix.
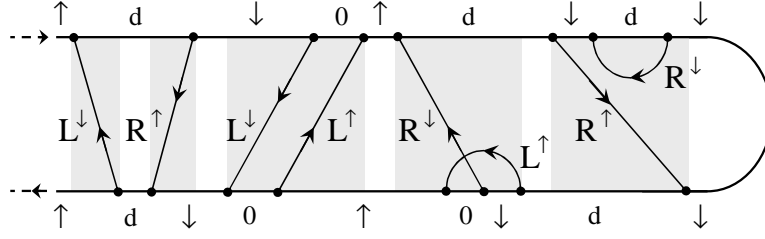
Figure 4.2: An example of time evolution of the reduced density matrix. The grey regions correspond to the irreducible diagrams of the first and second order in tunneling processes, respectively. Each tunneling line indicates whether an electron leaves or enters the dot, thus, leading to a change of the dot state, as indicated on the forward and backward Keldysh propagators.

the Keldysh contour represent the forward and backward propagators, to which the respective dot states are assigned. The vertices on the propagators correspond to the products of Fermi operators of the leads and the dot. It is further necessary to distinguish between the vertices originating from the expansion of the tunnel Hamiltonian (they are referred to as *internal* vertices) and the vertices related to the operator, of which the expectation value is calculated (those are the *external* vertices). Furthermore, the vertices are connected by tunneling lines representing the contractions of the lead operators. Each tunneling line acquires an arrow indicating whether an electron with respective spin leaves or enters the dot through the corresponding junction. The grey regions in Fig. 4.2 mark the irreducible diagrams of the first order (diagrams with one tunneling line) and the second order (diagrams with two overlapping tunneling lines) in the dot-lead coupling strength Γ. By an irreducible diagram one means a diagram in which any vertical line drawn between two neighboring vertices on the real axis crosses at least one tunneling line.
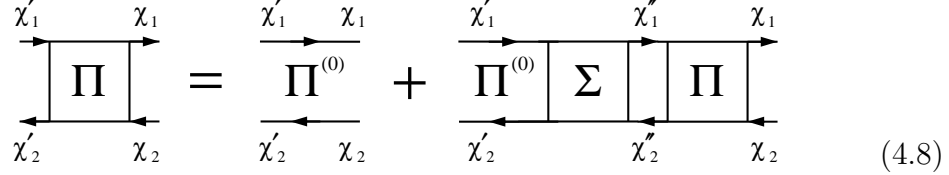
The propagation of the reduced system can be expressed by the reduced propagator $\Pi^{\chi_1\chi_1'}_{\chi_2\chi_2'}(t,t')$, corresponding to the propagation forward in time from state χ_1' at time t' to state χ_1 at time t and then backward in time from state χ_2 at time t to state χ_2' at time t'. An element of the reduced density matrix at time t, $P^{\chi_1}_{\chi_2}(t)$, can be then written as [102]

$$P^{\chi_1}_{\chi_2}(t) = \sum_{\chi_1',\chi_2'} \Pi^{\chi_1\chi_1'}_{\chi_2\chi_2'}(t,t')P^{\chi_1'}_{\chi_2'}(t')\,, \tag{4.6}$$

the propagator, in turn, is given by a Dyson equation of the form [102]

$$\Pi^{\chi_1\chi_1'}_{\chi_2\chi_2'}(t,t') = \Pi^{(0)\chi_1}_{\chi_2}(t,t')\delta_{\chi_1,\chi_1'}\delta_{\chi_2,\chi_2'} \tag{4.7}$$

$$+ \sum_{\chi_1'',\chi_2''} \int_{t'}^{t} dt_2 \int_{t'}^{t_2} dt_1 \Pi^{(0)\chi_1}_{\chi_2}(t,t_2)\Sigma^{\chi_1\chi_1''}_{\chi_2\chi_2''}(t_2,t_1)\Pi^{\chi_1''\chi_1'}_{\chi_2''\chi_2'}(t_1,t')\,.$$

48

Here, $\Sigma_{\chi_2\chi_2'}^{\chi_1\chi_1'}(t,t')$ is an irreducible self-energy and $\Pi^{(0)\chi_1}_{\chi_2}(t,t')$ denotes the free propagator, $\Pi^{(0)\chi_1}_{\chi_2}(t,t') = \exp\left[-i(\varepsilon_{\chi_1} - \varepsilon_{\chi_2})(t-t')\right]$. The irreducible self-energy is given by a sum of all irreducible diagrams having at the ends the corresponding states. The Dyson equation for propagator $\Pi_{\chi_2\chi_2'}^{\chi_1\chi_1'}(t,t')$ can be written graphically as

$$\tag{4.8}$$

By multiplying Eq. (4.7) with $P_{\chi_2'}^{\chi_1'}(t')$ summing over χ_1', χ_2' and differentiating with respect to t, this equation can be transformed to the following [102]

$$\frac{d}{dt}P_{\chi_2}^{\chi_1}(t) + i(\varepsilon_{\chi_1} - \varepsilon_{\chi_2})P_{\chi_2}^{\chi_1}(t) = \sum_{\chi_1',\chi_2'}\int_{t_0}^t dt' \Sigma_{\chi_2\chi_2'}^{\chi_1\chi_1'}(t,t')P_{\chi_2'}^{\chi_1'}(t')\,. \tag{4.9}$$

The calculation proceeds with the determination of all the elements of the reduced density matrix, which can be found from the above time-dependent equation. However, in this analysis only the stationary properties of the system are considered, since the majority of experimental works has been carried out in this regime. In the stationary state, Eq. (4.9) becomes

$$0 = (\varepsilon_{\chi_1} - \varepsilon_{\chi_2})P_{\chi_2}^{\chi_1} + \sum_{\chi_1'\chi_2'}\Sigma_{\chi_2\chi_2'}^{\chi_1\chi_1'}P_{\chi_2'}^{\chi_1'}\,. \tag{4.10}$$

Because only spin conserving tunneling processes are taken into account and magnetic moments of the leads are collinear, all the spinor functions are represented in one reference frame. This results in vanishing of the off-diagonal elements of the reduced density matrix and consequently one can write $P_\chi^{\chi'} \equiv P_{\chi'}$ for density matrix elements and $\Sigma_{\chi_1\chi_1'}^{\chi\chi'} \equiv \Sigma_{\chi\chi'}$ for self-energies. Thus, the diagonal elements of the reduced density matrix can be determined from the following steady-state master equation

$$0 = \sum_\chi \Sigma_{\chi'\chi}P_\chi\,. \tag{4.11}$$

Now, each element P_χ has its clear physical meaning – it corresponds to the probability that the dot is in state $|\chi\rangle$. The electric current is given by [102, 129]

$$I = -\frac{ie}{2\hbar}\sum_{\chi\chi'}\Sigma_{\chi'\chi}^{\mathrm{I}}P_\chi\,, \tag{4.12}$$

where the self-energy $\Sigma_{\chi'\chi}^{\mathrm{I}}$ is modified as compared to $\Sigma_{\chi'\chi}$ to account for the number of electrons transferred through the barriers.

Using the diagrammatic language we perform a perturbative expansion of the reduced density matrix and self-energies in the coupling strength Γ

$$P_\chi = P_\chi^{(0)} + P_\chi^{(1)} + \dots , \tag{4.13}$$

$$\Sigma_{\chi'\chi} = \Sigma_{\chi'\chi}^{(1)} + \Sigma_{\chi'\chi}^{(2)} + \dots . \tag{4.14}$$

The expansion of the probabilities starts from the zeroth order, whereas the expansion of the self-energies proceeds from the first order in the dot-lead coupling strength Γ.

In these considerations we analyze the current up to the second order in Γ. This implies that we take into account the first-order and second-order self-energies. The respective self-energies $\Sigma_{\chi'\chi}^{(m)}$ and $\Sigma_{\chi'\chi}^{\mathrm{I}(m)}$ are determined by summing all irreducible diagrams of the m-th order, having at the ends the states χ' and χ, respectively. Consequently, the entire problem is reduced to the calculation of all the self-energies with the aid of the diagrammatic rules. The rules to calculate contributions coming from corresponding diagrams in energy space will be presented further on. Having determined the first- and second-order self-energies, it is straightforward to find the respective probabilities using the following stationary master equations [102]

$$0 = \sum_\chi \Sigma_{\chi'\chi}^{(1)} P_\chi^{(0)} , \tag{4.15}$$

$$0 = \sum_\chi \Sigma_{\chi'\chi}^{(2)} P_\chi^{(0)} + \Sigma_{\chi'\chi}^{(1)} P_\chi^{(1)} , \tag{4.16}$$

for the first and second orders, respectively. The probabilities are fully determined using the normalization

$$\sum_\chi P_\chi^{(m)} = \delta_{m,0} . \tag{4.17}$$

Systematic perturbation expansion of electric current with respect to the coupling strength Γ can be performed in a similar way as in the case of master equation [129]. The first-order and second-order contributions to the current can be calculated from the expressions [102, 129]

$$I^{(1)} = -\frac{ie}{2\hbar} \sum_{\chi\chi'} \Sigma_{\chi'\chi}^{\mathrm{I}(1)} P_\chi^{(0)} , \tag{4.18}$$

$$I^{(2)} = -\frac{ie}{2\hbar} \sum_{\chi\chi'} \Sigma_{\chi'\chi}^{\mathrm{I}(2)} P_\chi^{(0)} + \Sigma_{\chi'\chi}^{\mathrm{I}(1)} P_\chi^{(1)} . \tag{4.19}$$

Here, the coefficients $\Sigma_{\chi'\chi}^{\mathrm{I}(1)}$ and $\Sigma_{\chi'\chi}^{\mathrm{I}(2)}$ are the first- and second-order self-energies, respectively, in which one external vertex was substituted for an internal vertex representing the current operator $\hat{I}$.

The evaluation of probabilities $P_\chi^{(0)}$ and $P_\chi^{(1)}$ from Eqs. (4.15) and (4.16) has to be done carefully. As shown in the proceeding subsections, it is necessary to distinguish between the two cases in which sequential tunneling is either present or exponentially suppressed [105].

4.2.1 Perturbation Expansion in the Presence of Sequential Tunneling

In regime where the sequential tunneling is allowed, one can use the perturbation expansion presented in the previous subsection. In particular, one can determine the zeroth-order probabilities $P_\chi^{(0)}$ from Eq. (4.15) and, then, plug the result into Eq. (4.16) in order to evaluate the first-order corrections $P_\chi^{(1)}$. Having calculated the corresponding probabilities, one can use the result to calculate the current from Eqs. (4.18) and (4.19) in the first and second order, respectively.

4.2.2 Perturbation Expansion in the Coulomb Blockade Regime

The situation, however, becomes more complex for the range of parameters where the first-order processes are suppressed. In the Coulomb blockade regime, several of the first-order self-energies are exponentially small, as they are associated with energetically forbidden sequential tunneling rates. As a consequence, some factors in the first-order master equation, Eq. (4.15), are exponentially small. This is because either the state χ is classically forbidden, i.e., $P_\chi^{(0)}$ is exponentially suppressed, or the state χ is classically allowed but then the corresponding transition rates $\Sigma_{\chi'\chi}^{(1)}$ are exponentially small.

This is not a problem for the Coulomb blockade valleys with an even number of electrons, $k_BT, |eV| \ll \varepsilon, \varepsilon + U$ and $k_BT, |eV| \ll -\varepsilon, -\varepsilon - U$, since for this case there is only one classically-allowed dot state and from the first-order master equation one gets $P_\chi^{(0)} = \delta_{\chi,0}$ and $P_\chi^{(0)} = \delta_{\chi,\mathrm{d}}$, respectively. The situation is different for the Coulomb blockade valley with an odd number of electrons, $k_BT, |eV| \ll -\varepsilon, \varepsilon + U$, where both the states $\chi =\uparrow$ and $\chi =\downarrow$ are classically occupied. In this case, Eq. (4.15) simplifies to

$$
\begin{pmatrix}
\Sigma_{00}^{(1)} & 0 & 0 & 0 \\
\Sigma_{\uparrow 0}^{(1)} & 0 & 0 & \Sigma_{\uparrow \mathrm{d}}^{(1)} \\
\Sigma_{\downarrow 0}^{(1)} & 0 & 0 & \Sigma_{\downarrow \mathrm{d}}^{(1)} \\
0 & 0 & 0 & \Sigma_{\mathrm{dd}}^{(1)}
\end{pmatrix}
\begin{pmatrix}
P_0^{(0)} \\
P_\uparrow^{(0)} \\
P_\downarrow^{(0)} \\
P_\mathrm{d}^{(0)}
\end{pmatrix}
= 0 \, . \tag{4.20}
$$

From the above equation one obtains $P_0^{(0)} = P_\mathrm{d}^{(0)} = 0$, while the individual occupation probabilities $P_\uparrow^{(0)}$ and $P_\downarrow^{(0)}$ remain undetermined. Furthermore, the probabilities $P_\uparrow^{(1)}$ and $P_\downarrow^{(1)}$ do not appear in the second-order master equation,

Eq. (4.16), and the expression for the second-order current, Eq. (4.19), because they are multiplied with exponentially small self-energies $\Sigma_{\chi'\chi}^{(1)}$. As a consequence, one only needs to find the probabilities $P_0^{(1)}$, $P_\uparrow^{(0)}$, $P_\downarrow^{(0)}$, and $P_{\mathrm{d}}^{(1)}$. They are determined from the second-order master equation given by Eq. (4.16), which simplifies to

$$
\begin{pmatrix}
\Sigma_{00}^{(1)} & \Sigma_{0\uparrow}^{(2)} & \Sigma_{0\downarrow}^{(2)} & 0 \\
\Sigma_{\uparrow 0}^{(1)} & \Sigma_{\uparrow\uparrow}^{(2)} & \Sigma_{\uparrow\downarrow}^{(2)} & \Sigma_{\uparrow\mathrm{d}}^{(1)} \\
\Sigma_{\downarrow 0}^{(1)} & \Sigma_{\downarrow\uparrow}^{(2)} & \Sigma_{\downarrow\downarrow}^{(2)} & \Sigma_{\downarrow\mathrm{d}}^{(1)} \\
0 & \Sigma_{\mathrm{d}\uparrow}^{(2)} & \Sigma_{\mathrm{d}\downarrow}^{(2)} & \Sigma_{\mathrm{dd}}^{(1)}
\end{pmatrix}
\begin{pmatrix}
P_0^{(1)} \\
P_\uparrow^{(0)} \\
P_\downarrow^{(0)} \\
P_{\mathrm{d}}^{(1)}
\end{pmatrix} = 0\,,
\tag{4.21}
$$

together with normalization condition, Eq. (4.17), which is now given by $P_\uparrow^{(0)} + P_\downarrow^{(0)} = 1$. The current can be then calculated from the expression

$$
I = -\frac{ie}{2\hbar} \sum_\chi \Sigma_{\chi\uparrow}^{\mathrm{I}(2)} P_\uparrow^{(0)} + \Sigma_{\chi\downarrow}^{\mathrm{I}(2)} P_\downarrow^{(0)} + \Sigma_{\chi 0}^{\mathrm{I}(1)} P_0^{(1)} + \Sigma_{\chi\mathrm{d}}^{\mathrm{I}(1)} P_{\mathrm{d}}^{(1)}\,.
\tag{4.22}
$$

It is worth noting that the current in the Coulomb blockade regime can alternatively be calculated without the use of the real-time diagrammatic technique. Instead one can express the cotunneling rates using the second-order perturbation theory and then calculate the occupation probabilities from the appropriate master equation. This method is known as the Averin-Nazarov approach and will be described in section 4.3. The results obtained within the second-order perturbation theory are identical to the ones obtained using the diagrammatic language. Close to resonance, however, it is not sufficient to include the sequential and cotunneling processes, but also contributions associated with renormalization of level position, level splitting and tunnel-coupling strength. All these effect are automatically taken into account within the real-time diagrammatic technique in a systematic way.

4.2.3   Crossover Scheme

In previous subsections a proper perturbation expansion of the current up to the second order in Γ for both the case when sequential tunneling is allowed or suppressed was formulated. However, when calculating transport characteristics as a function of various parameters, such as the gate or transport voltage, one has to switch from one scheme to the other around the threshold of sequential tunneling. In order to cross smoothly from one scheme to the other one a crossover scheme can be used. This scheme consists of solving the master equation with first-order and second-order self-energies, without expanding the probabilities

$$
0 \;=\; \sum_\chi \left[\Sigma_{\chi'\chi}^{(1)} + \Sigma_{\chi'\chi}^{(2)} \right] P_\chi\,.
\tag{4.23}
$$

Then the probabilities can be used to calculate the current from the following expression

$$I = -\frac{ie}{2\hbar} \sum_{\chi\chi'} \left[\Sigma_{\chi'\chi}^{\mathrm{I}(1)} + \Sigma_{\chi'\chi}^{\mathrm{I}(2)} \right] P_\chi. \tag{4.24}$$

Up to the second order in the dot-lead coupling strength Γ, this result for the electric current is identical to the one obtained with the aid of the accurate perturbation schemes described previously. Deviations are of third and higher order, which are however always small for the chosen parameters.

4.2.4   Diagrammatic Rules in Energy Space

In this section the general rules in energy space for calculating contributions of various diagrams are presented [102, 127]. Contribution of a particular diagram to the self-energy $\Sigma_{\chi'\chi}$ can be found following the general rules in energy space:

1. Draw all topologically different diagrams with fixed time ordering and position of vertices. Connect the vertices by tunneling lines. Assign the energies of respective quantum dot states to the forward and backward propagators. To each tunneling line assign a frequency ω, the spin of tunneling electron and label of the junction.

2. Tunneling lines acquire arrows indicating whether an electron leaves or enters the dot. For tunneling lines going forward with respect to the Keldysh contour assign a factor $\gamma_r^{-\sigma}(\omega)$, whereas for tunneling lines going backward assign $\gamma_r^{+\sigma}(\omega)$.

3. For each time interval on the real axis limited by two adjacent vertices draw a vertical line inside the interval and assign a resolvent $1/(\Delta E + i0^+)$, with ΔE being the difference of all energies crossing the vertical line from right side minus all energies crossing the vertical line from left side.

4. Each diagram gets a prefactor $(-1)^{b+c}$, with b being the number of vertices lying on the backward propagator and c denoting the number of crossings of the tunneling lines.

5. Each internal vertex represents a matrix element $\langle\chi|d_\sigma^\dagger|\chi'\rangle$ or $\langle\chi|d_\sigma|\chi'\rangle$. Consequently, a minus sign may appear due to these matrix elements. This is because $|\mathrm{d}\rangle = \mathrm{d}_\sigma^\dagger|\bar\sigma\rangle = -\mathrm{d}_{\bar\sigma}^\dagger|\sigma\rangle$ (depending on the definition of state $|\mathrm{d}\rangle$), where $\sigma = \uparrow$ or $\sigma = \downarrow$. To account for this factor, multiply each diagram by $(-1)^m$, where m is the number of vertices connecting the spin-σ state with doubly occupied state.

6. Integrate over all frequencies and sum up over the reservoirs.

The parameters $\gamma_r^{\pm\sigma}(\omega)$ are defined as

$$\gamma_r^{+\sigma}(\omega) = \frac{\Gamma_r^\sigma}{2\pi} f(\omega - \mu_r), \qquad (4.25)$$

$$\gamma_r^{-\sigma}(\omega) = \frac{\Gamma_r^\sigma}{2\pi}[1 - f(\omega - \mu_r)], \qquad (4.26)$$

with $f(x)$ being the Fermi-Dirac distribution function, $f(x) = 1/[\exp(x/k_\mathrm{B}T) + 1]$, and μ_r representing the electrochemical potential of lead r.

To find electric current flowing through the system, one has to determine the self-energies Σ^I, see Eqs. (4.18) or (4.19). This can be done by realizing that each term of the expansion of the current operator $\hat{I} = (\hat{I}_\mathrm{R} - \hat{I}_\mathrm{L})/2$, where $\hat{I}_r$ is the current operator for electrons tunneling to the lead r, is equal to the corresponding expansion term of the reduced density matrix multiplied by a factor of $e/\hbar$. The only difference is that now for each external vertex lying on the upper (lower) branch of the Keldysh contour, corresponding to tunneling of an electron into the left (right) or out of the right (left) lead, we have a multiplicative factor $+1/2$, whereas for each external vertex on the upper (lower) branch of the contour, describing tunneling of an electron into the right (left) or out of the left (right) lead, there is a factor of -1/2.

The explicit expressions for the first-order self-energies $\Sigma^{(1)}$ and $\Sigma^{\mathrm{I}(1)}$ are listed in Appendix A.1. Whereas the second-order self-energies $\Sigma^{(2)}$ and $\Sigma^{\mathrm{I}(2)}$ are presented in Appendix A.2. An exemplary calculation of one of the second-order self-energies is also described therein.

4.3   Averin-Nazarov Approach

In this section an approach developed by Averin and Nazarov [30] is presented. Within this approach one can analyze the second-order transport in the case when the system is in a deep Coulomb blockade. It consists in calculating the cotunneling rates using the second-order perturbation theory, whereas the respective occupation probabilities are determined from the appropriate master equation. The cotunneling rate for transition from lead r to lead r' is given by [101]

$$\gamma_{rr'} = \frac{2\pi}{\hbar} \left| \sum_\nu \frac{\langle \Phi_r | H_\mathrm{T} | \Phi_\nu \rangle \langle \Phi_\nu | H_\mathrm{T} | \Phi_{r'} \rangle}{\varepsilon_i - \varepsilon_\nu} \right|^2 \delta(\varepsilon_i - \varepsilon_f), \qquad (4.27)$$

where ε_i and ε_f denote the energies of the initial and final states, $|\Phi_r\rangle$ is the state with an electron in the lead r, whereas $|\Phi_\nu\rangle$ is a virtual state of the system with ε_ν denoting the corresponding energy. Between cotunneling processes one can distinguish the *single-barrier* ($r = r'$) and *double-barrier* ($r \neq r'$) cotunneling processes. Furthermore, there are also cotunneling processes that leave unchanged magnetic state of the dot (*non-spin-flip* processes) and the processes
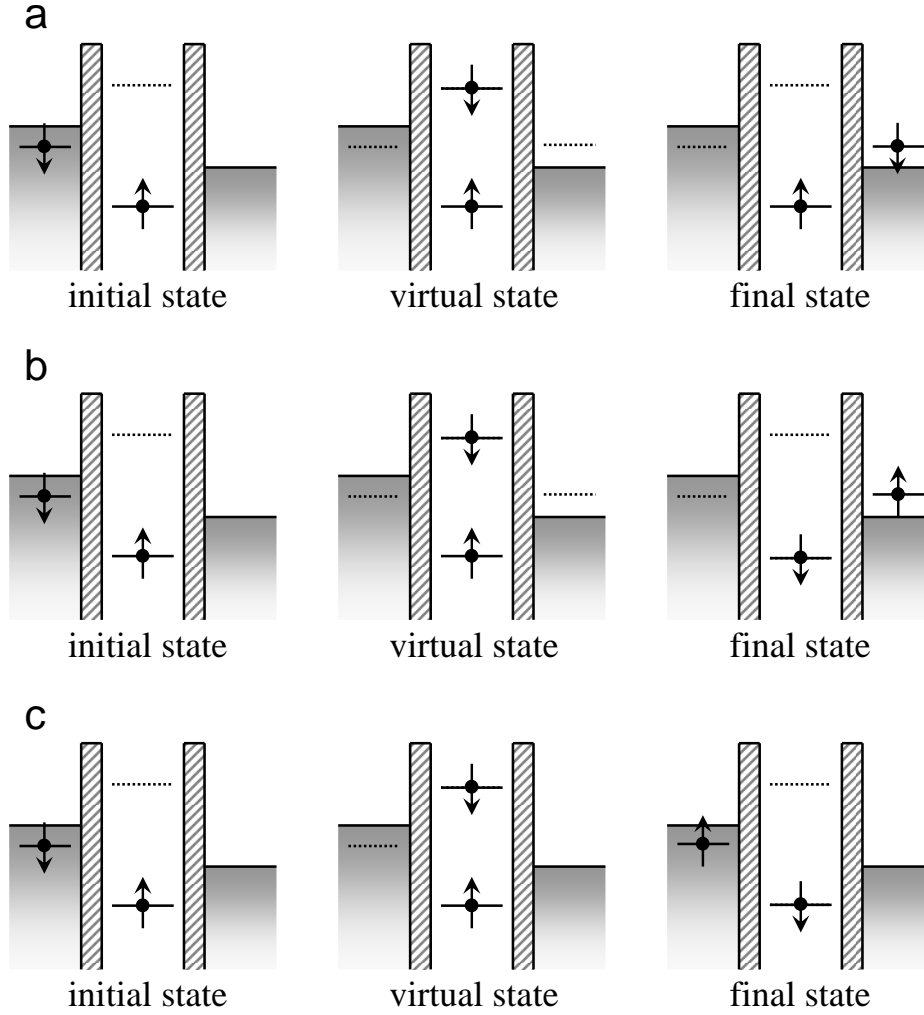
Figure 4.3: A sketch illustrating different types of cotunneling processes: (a) double-barrier non-spin-flip cotunneling, (b) double-barrier spin-flip cotunneling and (c) single-barrier spin-flip cotunneling. The process shown in (c) is possible only for $k_BT > 0$.

which reverse spin of the dot (*spin-flip* processes). The former processes are elastic and coherent, whereas the latter ones are generally inelastic and lead to decoherence. The various cotunneling processes are illustrated schematically in Fig. 4.3. Part (a) shows a double-barrier non-spin-flip cotunneling process, part (b) presents a double-barrier spin-flip cotunneling event, whereas part (c) is an example of a single-barrier spin-flip cotunneling process. The spin-flip cotunneling can take place *via* two intermediate virtual states, in which the dot is either empty or doubly occupied. For the sake of clarity, in Fig. 4.3b,c we show only one of the two possible virtual states, namely, the one in which the dot is in state

$|\chi = \mathrm{d}\rangle$.

Unlike the double-barrier cotunneling processes, the single-barrier ones do not contribute directly to electric current. However, they may affect the occupation probabilities, and this way also the current flowing through the system.

In the case of empty or doubly occupied dot (Coulomb blockade valleys with even number of electrons) the occupation probabilities are fixed, respectively, either $P_0 = 1$ or $P_{\mathrm{d}} = 1$. The situation is changed for singly occupied dot (Coulomb blockade valleys with odd number of electrons). Although in this case the probability that the dot is occupied by a single electron is equal to unity, it is necessary to determine the occupation probabilities for having spin-up or spin-down electron on the dot. They can be calculated from the following master equation

$$0 = \sum_{r,r'=\mathrm{L,R}} \left(-\gamma_{rr',\sigma \Rightarrow \bar{\sigma}} P_\sigma + \gamma_{rr',\bar{\sigma} \Rightarrow \sigma} P_{\bar{\sigma}} \right) , \qquad (4.28)$$

together with the normalization condition

$$P_\sigma + P_{\bar{\sigma}} = 1 , \qquad (4.29)$$

where $\gamma_{rr',\sigma \Rightarrow \sigma'}$ denotes the cotunneling rate for transition from lead r to lead r' with a change of the dot spin from σ to σ'. If $\sigma = \sigma'$ the process is a non-spin-flip one, whereas for $\sigma \neq \sigma'$ the process is a spin-flip one. The explicit expressions for the cotunneling rates are given in Appendix B. Having calculated the corresponding probabilities from Eq. (4.28), one can calculate electric current using the formula

$$I = -e \sum_{\sigma,\sigma'=\uparrow,\downarrow} \left[\gamma_{\mathrm{LR},\sigma \Rightarrow \sigma'} - \gamma_{\mathrm{RL},\sigma \Rightarrow \sigma'} \right] P_\sigma . \qquad (4.30)$$

This method was first proposed for single-electron transistors [30] and then extended into the case of quantum dots [101]. It is worth noting that in deep Coulomb blockade where sequential processes are suppressed, within the approach described above, one gets results identical to the ones obtained within the perturbation scheme presented in subsection 4.2.2.

4.4　Numerical Results on Transport through Quantum Dots

In the following, we analyze transport through quantum dots in both the linear and nonlinear response regimes [105]. Therefore, it is important to distinguish between different transport regimes that will be considered. The various transport regimes are sketched in Fig. 4.4 and labelled by corresponding letters.

First of all, one can see that by changing the position of the dot level (by the gate voltage) or applying the bias voltage, one can cross over from one regime
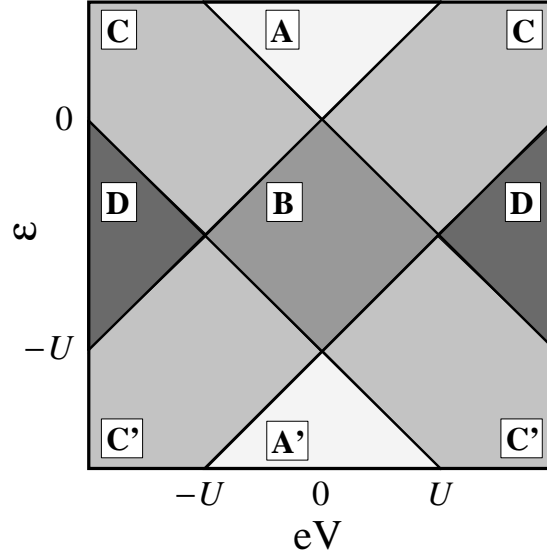
Figure 4.4:   A sketch illustrating different transport regimes. The respective regimes are separated by solid lines and labelled correspondingly.

to another. The three diamonds around zero bias correspond to regime where sequential tunneling is exponentially suppressed and current flows due to cotunneling. In these regimes the charge state of the dot is fixed to zero electrons in regime A, one electron in regime B, and two electrons in regime A'. The first-order tunneling processes are possible once the bias voltage is increased above the threshold voltage, allowing for finite occupation of two adjacent charge states (zero and one for regime C, and one and two for regime C'). In regime D all four dot states $\chi = 0, \uparrow, \downarrow, \mathrm{d}$ are possible. By performing a particle-hole transformation, the behavior in regime A' and C' can be mapped to that in regime A and C, respectively.

4.4.1   Case of Nonmagnetic Leads

Before the description of numerical results of the first-order and second-order transport through a quantum dot coupled to ferromagnetic leads, let us discuss briefly the case of a dot coupled to nonmagnetic leads ($p_{\mathrm{L}} = p_{\mathrm{R}} = 0$). At equilibrium, the dot can be occupied by zero electrons when $\varepsilon \gg 0$ (regime A), one electron for $-U \ll \varepsilon \ll 0$ (regime B), and two electrons when $\varepsilon \ll -U$ (regime A'). When $\varepsilon \approx 0$ or $\varepsilon \approx -U$, the dot is in a mixed valance state. The occupancy can be changed by applying gate voltage to the dot.

Figure 4.5 shows the linear conductance calculated in the first (dashed line) and second (dotted line) orders as well as the total conductance (solid line) defined as the sum of the first- and second-order contributions. The conductance
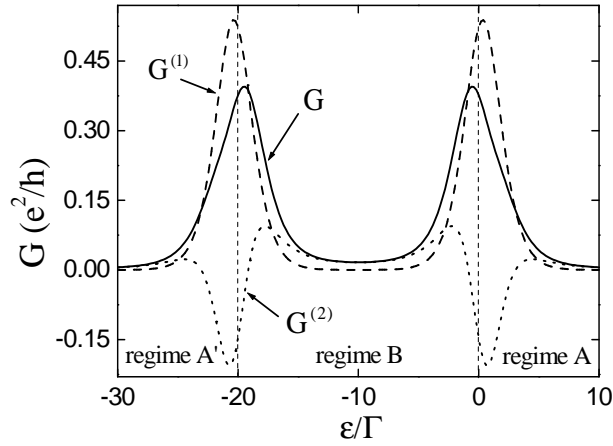
Figure 4.5: Linear conductance as a function of the level position. The dashed line corresponds to the first-order contribution $G^{(1)}$, the dotted line presents the second-order conductance $G^{(2)}$ and the solid line shows the sum $G^{(1)} + G^{(2)}$. The different transport regimes are also specified. The parameters are: $k_{\mathrm{B}}T = \Gamma$, $U = 20\Gamma$, and $p = 0$. The figure was generated using the scheme for the perturbation expansion in the presence of sequential tunneling.

is shown there as a function of the position of the dot level energy. Since this position can be changed by an externally applied gate voltage, Fig. 4.5 can be considered effectively as a gate voltage dependence of the linear conductance.

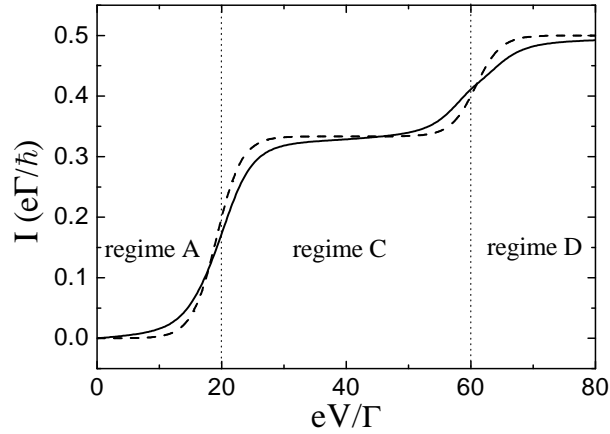
Figure 4.6: The current as a function of the bias voltage. The dashed line presents the first-order contribution, whereas the solid line shows the first- and second-order current. The parameters are: $k_{\mathrm{B}}T = \Gamma$, $\varepsilon = 10\Gamma$, $U = 20\Gamma$, and $p = 0$. The figure was generated using the scheme for the perturbation expansion in the presence of sequential tunneling.

When the energy of the dot level crosses the Fermi level of electrodes, there is
a resonance peak in the linear conductance. Another resonance appears when
$\varepsilon + U$ crosses the Fermi level. The resonance peaks acquire a certain width as a
result of thermal fluctuations and also as a result of the level broadening. It is
interesting to note, that the second-order contribution becomes negative at res-
onances, which indicates that the second-order processes renormalize first-order
(sequential) contribution. Except for resonances, the dot is either in the empty
(regime A) or doubly occupied (regime A') state, or in the Coulomb blockade
regime (regime B). In all these three cases the cotunneling contribution to elec-
tric current becomes dominant. It is also worth noting, that the second-order
processes lead to renormalization of the dot level energy[2].

The first-order as well as first- and second-order currents as a function of the
bias voltage are shown in Fig. 4.6. The parameters correspond to the situation
when the dot level lies above the Fermi energy of the leads. In the Coulomb
blockade regime (regime A), the sequential tunneling is suppressed and the cur-
rent flows due to cotunneling. Furthermore, the second-order processes lead to
smearing of the Coulomb steps, as can be seen in Fig. 4.6.

4.4.2   Case of Ferromagnetic Leads

When the quantum dot is coupled to ferromagnetic leads, some novel phenomena
originating from ferromagnetism of the leads can arise. In particular, these phe-
nomena result from spin dependency of the coupling between the dot and ferro-
magnetic leads. In the following, it is assumed that spin-up (spin-down) electrons
in the parallel configuration correspond to the majority (minority) electrons of
the leads. In the antiparallel configuration, on the other hand, the magnetic
moment of the right electrode is reversed (see Fig. 4.1), and spin-up (spin-down)
electrons correspond to minority (majority) electrons in the right lead.

As a consequence of spin-dependent densities of states in the leads, the dot-
lead coupling also becomes dependent on spin. In the parallel configuration
and for symmetric junctions, the coupling of the spin-up level to electrodes is
proportional to $(1 + p)$, whereas coupling of the spin-down level is proportional
to $(1 - p)$. One may then expect an effective splitting of the dot level due to
interaction with ferromagnetic leads [93, 113]. Figure 4.7 shows the zeroth-order
and first-order probabilities to find the dot in the states $| \uparrow \rangle$ and $| \downarrow \rangle$ in the linear
response regime. The probabilities are shown as a function of the level position.

In equilibrium, the lowest-order probabilities are simply given by the Boltz-
mann factors, $P_\chi^{(0)} = \exp(-\beta \varepsilon_\chi)/Z$, with Z denoting the partition function and ε_χ
being the energy of state $|\chi\rangle$. When the isolated dot is nonmagnetic ($\varepsilon_\uparrow = \varepsilon_\downarrow = \varepsilon$),
the zeroth-order occupation probabilities for spin-up and spin-down energy levels

---

[2]For a detailed description of second-order transport in the case of quantum dots coupled
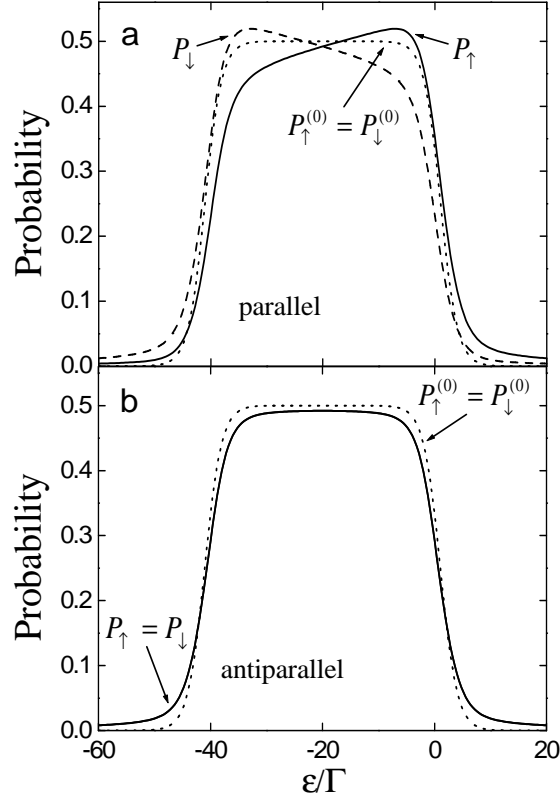to nonmagnetic leads see Ref. [102].

Figure 4.7: The occupation probabilities of the spin-up and spin-down dot levels as a function of the level position in the parallel (a) and antiparallel (b) configurations. The zeroth-order occupation probabilities for the spin-up and spin-down levels are equal in both magnetic configurations, and are represented by the dotted lines. The total occupation probability of the spin-up (spin-down) level is presented by the solid (dashed) line. In the antiparallel configuration, the dashed and solid lines coincide. The parameters are: $k_{\mathrm{B}}T = 1.5\Gamma$, $U = 40\Gamma$, and $p = 0.5$. The figure was generated using the scheme for the perturbation expansion in the presence of sequential tunneling.

are equal, $P_\uparrow^{(0)} = P_\downarrow^{(0)}$, as shown in Fig. 4.7. However, the corrections $P_\chi^{(1)}$ due to the second-order processes give rise to a finite splitting of the dot level, as can be concluded from Fig. 4.7a. An effective exchange field exerted by ferromagnetic electrodes on the dot gives rise to a difference in occupations of the spin-up and spin-down levels[3]. However, the difference in energy is relatively small compared to the thermal energy $k_{\mathrm{B}}T$, therefore the splitting may be hardly detectable in conductance measurements.

Contrarily, in the antiparallel configuration the spin-up and spin-down lev-

---

[3]An overview about the various effects of exchange field can be found in Ref. [130].
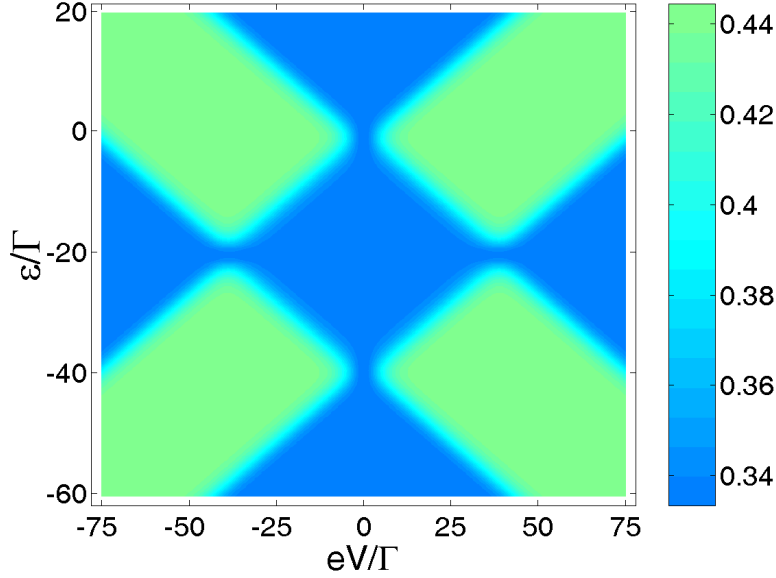
Figure 4.8: The first-order tunnel magnetoresistance as a function of the bias and gate voltages. The parameters are: $k_{\mathrm{B}}T = 1.5\Gamma$, $U = 40\Gamma$, and $p = 0.5$.

els are equally coupled to the leads, with the coupling strength independent of spin polarization p (provided there is no asymmetry between the left and right junctions in the parallel configuration). If this is the case, the probability of having a spin-up electron is equal to the probability that the dot is occupied by a spin-down electron, $P_\uparrow = P_\downarrow$. This situation is displayed in Fig. 4.7b.

In the case of ferromagnetic systems, transport characteristics usually depend on the relative orientation of the leads' magnetic moments, and the resistance generally increases when magnetic alignment switches from parallel to antiparallel. The relative change in the resistance is described phenomenologically by tunnel magnetoresistance given by Eq. (1.3). In the following part, we present and discuss the behavior of the TMR effect in different transport regimes.

Figure 4.8 shows tunnel magnetoresistance calculated in the first order of the dot-lead coupling strength Γ as a function of bias and gate voltages. It can be seen that TMR generally takes two values, depending on transport regime. For regimes A (and A'), B and D, the TMR value is

$$\mathrm{TMR}_{\mathrm{seq}}^{\mathrm{A,B,D}} = \frac{p^2}{1 - p^2} = \frac{1}{2}\mathrm{TMR}^{\mathrm{Jull}}, \qquad (4.31)$$

while for regime C (and C') it is

$$\mathrm{TMR}_{\mathrm{seq}}^{\mathrm{C}} = \frac{4p^2}{3(1 - p^2)} = \frac{2}{3}\mathrm{TMR}^{\mathrm{Jull}}. \qquad (4.32)$$
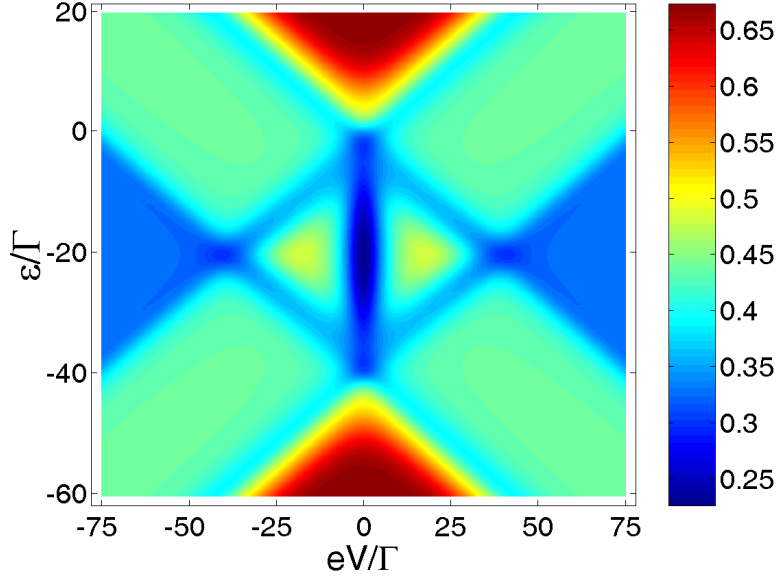
Figure 4.9: The first and second-order tunnel magnetoresistance as a function of bias and gate voltages. The parameters are the same as in Fig. 4.8. The figure was generated using the crossover scheme.

These results can be understood in the following way. For regions A and B the first-order linear conductance in the parallel and antiparallel configurations can be expressed as

$$G_\mathrm{P}^{(1)} \sim \Gamma/2 \quad \text{and} \quad G_\mathrm{AP}^{(1)} \sim \Gamma(1-p^2)/2 \;, \tag{4.33}$$

which gives the TMR equal to $\mathrm{TMR}_\mathrm{seq}^\mathrm{A,B} = p^2(1-p^2)$.

To understand the behavior of TMR in regions C and D let us consider the case at zero temperature and assume that electrons tunnel only from the left to right sides. In region C there are three dot states taking part in transport, those are $\chi = 0, \uparrow, \downarrow$ (because of particle-hole symmetry results are applicable to regime C'). For this case one finds the first-order currents in the parallel and antiparallel configurations to be

$$I_\mathrm{P}^{(1)} \sim \Gamma/3 \quad \text{and} \quad I_\mathrm{AP}^{(1)} \sim \Gamma(1-p^2)/(3+p^2) \;, \tag{4.34}$$

which, after plugging to the formula for TMR, gives $\mathrm{TMR}_\mathrm{seq}^\mathrm{C} = 4p^2/3(1-p^2)$. By performing a similar analysis for region D, one gets, $I_\mathrm{P}^{(1)} \sim \Gamma/2$ and $I_\mathrm{AP}^{(1)} \sim \Gamma(1-p^2)/2$, for the corresponding currents. Consequently, the TMR is found to be $\mathrm{TMR}_\mathrm{seq}^\mathrm{D} = p^2/(1-p^2)$.

One can note that the sequential tunneling TMR is always smaller than the Jullière's value of TMR, see Eq. (1.5). This is because the corresponding first-order transition rates involve the spin-dependent density of states of only one

lead, as can be seen from the expressions for first-order self-energies given in appendix A.1. As it was already pointed in previous chapters, the TMR does not occur in systems of type FM/NM/FM, unless a finite spin accumulation on the middle electrode is taken into account. In the case of quantum dots, it is thus the spin accumulation on the dot that mediates the information about the relative magnetic orientation of the leads. This indirect mechanism is, however, always less effective than a direct coupling of the two leads. Consequently, the value of the first-order TMR is always smaller than the Jullière's TMR.

Let us now include the second-order contribution and discuss the changes in the TMR effect due to cotunneling. This situation is displayed in Fig. 4.9. The sequential tunneling dominates transport above threshold voltage, i.e., in regimes C and D. As a consequence, the total TMR is only slightly modified as compared to the first-order TMR. In regimes A and B, however, the first-order tunneling processes are exponentially suppressed and the current flows due to second-order tunneling processes. As can be seen in Fig. 4.9, in these regimes, cotunneling has the largest impact on tunnel magnetoresistance. Furthermore, TMR exhibits distinctively different behavior in regimes A and B. In the following, the TMR effect in different transport regimes is presented and discussed in more details.

The first and second-order linear conductance as well as the resulting TMR effect as a function of the level position (gate voltage) are displayed in Fig. 4.10. By changing the position of the dot level, one crosses over from regime A through regime B to regime A'. First of all, it can be seen that the total conductance for parallel alignment is larger than that in the antiparallel configuration, as shown in Fig. 4.10a. This difference in turn leads to a nonzero TMR effect shown in Fig. 4.10b. For comparison, the Jullière's value of TMR is also displayed in the figure. The first-order contribution to TMR (denoted as TMR$^{(1)}$) is constant as a function of the gate voltage and equal exactly to a half of the Jullière's value. First of all, one can see that the inclusion of second-order processes modifies the TMR substantially. Unlike the first-order term, the total TMR (first-order plus second-order contributions) does depend on the level position. The interesting and new feature of TMR shown in Fig. 4.10b is a strong parity effect. The TMR reaches maximum when there is an even number of electrons on the dot (zero for regime A or two for regime A'), and has minimum for an odd (one in regime B) number of electrons. A universal feature is that for even electron number the value of TMR exactly coincides with the Jullière's value. This fact suggests that for even number of electrons, the system behaves like a single ferromagnetic tunnel junction. Such a situation can take place when tunneling processes are coherent. Consider, for example, the case of empty dot. The only second-order processes that contribute to conductance are the non-spin-flip cotunneling processes, in which the electron spin is conserved, see Fig. 4.3a. Such processes are fully coherent. The corresponding cotunneling rates are proportional to the product of the density of states of the left and right leads, thus, one can express the
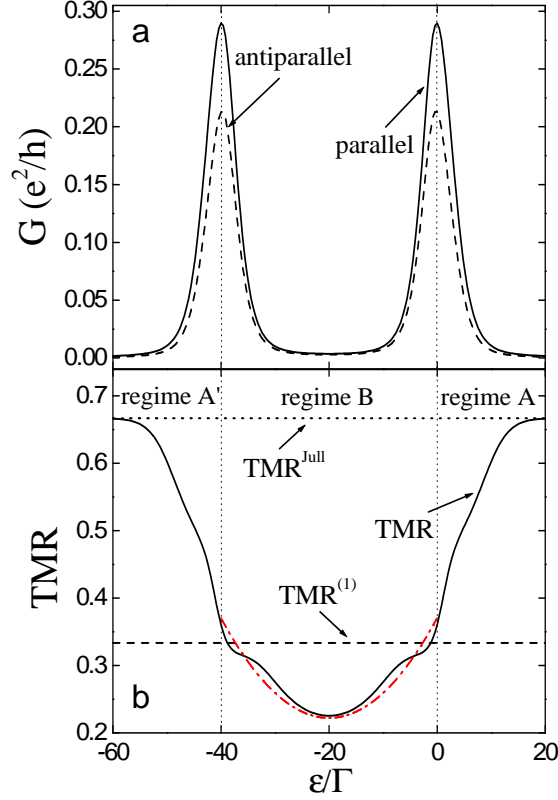
Figure 4.10: The total linear conductance (a) in the parallel (solid line) and antiparallel (dashed line) configuration and the resulting tunnel magnetoresistance [solid line in (b)] as a function of the level position. The dashed line in part (b) represents the first-order tunnel magnetoresistance, whereas the dotted line corresponds to the Jullière's value. The dotted-dashed curve presents the TMR calculated using Eq. (4.37). The parameters are $k_{\mathrm{B}}T = 1.5\Gamma$, $U = 40\Gamma$, and $p = 0.5$. The figure was generated using the scheme for the perturbation expansion in the presence of sequential tunneling.

second-order linear conductance as

$$G_{\mathrm{P}}^{(2)} \sim \frac{\Gamma^2}{2}(1 + p^2) \quad \text{and} \quad G_{\mathrm{AP}}^{(2)} \sim \frac{\Gamma^2}{2}(1 - p^2) \,, \qquad (4.35)$$

for the parallel and antiparallel configuration, respectively. As a consequence, the TMR is that of a single ferromagnetic tunnel junction

$$\mathrm{TMR}^{\mathrm{A}} = \frac{2p^2}{1 - p^2} = \mathrm{TMR}^{\mathrm{Jull}} \,, \qquad (4.36)$$

i.e., twice as large as the first-order TMR. Because of the particle-hole symmetry, the same result can be obtained for regime A'.

While the dot occupied by an even number of electrons allows only non-spin-flip (coherent) cotunneling processes, the situation becomes more complex for an odd number of electrons on the dot. Apart from the non-spin-flip processes described above, there are also spin-flip cotunneling processes that change spin of the dot, see Fig. 4.3b and c. Such second-order processes give rise to spin relaxation on the dot. Moreover, such processes are incoherent. This effectively leads to reduction of TMR for regime B. In other words, the suppression of TMR in regime B can be understood by realizing the fact that for a singly-occupied dot both spin-flip and non-spin-flip cotunneling processes are possible, in contrast to regime A where only non-spin-flip cotunneling occurs. Thus, spin-flip cotunneling has a tendency to reduce the TMR, which is minimal for $\varepsilon = -U/2$, see Fig. 4.10b. The dependence of TMR on the position of the energy level in regime B reflects the relative relation of the spin-flip to non-spin-flip cotunneling processes. The corresponding cotunneling rates are given in appendix B.1, see Eqs. (B.2), (B.11) and (B.12). Thus, for the gate voltage dependence of the ratio of spin-flip to non-spin-flip cotunneling, one finds $[-1/\varepsilon + 1/(\varepsilon + U)]^2/[1/\varepsilon^2 + 1/(\varepsilon + U)^2] = 2/[1 + (1 + 2\varepsilon/U)^2]$, which can be obtained from the expressions for cotunneling rates by setting $\omega = 0$. It can bee seen that the ratio is maximal for $\varepsilon = -U/2$, thus leading to a minimum in TMR. As illustrated in Fig. 4.10b, the gate voltage dependence of the linear response TMR around the center is parabolic. When considering the case of deep Coulomb blockade regime ($k_\mathrm{B}T, \Gamma \ll |\varepsilon|, \varepsilon + U$), taking into account only the lowest-order corrections in the ratio x/y with $x = |eV|, k_BT$, $y = |\varepsilon|, \varepsilon + U$, and, further, expanding the TMR up to quadratic order around $\varepsilon = -U/2$, one can obtain an approximate analytic expression for the TMR

$$\mathrm{TMR}^\mathrm{B} = \frac{p^2}{1 - p^2}\left[\frac{2}{3} + \frac{4}{9}\left(1 + \frac{2\varepsilon}{U}\right)^2\right]. \tag{4.37}$$

From the above expression one finds that for $\varepsilon = -U/2$, which corresponds to minimal value of TMR, the tunnel magnetoresistance is

$$\mathrm{TMR}^\mathrm{B}_\mathrm{min} = \frac{2p^2}{3(1 - p^2)} = \frac{1}{3}\mathrm{TMR}^\mathrm{Jull}, \tag{4.38}$$

For comparison, in Fig. 4.10b we also plotted the analytic expression given by Eq. (4.37). As can be seen in the figure, this formula approximates the numerical data relatively accurately.

Figure. 4.11 illustrates the current flowing through the system in the parallel and antiparallel configurations as well as the resulting TMR as a function of level position for the nonlinear response regime. The dashed line in Fig. 4.11b presents the first-order TMR plotted for reference. When changing the gate voltage, one crosses over from regime A' through regime C' to regime B and then further on through regime C to regime A. As shown in the figure, the second-order processes modify the TMR mainly in regimes A and B, whereas in regime C, where the
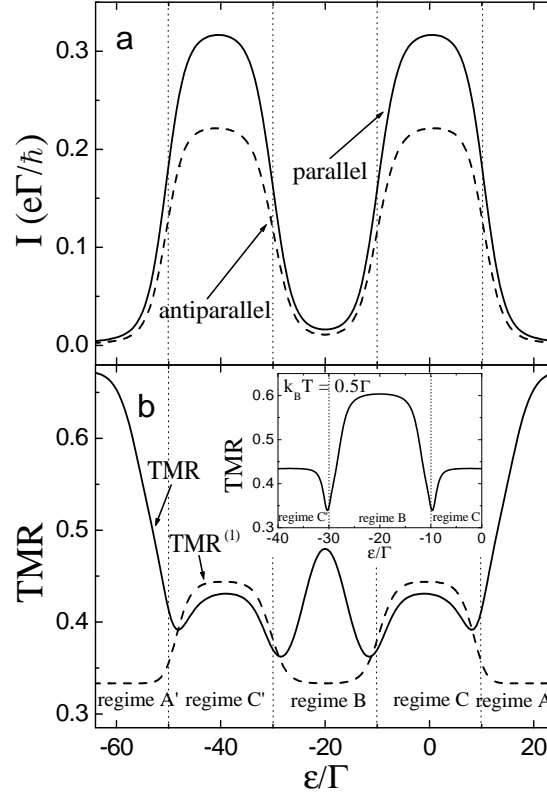
Figure 4.11:   The total currents (a) in the parallel (solid line) and antiparallel (dashed line) magnetic configurations as a function of level position for $eV = 20\Gamma$. Part (b) shows the first-order contribution to the TMR (dashed line) and the total TMR (solid line). The inset in part (b) shows the total TMR at lower temperature, $k_{\mathrm{B}}T = 0.5\Gamma$. The other parameters are the same as in Fig. 4.10. The figure was generated using the crossover scheme.

sequential tunneling dominates, the total TMR is only slightly modified. Furthermore, it can be seen that the behavior of TMR in regime B differs significantly from that in linear response shown in Fig. 4.10b. Instead of a minimum, TMR has a local maximum for $\varepsilon = -U/2$, as displayed in Fig. 4.11b. When lowering the temperature, this maximum develops into a pronounced plateau, see the inset of Fig. 4.11b. The height of this plateau is given by the Jullière's value and the width is determined by the region where first-order contributions are negligible. The reason for this increased TMR is nonequilibrium spin accumulation, which appears in the nonlinear response regime. Spin accumulation, in turn, decreases the role of spin-flip cotunneling and, as a consequence, non-spin-flip cotunneling dominates, leading to the Jullière's value of the total TMR. In the linear response, on the contrary, single-barrier spin-flip cotunneling processes become important. These processes do not contribute to transport but reduce the spin accumulation
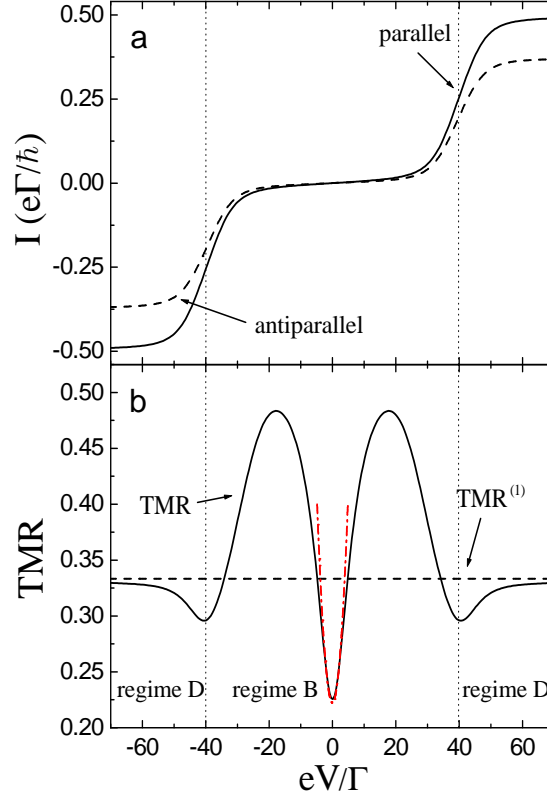
Figure 4.12: The total current (a) in the parallel (solid line) and antiparallel (dashed line) magnetic configurations as a function of the bias voltage. Part (b) shows the first-order contribution to the TMR (dashed line) and the total TMR (solid line). The dotted-dashed curve presents the TMR calculated using Eq. (4.40). The parameters are: $k_B T = 1.5\Gamma$, $\varepsilon = -20\Gamma$, $U = 40\Gamma$, and $p = 0.5$. The figure was generated using the crossover scheme.

and, consequently, the TMR effect. When approaching the threshold for sequential tunneling, the first-order processes dominate transport and TMR drops from Jullière's value to the first-order TMR, as can be seen in Fig. 4.11b. For regime A (A') the TMR effect reaches the Jullière's value, similarly as in the case shown in Fig. 4.10b.

Electric current flowing through the system in the nonlinear response regime is shown in Fig. 4.12a for both magnetic configurations and for symmetric Anderson model ($\varepsilon = -U/2$). The resulting TMR is also shown there, see Fig. 4.12b. A finite contribution due to the second-order tunneling processes leads to a nonzero current in the Coulomb blockade regime. Furthermore, the cotunneling processes make the Coulomb steps smoother. The sequential TMR is shown by a dashed line in Fig. 4.12b. It can be seen that sequential TMR is constant as a function of the bias voltage. However, this is not a universal behavior but occurs only for

symmetric Anderson model. Generally, first-order TMR depends on the applied bias voltage, as illustrated in Fig 4.8. The second-order processes lead to a strong and nontrivial dependence of the total TMR on the bias voltage. For large values of the transport voltage (regime D), the first-order tunneling processes dominate, and therefore the total TMR is only slightly modified as compared to that in the sequential transport regime. However, for voltages below the threshold voltage (regime B), the cotunneling processes have to be included. These processes lead to a strong bias dependence of the TMR effect in the Coulomb blockade regime, and to a deep minimum of TMR in the zero-bias limit. This is an interesting and qualitatively new result. In the case of metallic islands, cotunneling processes usually lead to an enhancement of the TMR effect in the Coulomb blockade regime [33]. Here, we have the opposite situation, i.e., suppression of the effect. At low bias voltage, $|eV| \ll k_B T$, the single-barrier spin-flip processes reduce the TMR. This is however no longer the case for nonlinear response regime, $|eV| \gg k_B T$, where the spin accumulation diminishes the amount of spin-flip processes and the TMR increases. Consequently, the TMR effect in regime B increases with rising the bias voltage within the limits

$$\frac{1}{3}\mathrm{TMR}^{\mathrm{Jull}} \leq \mathrm{TMR}^{\mathrm{B}} \leq \mathrm{TMR}^{\mathrm{Jull}} \,. \tag{4.39}$$

The minimal value is reached at $V = 0$ and $\varepsilon = -U/2$, whereas the maximal value is approached for bias voltages large as compared to thermal energy but still far away from the onset of sequential tunneling. In order to determine an approximate analytic expression for the TMR around the minimum, we consider the symmetric Anderson model, $\varepsilon = -U/2$, expand the TMR up to quadratic order in $|eV|/k_B T$ and take the limit $|\varepsilon| \gg k_B T$. Then, we get

$$\mathrm{TMR}^{\mathrm{B}} = \frac{p^2}{1-p^2}\left[\frac{2}{3} + \frac{(3-p^2)(eV)^2}{54(k_B T)^2}\right] \,, \tag{4.40}$$

which compares well with the full numerical result, as can be seen in Fig. 4.12b. If the bias voltage increases further, the first-order processes become dominant and deep in regime D the TMR approaches one half of the Jullière's TMR, as shown in Fig. 4.12b.

Another interesting feature can be seen at the threshold voltage for sequential tunneling. This value of the bias voltage corresponds to the intersection point of regimes B, C and D. At this bias voltage, the first-order processes become dominant, however, the effect of second-order processes on TMR can still be observable. The corrections due to cotunneling lead to a local minimum of the TMR effect, as shown in Fig. 4.12b. When assuming $|\varepsilon| \gg k_B T$ and expanding the TMR up to the first order in $\Gamma/(k_B T)$, the TMR at the intersection of regimes B, C and D can be approximated by

$$\mathrm{TMR}^{\mathrm{B|C|D}} = \frac{p^2}{1-p^2}\left\{1 - \frac{\Gamma}{4\pi k_B T}\left[\ln\left(\frac{|\varepsilon|}{\pi k_B T}\right) - \Psi\left(\frac{1}{2}\right)\right]\right\} \,, \tag{4.41}$$
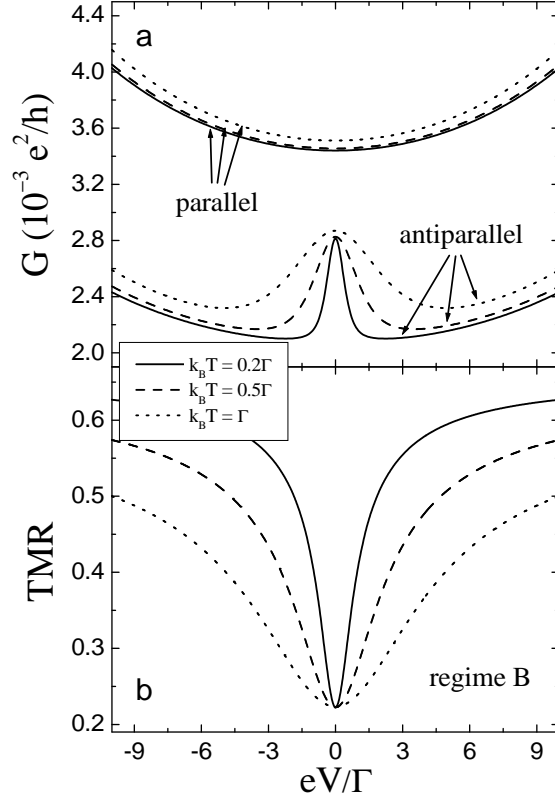
Figure 4.13:   The differential conductance (a) for the parallel and antiparallel configurations and the tunnel magnetoresistance (b) as a function of the bias voltage for different values of temperature. The maximum in differential conductance for antiparallel configuration at zero bias is clearly demonstrated. The other parameters are the same as in Fig. 4.12. Figure was generated using the scheme for the perturbation expansion in the Coulomb blockade regime.

with $\Psi(x)$ being the digamma function, $\Psi(1/2) \simeq -1.96$.

   In order to elucidate and understand the anomalous behavior of TMR in the Coulomb blockade regime, we show in Fig. 4.13a the differential conductance in the small bias regime for both parallel and antiparallel configurations. Figure 4.13b displays the TMR effect for several temperatures. First of all, one can see that the TMR effect in regime B for $|eV| \gg k_{\mathrm{B}}T$ increases with lowering temperature and approaches the Jullière's value. Whereas, the minimum at zero bias does not depend on temperature, as can be seen in Fig. 4.13b. The differential conductance in the parallel alignment has characteristics typical of the cotunneling regime, with a smooth parabolic dependence on the bias voltage. For antiparallel configuration, on the other hand, differential conductance has a local maximum at zero bias, followed by local minimum with increasing bias, as illustrated in Fig. 4.13a. This zero-bias anomaly stems from the interplay
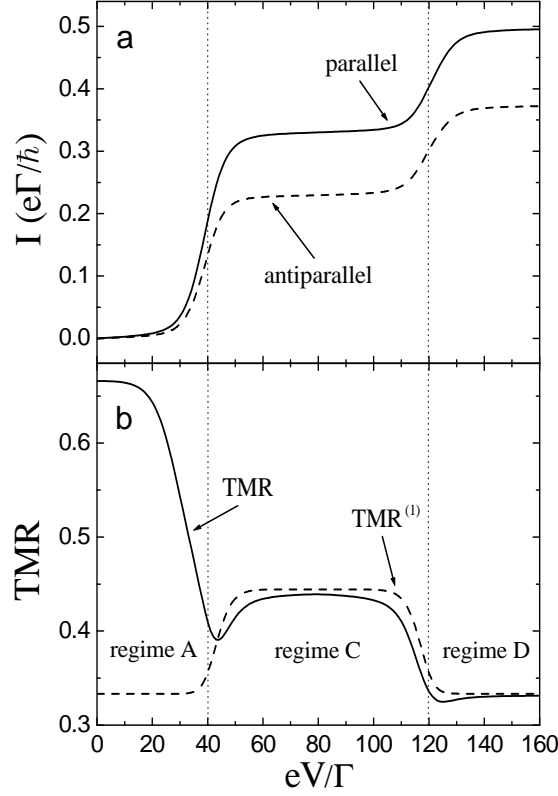
Figure 4.14: The total current (a) in the parallel (solid line) and antiparallel (dashed line) magnetic configurations as a function of the bias voltage. Part (b) shows the first-order contribution to TMR (dashed line) and the total TMR (solid line). The parameters are: $k_B T = 1.5\Gamma$, $\varepsilon = 20\Gamma$, $U = 40\Gamma$, and $p = 0.5$. The figure was generated using the perturbation expansion in the presence of sequential tunneling.

of the spin-flip and non-spin-flip single-barrier and double-barrier cotunneling processes [104]. The minimum in the TMR effect is a direct consequence of anomalous behavior of differential conductance in the antiparallel configuration. The mechanism and main features of this zero-bias anomaly will be presented and discussed in the next section.

The current for parallel and antiparallel configurations and the resulting TMR for the situation when the dot level lies above the Fermi energy of the leads is shown in Fig. 4.14. The first-order TMR is also shown for comparison. In this case, one crosses over from regime A via C to D as the bias voltage is increased. At low voltage, the dot is empty (regime A) and the current is mediated by non-spin-flip cotunneling, with the TMR given by the Jullière's value. In regime C, the first-order processes dominate transport. The second-order processes, however, slightly reduce the TMR effect as compared to the sequential tunneling value. In

order to find an approximate analytic expression for this case, we consider the case of zero temperature, expand the TMR up to the first order in Γ and assume $|\varepsilon|/U \ll 1$, then we get

$$\mathrm{TMR}^{\mathrm{C}} = \frac{p^2}{1-p^2}\left[\frac{4}{3} - \frac{(27 + 34p^2 + 3p^4)\Gamma}{18\pi(1-p^2)\varepsilon}\right] . \qquad (4.42)$$

The second term in the bracket of the above expression describes the renormalization of the first-order TMR due to cotunneling.

Furthermore, it can be seen that at the intersection of regimes A and C the TMR develops a local minimum. This results from the fact that when approaching the intersection from regime C the TMR (dominated by sequential tunneling) decreases while beyond, in regime A, the TMR has to rise again to reach the Jullière's value [107].

In regime D all the four dot states, i.e., $\chi = 0, \uparrow, \downarrow, \mathrm{d}$ take part in transport. This situation is illustrated in Fig. 4.12b and Fig. 4.14b for $eV > 2(\varepsilon + U)$. In regime D, transport is dominated by the first-order processes and the influence of second-order processes is negligible. Consequently, the value of total TMR in regime D is well described by Eq. (4.31), as can be seen in Figs. 4.12b and 4.14b.

Up to now the considerations were restricted to the case when the dot level was spin degenerate. It is, however, interesting to investigate the behavior of the tunnel magnetoresistance when an external magnetic field is applied to the system. In this situation the spin degeneracy of the dot level can be lifted, consequently, $\varepsilon_\uparrow \neq \varepsilon_\downarrow$. As shown below, a finite Zeeman splitting, $\Delta = \varepsilon_\downarrow - \varepsilon_\uparrow$, changes the transport characteristics substantially. Figure 4.15 illustrates the gate and bias voltage dependence of tunnel magnetoresistance for $\Delta = 4\Gamma$. First of all, it can be seen that a finite Zeeman splitting affects the TMR mainly in regimes A (A') and B, where the second-order processes dominate. Furthermore, TMR exhibits a distinctively different behavior in regimes A and A'. It is increased in the case of empty dot, whereas in the case of doubly occupied dot, the TMR is much decreased and may even become negative. This effect depends on the direction of applied magnetic field and, when the field is applied in opposite direction, $\Delta = -4\Gamma$, there is an enhancement of TMR in regime A' and suppression in regime A, as illustrated in Fig. 4.16. Thus, by changing the sign of the Zeeman splitting (direction of magnetic field) or applying the gate voltage, which changes the dot occupation, it is possible to reduce or enhance the TMR effect considerably. Another interesting feature of TMR displayed in Fig. 4.15 can be seen in regime B. There is a strong asymmetry of TMR with respect to the bias reversal. The TMR is decreased for positive and increased for negative bias voltage. This can also be seen in Fig. 4.16, but in this case for positive transport voltage TMR is larger than for negative bias voltage. The crossover between those two values of TMR takes place roughly at the zero bias. As a consequence, by changing the bias voltage in the small range one can substantially tune the magnitude of

Figure 4.15: The total tunnel magnetoresistance as a function of the bias and gate voltages in the presence of external magnetic field. The parameters are: $k_\mathrm{B}T = 1.5\Gamma$, $\Delta = 4\Gamma$, $U = 40\Gamma$, and $p = 0.5$.
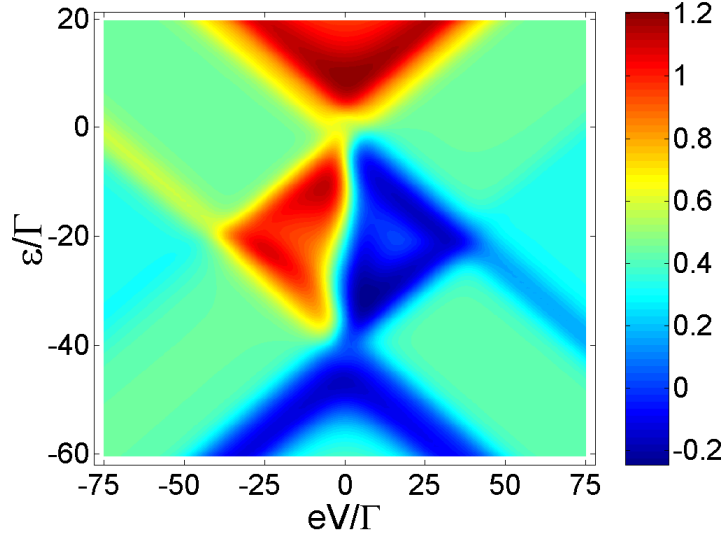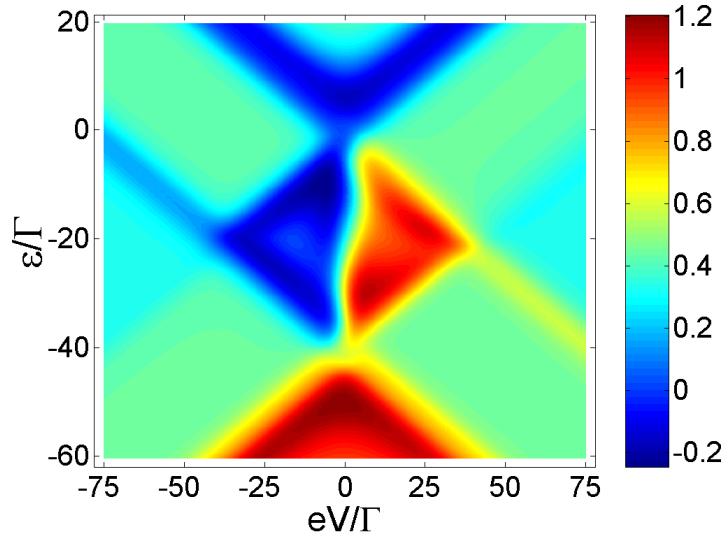

Figure 4.16: The total tunnel magnetoresistance as a function of the bias and gate voltages in the presence of external magnetic field for $\Delta = -4\Gamma$. The other parameters are the same as Fig. 4.15.

the TMR effect. The main properties of second-order transport through quantum dots in the presence of magnetic field will be presented and discussed in the proceeding sections.

In this section we have thoroughly analyzed electronic transport through single-level quantum dots coupled to ferromagnetic leads for the linear and nonlinear response regimes, with an even or odd number of electrons on the dot. We have shown that the behavior of TMR is different in various transport regimes. In particular, it was shown that the value of TMR is below that of a single magnetic tunnel junction, except for the Coulomb blockade valley with an even dot electron number and the Coulomb blockade valley with an odd number of electron on the dot in the case of the nonlinear response regime. This, consequently, results in a strong parity effect of TMR between the Coulomb blockade valleys with an even and odd number of electrons, that is related to the absence or presence of spin-flip cotunneling, respectively. Furthermore, the TMR has a minimum at the zero bias, which results from the anomalous behavior of differential conductance in the antiparallel configuration. It was also demonstrated that a finite Zeeman splitting induced for example by an external magnetic field may substantially modify the tunnel magnetoresistance in the cotunneling regime.

4.5   Zero-Bias Anomaly in the Cotunneling Regime

In the previous section transport characteristics of a quantum dot coupled to ferromagnetic leads were analyzed in the whole range of parameters. In particular, in the case of Coulomb blockade regime and singly occupied dot (regime B) the zero-bias anomaly in differential conductance in the antiparallel configuration was found. In the following, the mechanism and main features of this anomaly are presented and discussed both in the case of spin-degenerate and spin-split dot level.

In order to calculate the current in the Coulomb blockade regime we employ the perturbation scheme in the absence of sequential tunneling, as described in subsection 4.2.2. The same results, however, can be obtained within the Averin-Nazarov approach [104].

4.5.1   Results in the Absence of Magnetic Field

First, we consider the case of spin-degenerate dot level. The differential conductance as a function of the bias voltage for different values of spin polarization of the leads and temperature is shown in Fig. 4.17. In the parallel configuration, we find a typical parabolic behavior of the cotunneling conductance with increasing bias voltage. This is distinctively different for the antiparallel configuration, for which a zero-bias anomaly appears. As illustrated in Fig. 4.17a,
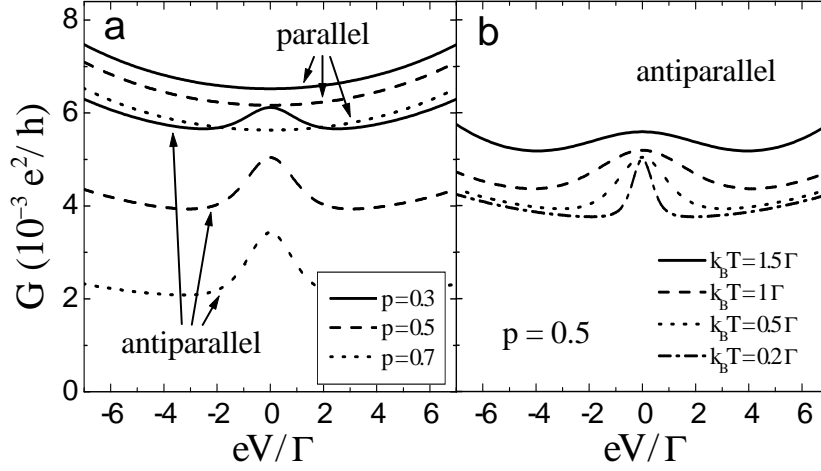
73

Figure 4.17: Differential conductance in the parallel and antiparallel configurations as a function of bias voltage for different values of spin polarization (a) and for different temperatures (b). The other parameters are $k_\mathrm{B}T = 0.5\Gamma$, $\varepsilon = -U/2$, $U = 30\Gamma$, and $p = 0.5$ in part (b).

the differential conductance in the antiparallel configuration strongly depends on the spin polarization – when spin polarization increases the conductance is generally decreased. The bias voltage dependence of the conductance for different temperatures is shown in Fig. 4.17b. It can be seen that the width of the peak increases with increasing temperature. In order to understand the behavior of the differential conductance in a more intuitive way, we present some approximative expressions for the zero-bias peak. When considering the case of deep Coulomb blockade regime, one can neglect corrections in the ratio x/y with $x = |eV|, k_\mathrm{B}T$ and $y = |\varepsilon|, \varepsilon + U$, then the differential conductance in the parallel configuration can be expressed as

$$G^\mathrm{P} = \frac{e^2}{h}\frac{\Gamma^2}{2}\left[\frac{1}{\varepsilon^2} + \frac{1}{(\varepsilon + U)^2} + \frac{1 - p^2}{|\varepsilon|(\varepsilon + U)}\right]. \tag{4.43}$$

The above result is independent of $|eV|/k_\mathrm{B}T$. For the antiparallel configuration one finds

$$G^\mathrm{AP}_\mathrm{max} = \frac{e^2}{h}\frac{\Gamma^2}{2}(1 - p^2)\left[\frac{1}{\varepsilon^2} + \frac{1}{(\varepsilon + U)^2} + \frac{1}{|\varepsilon|(\varepsilon + U)}\right] \tag{4.44}$$

in the linear response regime, $|eV| \ll k_\mathrm{B}T$, and

$$G^\mathrm{AP}_\mathrm{min} = \frac{e^2}{h}\frac{\Gamma^2}{2}\frac{1 - p^2}{1 + p^2}\left[\frac{1}{\varepsilon^2} + \frac{1}{(\varepsilon + U)^2} + \frac{1 - p^2}{|\varepsilon|(\varepsilon + U)}\right] \tag{4.45}$$

for the nonlinear response ($|eV| \gg k_\mathrm{B}T$). First of all, one can see that conductance in the parallel configuration is generally larger than conductance in the

74

antiparallel configuration. Furthermore, from the above expressions it can be seen that $G_{\text{max}}^{\text{AP}} > G_{\text{min}}^{\text{AP}}$, which leads to a zero-bias peak. In order to describe the peak, it is useful to introduce a quantity describing its *relative* height, defined as

$$x_{\text{G}} \equiv \frac{G_{\text{max}}^{\text{AP}} - G_{\text{min}}^{\text{AP}}}{G_{\text{min}}^{\text{AP}}}, \qquad (4.46)$$

which, after plugging Eqs. (4.44) and (4.45), is given by

$$x_{\text{G}} = \frac{p^2 U^2}{(1 + p^2)\varepsilon(\varepsilon + U) + U^2}. \qquad (4.47)$$

The relative height increases from $x_{\text{G}} = p^2$ for $|\varepsilon| \ll \varepsilon + U$ or $|\varepsilon| \gg \varepsilon + U$ to $x_{\text{G}} = 4p^2/(3 - p^2)$ in the middle of the Coulomb blockade valley ($\varepsilon = -U/2$).

The main properties of the zero-bias anomaly can be written in several points listed in the following:

- The crossover from $G_{\text{max}}^{\text{AP}}$ to $G_{\text{min}}^{\text{AP}}$ is around $|eV| \approx k_{\text{B}}T\sqrt{8/(1 + p^2)}$, i.e., the width of the zero-bias anomaly scales linearly with temperature and depends only weakly on polarization.

- The *relative* peak height x_{G} increases monotonically with polarization and when moving from the edges towards the middle of the Coulomb blockade valley.

- The *absolute* peak height $G_{\text{max}}^{\text{AP}} - G_{\text{min}}^{\text{AP}}$ depends nonmonotonically on polarization, since it vanishes for $p = 0$ and $p = 1$.

- At low temperature both $G_{\text{max}}^{\text{AP}}$ and $G_{\text{min}}^{\text{AP}}$ increase with temperature, $G_{\text{max,min}}^{\text{AP}}(T)/G_{\text{max,min}}^{\text{AP}}(0) = 1 + (T/B)^2 + \mathcal{O}(T^4)$ with the same constant B, such that x_{G} is nearly independent of temperature.

It is worth noting that the zero-bias anomaly in the cotunneling regime is qualitatively similar to the maximum due to the Kondo effect, which occurs in the strong coupling limit [110, 111, 112]. There are, however, some distinct differences. First of all, processes responsible for the zero-bias anomaly in the cotunneling regime are of the second order in tunneling processes, while these leading to the Kondo effect are of higher than second order. The conductance in the cotunneling regime is much smaller than in the Kondo regime, where almost perfect transmission ($G = e^2/h$) through the dot is possible owing to the Kondo peak in the density of states at the Fermi level. Furthermore, the Kondo peak occurs at temperatures lower than the so-called Kondo temperature, $T \lesssim T_{\text{K}}$, and exists also in the parallel configuration [109, 113].

4.5.2 Mechanism of the Zero-Bias Anomaly

To understand the mechanism of the zero-bias anomaly it is crucial to distinguish between different types of cotunneling processes. They are illustrated in Fig. 4.3. In the following, however, we focus only on the cotunneling processes that are responsible for the occurrence of the zero-bias peak. These are the single-barrier cotunneling processes shown in Fig. 4.18a and double-barrier cotunneling processes illustrated in Fig. 4.18b. As already pointed in section 4.3 both single-barrier and double-barrier processes can be either spin-flip or non-spin-flip ones. The current flows due to double-barrier cotunneling, whereas the single-barrier cotunneling can influence the current in an indirect way, by changing the magnetic state of the dot. In the antiparallel configuration, there is a finite spin accumulation on the dot, as presented in Fig. 4.18c. The different occupation probabilities for spin-up and spin-down electrons appear due to spin asymmetry in tunneling processes, i.e., when the spin-flip cotunneling rates that change the dot state from $|\uparrow\rangle$ to $|\downarrow\rangle$ and $|\downarrow\rangle$ to $|\uparrow\rangle$ are different from each other. In equilibrium, both rates are equal and, consequently, there is no spin accumulation, $P_\uparrow = P_\downarrow$. When, however, a bias voltage is applied and the system is in the antiparallel configuration, the situation is different. The amount of single-barrier cotunneling is diminished as compared to the double-barrier cotunneling. This is because the rate of single-barrier cotunneling is proportional to thermal energy, whereas that of double-barrier cotunneling is proportional to the bias voltage. In the nonlinear response regime, only the two spin-flip processes that transfer an electron from the left to the right leads determine the magnetic state of the dot.
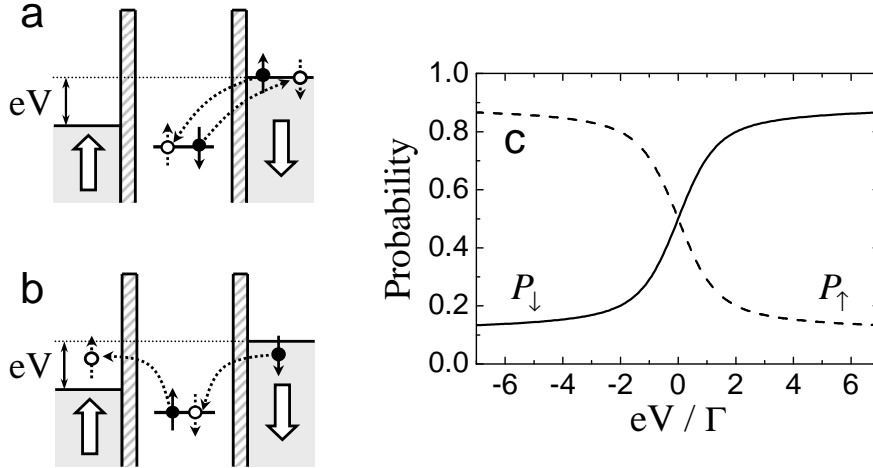

Figure 4.18: Single-barrier (a) and double-barrier (b) cotunneling processes, and the occupation probabilities for spin-up and spin-down electrons in the antiparallel configuration (c). The parameters are $k_B T = 0.5\Gamma$, $\varepsilon = -U/2$, $U = 30\Gamma$, and $p = 0.5$.

The one shown in Fig. 4.18b changes the dot spin from $|\uparrow\rangle$ to $|\downarrow\rangle$. Because the rate of this process is proportional to a product of densities of states for majority electrons, the corresponding rate is larger than that of the other process that changes the dot spin from $|\downarrow\rangle$ to $|\uparrow\rangle$, where only the minority spins are involved. This results in a nonequilibrium spin accumulation $P_\downarrow > P_\uparrow$ that increases with increasing voltage, as shown in Fig. 4.18c. The initial state for the dominant spin-flip cotunneling process that contributes to the current is $|\uparrow\rangle$, as sketched in Fig. 4.18b. Thus, due to the spin accumulation ($P_\downarrow > P_\uparrow$) conductance is decreased. This is the mechanism by which spin accumulation gives rise to nonzero tunnel magnetoresistance effect, $G^{\mathrm{P}} > G^{\mathrm{AP}}$, see Fig. 4.13b.

Because the spin accumulation decreases transport, thus, any spin-flip process, that reduces the spin accumulation will enhance the conductance. In particular, single-barrier spin-flip cotunneling is such a process. As pointed in previous paragraph, the rate of single-barrier processes scales with $k_\mathrm{B}T$ while that of double-barrier cotunneling is proportional to $\max\{|eV|, k_\mathrm{B}T\}$, which explains the mechanism of the zero-bias anomaly. At low bias voltage, $|eV| \lesssim k_\mathrm{B}T$, single-barrier spin-flip processes play a significant role – they decrease the spin accumulation and, thus, open the system for the fastest double-barrier cotunneling. As a consequence, the current increases relatively fast with applied bias, leading to a maximum in differential conductance. For $|eV| \gg k_\mathrm{B}T$, on the other hand, the relative role of single-barrier processes is negligible as compared to double-barrier cotunneling, and the conductance is reduced. Thus, it is the interplay between the rates of double-barrier and single-barrier cotunneling processes that leads to the maximum in the differential conductance at the zero bias.

4.5.3   Results in the Presence of Magnetic Field

If an external magnetic field is applied, the dot level becomes spin-split. Furthermore, when the splitting $\Delta = \varepsilon_\downarrow - \varepsilon_\uparrow$ is larger than thermal energy and bias voltage, $|\Delta| \gg \max\{k_\mathrm{B}T, |eV|\}$, only the lower spin level is occupied and the dot is fully polarized, which results in a complete suppression of the spin-flip cotunneling, thus, leading to a reduction of conductance. This can be seen in Fig. 4.19, where the bias voltage dependence of differential conductance in both the parallel and antiparallel configurations for symmetric and asymmetric Anderson model is displayed. When using the same assumptions as the ones used in the case of spin-degenerate dot level, one can find approximative expressions for the plateaus in differential conductance. They are given by

$$G_{\mathrm{field}}^{\mathrm{P}} = \frac{e^2}{h}\frac{\Gamma^2}{4}\left[\frac{(1+p)^2}{(\varepsilon - |\Delta|/2)^2} + \frac{(1-p)^2}{(\varepsilon + U + |\Delta|/2)^2}\right], \qquad (4.48)$$

for the parallel configuration, whereas for the antiparallel configuration one finds

$$G_{\mathrm{field}}^{\mathrm{AP}} = \frac{e^2}{h}\frac{\Gamma^2}{4}(1-p^2)\left[\frac{1}{(\varepsilon - |\Delta|/2)^2} + \frac{1}{(\varepsilon + U + |\Delta|/2)^2}\right]. \qquad (4.49)$$
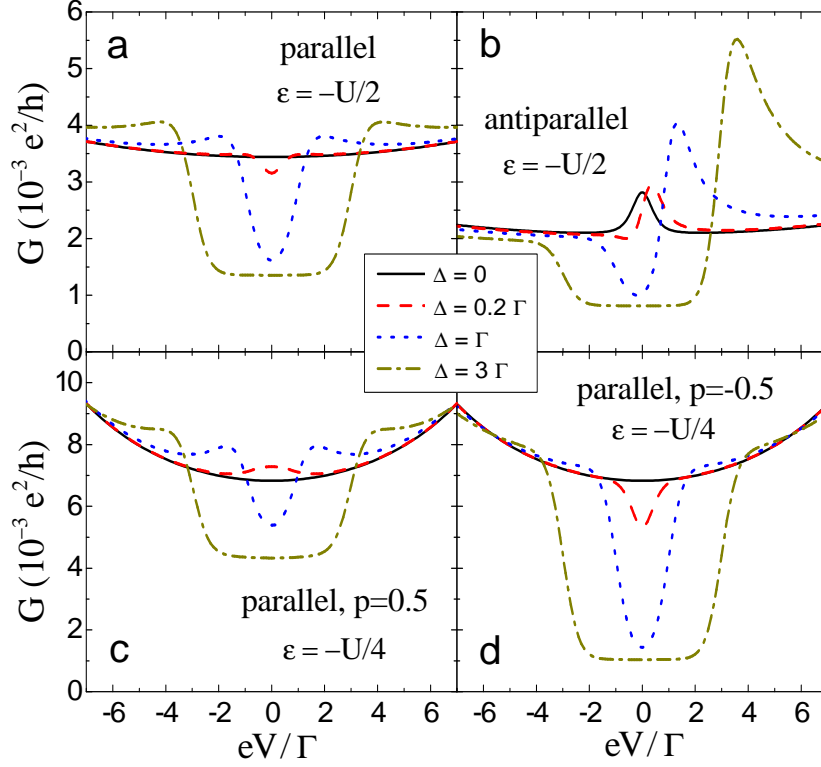
Figure 4.19:   Differential conductance in the presence of a Zeeman splitting with $p = 0.5$ in parts (a,b,c) and $p = -0.5$ in part (d) for the symmetric (a,b) and asymmetric (c,d) Anderson model with parallel (a,c,d) and antiparallel (b) relative magnetization of the leads. The other parameters are: $k_\mathrm{B}T = 0.2\Gamma$, and $U = 40\Gamma$.

The above expressions describe the plateau in differential conductance due to the suppression of spin-flip cotunneling. When, however, the bias voltage is increased such that $|eV| \sim |\Delta| \gg k_\mathrm{B}T$, spin-flip processes are again possible, and the conductance increases. In the antiparallel magnetic configuration, the conductance is asymmetric under the reversal of bias voltage. This is illustrated in Fig. 4.19b.

In order to understand this behavior it is crucial to realize that when the dot level splitting $\Delta = \varepsilon_\downarrow - \varepsilon_\uparrow$ is positive and larger than thermal energy, the single-barrier spin-flip cotunneling processes can occur only when the dot is occupied by a spin-down electron. This follows simply from the energy conservation rule. (The situation may be changed for negative Δ.) Thus, the single-barrier processes can assist the fastest double-barrier cotunneling processes, but only for positive bias voltage. This is because the fastest processes can occur when the dot is occupied by a spin-down electron for negative transport voltage and by a spin-up electron for positive voltage. As a consequence, the differential conductance is

larger for negative bias voltage than for positive one. This is indeed the case in the characteristics shown in Fig. 4.19b. Apart from this, if $|eV| < |\Delta|$ then the double-barrier spin-flip processes are also energetically forbidden, which results in a broad plateau in the conductance in the small bias voltage range.

In the parallel configuration, there is again a plateau for $\max\{k_BT, |eV|\} \ll |\Delta|$ due to the suppression of spin-flip cotunneling processes, as shown in Fig. 4.19a. In addition, it can be seen that for an asymmetric Anderson model (Fig. 4.19c and d) the differential conductance significantly depends on the spin polarization p. In the situation shown in Fig. 4.19c, a weak maximum in the conductance at small bias voltage appears for weak magnetic fields, which subsequently develops into a broad minimum for large fields. This does not take place for the opposite polarization factor, as shown in Fig. 4.19d.

In the present section we have presented the main properties and mechanism of the zero-bias anomaly in differential conductance found in the cotunneling regime when the leads are magnetized antiparallel to each other. It was shown that this zero-bias anomaly originates from the interplay of single-barrier and double-barrier spin-flip cotunneling processes. From an experimental point of view, the anomaly may be observed in quantum dots and/or molecules attached to ferromagnetic leads, which include an odd number of electrons. Such structures have already been realized experimentally [97, 98, 99, 100, 109, 119].

Finally, it is worth noting that no zero-bias anomaly occurs in the Coulomb blockade valleys with an even number of electrons (empty dot for $\varepsilon > 0$ and doubly occupied dot for $\varepsilon + U < 0$), as in this case the total dot spin is zero, and spin accumulation is absent.

4.6 Effects of Intrinsic Spin Relaxation in the Dot on Transport in the Cotunneling Regime

In the following, we discuss the impact of intrinsic spin relaxation in the dot on conductance of a quantum dot coupled to ferromagnetic leads in the cotunneling regime. In particular, we consider the cases of a dot symmetrically and asymmetrically coupled to the leads. The latter case is of particular interest as the corresponding transport characteristics are typical of diodes, i.e., they are highly asymmetric with respect to bias reversal. It is further shown that the diode-like behavior in the cotunneling regime is suppressed by the intrinsic spin flip processes on the dot.

In order to analyze the transport properties in the cotunneling regime we use the Averin-Nazarov approach. This approach was outlined in section 4.3. In numerical calculations we have included all possible cotunneling events. Furthermore, the intrinsic spin relaxation processes on the dot are also considered [91]. These processes have been taken into account *via* a relaxation term in the

appropriate master equation for the occupation probabilities

$$0 = \sum_{r,r'=\mathrm{L,R}} (-\gamma_{rr',\sigma\Rightarrow\bar{\sigma}}P_\sigma + \gamma_{rr',\bar{\sigma}\Rightarrow\sigma}P_{\bar{\sigma}}) - \frac{P_\sigma - P_{\bar{\sigma}}}{\tau_{\mathrm{sf}}} , \qquad (4.50)$$

where τ_{sf} is the spin relaxation time on the quantum dot. The occupation probabilities can be determined from the above master equation together with normalization condition, Eq. (4.29). The respective expressions for cotunneling rates are given in appendix B.1. Having found the corresponding second-order transition rates, one can calculate the electric current from Eq. (4.30).

4.6.1   Symmetrical Systems

We consider the case when the dot is singly occupied at equilibrium and the system is in a deep Coulomb blockade regime, $\Gamma, k_\mathrm{B}T \ll |\varepsilon_\sigma|, \varepsilon_\sigma + U$. This transport regime corresponds to regime B, as illustrated in Fig. 4.4. The sequential tunneling is then exponentially suppressed, and cotunneling gives the dominant contribution to electric current. Both non-spin-flip and spin-flip cotunneling processes are then allowed, as described in the previous sections. In the following, the influence of intrinsic spin relaxation on transport characteristics both in the presence and absence of external magnetic field is presented and discussed.

In the case of $\Delta = 0$ the dot level is spin degenerate, $\varepsilon_\uparrow = \varepsilon_\downarrow = \varepsilon$. The differential conductance for parallel and antiparallel magnetic configurations in the case of symmetric coupling of the dot to the leads is shown in Fig. 4.20. In the parallel configuration one finds typical parabolic behavior of the conductance with increasing transport voltage, whereas in the antiparallel configuration a maximum in differential conductance in the small bias regime appears, as presented in the preceding section. The anomalous behavior of differential conductance in turn leads to respective minimum in tunnel magnetoresistance, as shown by the solid curve in Fig. 4.20c.

Physical mechanism of the zero-bias anomaly was discussed in the previous section for the case of no spin relaxation, where it was pointed out that the anomalous behavior of differential conductance results from the spin asymmetry of tunneling processes and the subtle interplay of single-barrier and double-barrier cotunneling processes. The spin asymmetry of tunneling processes leads effectively to nonequivalent occupation of the dot by spin-up and spin-down electrons (spin accumulation), as illustrated in Fig. 4.18c and Fig. 4.21. Figure 4.21 shows the spin accumulation, defined as $(P_\uparrow - P_\downarrow)/2$, as a function of the bias voltage for different spin relaxation times. It can be seen that the accumulation is decreased as the relaxation time becomes shorter. From the discussion presented in subsection 4.5.2 follows that spin accumulation is crucial for the occurrence of the zero-bias anomaly. Thus, one may expect that intrinsic spin-flip processes on the dot should suppress the anomaly. Now we show that this is indeed the
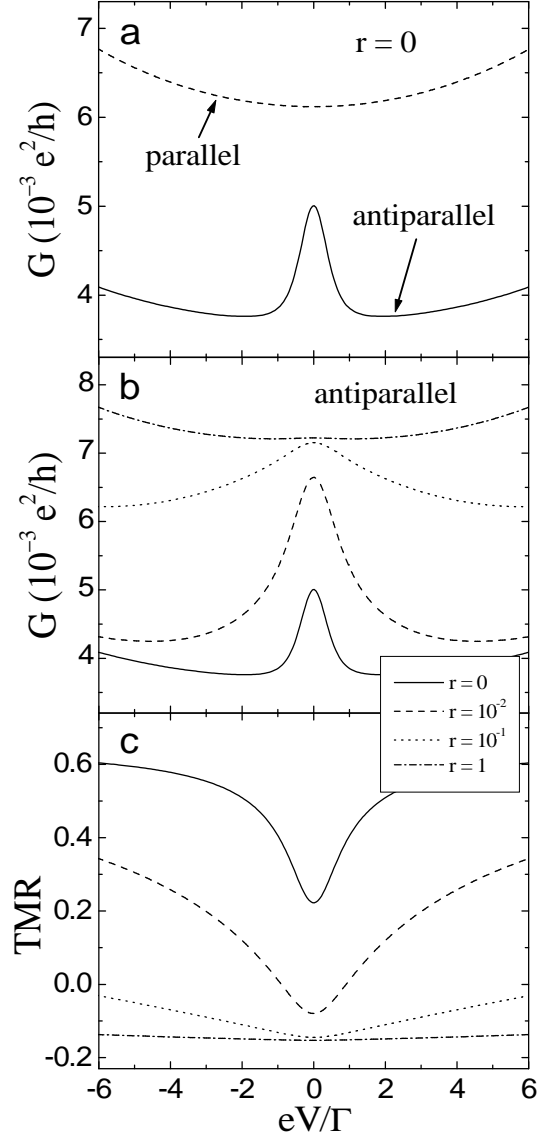
Figure 4.20: The differential conductance in the parallel and antiparallel configurations (a,b) and tunnel magnetoresistance (c) as a function of the bias voltage for different spin relaxation $r = h/(\tau_{\mathrm{sf}}\Gamma)$. The parameters are $k_{\mathrm{B}}T = 0.2\Gamma$, $\varepsilon = -15\Gamma$, $U = 30\Gamma$, and $p = 0.5$.

case, i.e., intrinsic spin relaxation on the dot significantly modifies the conductance maximum at zero bias, and, eventually, totally suppresses the anomaly in the limit of fast spin relaxation. This behavior is displayed in Fig. 4.20b, where different curves correspond to different values of the parameter r defined as $r = h/(\Gamma\tau_{\mathrm{sf}})$. Thus, the case of $r = 0$ corresponds to the situation with no intrinsic spin relaxation, whereas the curves corresponding to nonzero r describe

Figure 4.21: The spin accumulation in the antiparallel configuration as a function of the bias voltage for different spin relaxation $r = h/(\tau_{\mathrm{sf}}\Gamma)$. The parameters are the same as in Fig. 4.20.

the influence of the relaxation processes. First of all, it can be seen that small amount of intrinsic spin-flip processes enhances the zero-bias anomaly. This is because the spin-flip processes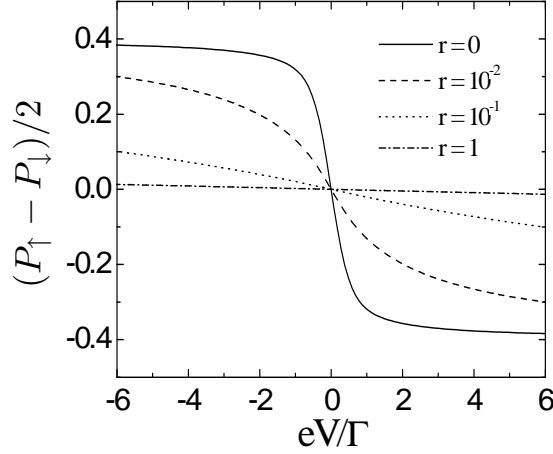 on the dot play a role similar to that of single-barrier spin-flip cotunneling, thus, reducing the spin accumulation. In the limit of fast spin relaxation, on the other hand, the spin accumulation is suppressed and the anomaly disappears, see Fig. 4.20b and Fig. 4.21 for $r = 1$. It is also worth noting that spin-flip processes on the dot enhance the overall conductance. In the parallel configuration, however, the differential conductance does not depend on intrinsic relaxation. This is because there is no spin accumulation in the parallel configuration. Consequently, the spin-flip processes on the dot do not play any role.

Intrinsic spin-flip scattering on the dot modifies conductance in the antiparallel configuration, and this way also the tunnel magnetoresistance, as shown in Fig. 4.20c. Since the zero-bias maximum in conductance is suppressed in the fast spin relaxation limit, the corresponding minimum in TMR at small bias voltage is also suppressed by the relaxation processes. More specifically, it can be seen that the dip in TMR broadens with increasing r and disappears in the limit of fast relaxation (see the curve for $r = 1$). An interesting feature of the TMR effect in the presence of spin-flip scattering on the dot is the crossover from positive to negative values when r increases, as illustrated in Fig. 4.20c. Thus, the difference between parallel and antiparallel magnetic configurations persists even for fast spin relaxation on the dot, on the contrary to the sequential tunneling regime, where this difference vanishes in this limit [91].

In the case of a deep Coulomb blockade one can take only the lowest order corrections in term x/y, with $x = k_{\mathrm{B}}T, |eV|, y = |\varepsilon|, \varepsilon + U$. It is then possible

to derive some approximate formulas for the differential conductance and TMR. For the parallel configuration the differential conductance is independent of spin relaxation and given by Eq. (4.43). For the antiparallel configuration and in the linear response, $|eV| \ll k_B T$, the conductance can be approximated by the expression

$$
\begin{aligned}
G_{\mathrm{max}}^{\mathrm{AP}} \;=\; & \frac{e^2}{h} \frac{\Gamma^2}{2} \Bigg\{ (1-p^2) \left[\frac{1}{\varepsilon^2} + \frac{1}{(\varepsilon+U)^2} + \frac{1}{|\varepsilon|(\varepsilon+U)} \right] \\
& + \frac{p^2 U^2 h/\tau_{\mathrm{sf}}}{\varepsilon^2(\varepsilon+U)^2 h/\tau_{\mathrm{sf}} + k_B T U^2 \Gamma^2} \Bigg\},
\end{aligned}
\tag{4.51}
$$

which describes the maximum of the differential conductance at zero bias. On the other hand, when $|eV| \gg k_B T$, one finds the formula

$$
\begin{aligned}
G_{\mathrm{min}}^{\mathrm{AP}} = \; & \frac{e^2}{h} \frac{\Gamma^2}{2} \Bigg\{ \frac{1-p^2}{1+p^2} \left[\frac{1}{\varepsilon^2} + \frac{1}{(\varepsilon+U)^2} + \frac{1-p^2}{|\varepsilon|(\varepsilon+U)} \right] \\
& + \frac{4p^2}{1+p^2} \frac{U^2 h/\tau_{\mathrm{sf}}}{2\varepsilon^2(\varepsilon+U)^2 h/\tau_{\mathrm{sf}} + (1+p^2)k_B T U^2 \Gamma^2} \Bigg\},
\end{aligned}
\tag{4.52}
$$

which in turn corresponds to local minimum value of the differential conductance. The latter terms in Eqs. (4.51) and (4.52) are due to spin relaxation processes. The above equations present generalizations of Eqs. (4.44) and (4.45). On the other hand, the relative height of the maximum in differential conductance for antiparallel configuration, given by Eq (4.46), in the case of symmetric Anderson model, $\varepsilon = -U/2$, can be expressed as

$$
x_{\mathrm{G}} = \frac{32p^2(1-p^2)(k_B T)^2 \Gamma^4}{(4k_B T \Gamma^2 + \varepsilon^2 h/\tau_{\mathrm{sf}})\left[2(1-p^2)(3-p^2)k_B T \Gamma^2 + (3+p^2)\varepsilon^2 h/\tau_{\mathrm{sf}} \right]} .
\tag{4.53}
$$

In the limit of no spin relaxation one finds $x_{\mathrm{G}} = 4p^2/(3-p^2)$, whereas in the limit of fast spin relaxation x_{G} tends to zero. This is because spin-flip relaxation processes diminish spin accumulation (and spin accumulation was the necessary condition for the zero-bias anomaly to occur). Indeed, in the limit of fast spin relaxation, $G_{\mathrm{max}}^{\mathrm{AP}}$ and $G_{\mathrm{min}}^{\mathrm{AP}}$ are equal and given by

$$
G^{\mathrm{AP}} = \frac{e^2}{h} \frac{\Gamma^2}{2} \left[\frac{1}{\varepsilon^2} + \frac{1}{(\varepsilon+U)^2} + \frac{1+p^2}{|\varepsilon|(\varepsilon+U)} \right] .
\tag{4.54}
$$

A similar analysis can be performed for tunnel magnetoresistance. In the case of a symmetric Anderson model the minimum in TMR at zero bias can be expressed as

$$
\mathrm{TMR}_{\mathrm{min}} = \frac{2p^2\left(4k_B T \Gamma^2 - \varepsilon^2 h/\tau_{\mathrm{sf}}\right)}{12(1-p^2)k_B T \Gamma^2 + (3+p^2)\varepsilon^2 h/\tau_{\mathrm{sf}}},
\tag{4.55}
$$

Figure 4.22: The spin relaxation time dependence of the linear conductance in the antiparallel configuration (a) and the resulting TMR (b). The parameters are the same as in Fig. 4.20.

whereas for $|eV| \gg k_{\mathrm{B}}T$ one finds

$$\mathrm{TMR}_{\max} = \frac{2p^2 \left[2(3-p^2)k_{\mathrm{B}}T\Gamma^2 - \varepsilon^2 h/\tau_{\mathrm{sf}}\right]}{2(1-p^2)(3-p^2)k_{\mathrm{B}}T\Gamma^2 + (3+p^2)\varepsilon^2 h/\tau_{\mathrm{sf}}} \; . \tag{4.56}$$

The latter formula approximates the value of TMR corresponding to the bias voltage at which differential conductance has local minimum. In the limit of long spin relaxation one finds $\mathrm{TMR}_{\min} = 2p^2/3(1-p^2)$, and $\mathrm{TMR}_{\max} = 2p^2/(1-p^2)$, see Eq. (4.39). On the other hand, in the limit of short spin relaxation TMR becomes negative and is given by

$$\mathrm{TMR} = -\frac{2p^2}{3+p^2} \; , \tag{4.57}$$

independent of $|eV|/k_{\mathrm{B}}T$. This is consistent with numerical results shown in Fig. 4.20c.

As follows from the results described above, the intrinsic spin relaxation on the dot has a significant influence on transport characteristics. The zero-bias anomaly
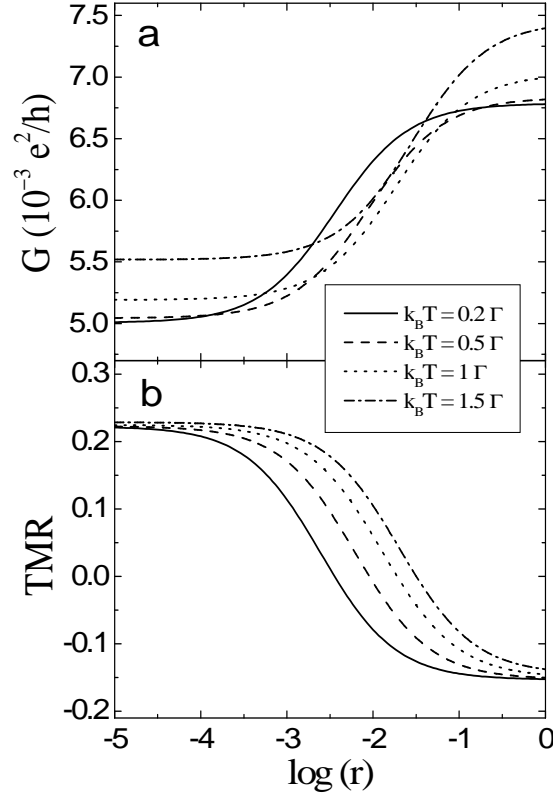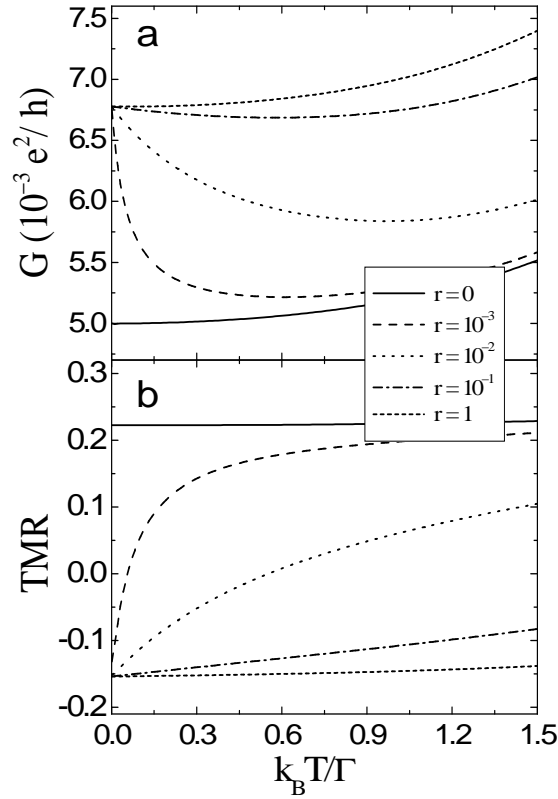
Figure 4.23:   The temperature dependence of the linear conductance in the antiparallel configuration (a) and the resulting TMR (b) for the same parameters as in Fig. 4.20.

in the antiparallel configuration and minimum in TMR become suppressed by the spin-flip processes. Variation of the conductance and TMR with the parameter r is shown explicitly in Fig. 4.22a and b, where the transition between slow and fast spin relaxation on the dot is clearly evident. Different curves correspond to different values of temperature. One can see that the crossover between the limit of fast and slow relaxation time is slightly shifted towards longer relaxation times as temperature increases.

The temperature dependence of the conductance and tunnel magnetoresistance is illustrated in Fig. 4.23a and b, where different curves correspond to different values of the parameter r. The TMR effect in the limit of slow and fast relaxation is almost independent of temperature. However, in the crossover between those two regimes the tunnel magnetoresistance reveals a strong dependence on temperature, and so does the linear conductance.

The discussion up to now was limited to the case of a spin-degenerate dot level. The situation changes when $\varepsilon_\uparrow \neq \varepsilon_\downarrow$, e.g., due to an external magnetic field. The magnetic field splits the dot level, consequently the occupation probabilities for
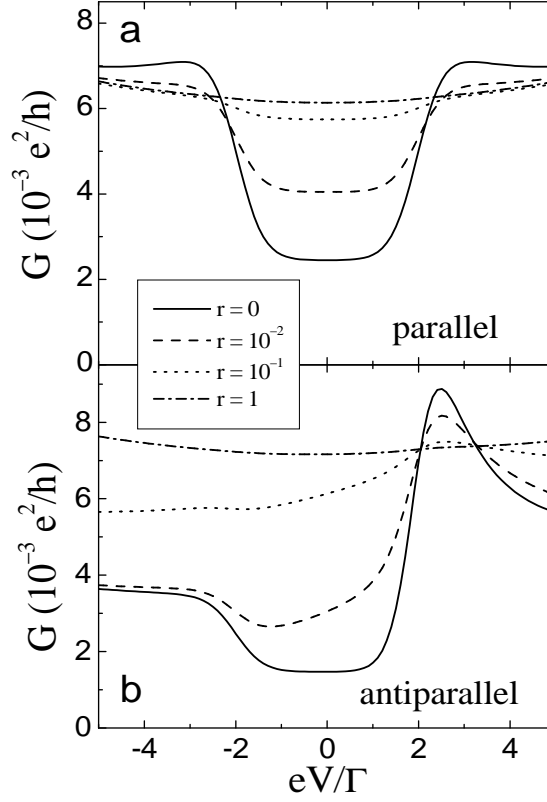
Figure 4.24: The differential conductance in the nonlinear response regime for different spin relaxation in the parallel (a) and antiparallel (b) configurations. The parameters are: $k_{\mathrm{B}}T = 0.2\Gamma$, $\varepsilon_\uparrow = -16\Gamma$, $\varepsilon_\downarrow = -14\Gamma$, $U = 30\Gamma$ and $p = 0.5$.

the spin-up and spin-down electrons are not equal even at equilibrium ($V = 0$). The level splitting is described by the parameter $\Delta = \varepsilon_\downarrow - \varepsilon_\uparrow$, where the magnetic field is assumed to be along the magnetic moment of the left electrode. In Fig. 4.24 we show the bias dependence of the differential conductance in the parallel and antiparallel configurations for different values of spin relaxation parameter r. In the limit of no spin relaxation on the dot (solid line in Fig. 4.24) and at low bias voltage, the dot is occupied by spin-up electron and the current flows mainly due to non-spin-flip cotunneling. Spin-flip cotunneling processes are suppressed for $|\Delta| \geq |eV|, k_{\mathrm{B}}T$, which results in the steps in differential conductance at $|\Delta| \simeq |eV|$, as discussed in previous section. The suppression of the spin-flip inelastic cotunneling was recently used as a tool to determine spin splitting of the dot level and the corresponding spectroscopic g-factor [98]. When $|eV|$ becomes larger than $|\Delta|$, spin-flip cotunneling is allowed, consequently the conductance increases. However, there is a large asymmetry in the antiparallel configuration with respect to bias reversal, as shown in Fig. 4.24b. No such an asymmetry occurs in the parallel configuration, as presented in Fig. 4.24a. The mechanism

of the asymmetry with respect to the bias reversal was discussed in subsection 4.5.3.

The situation changes when intrinsic spin-flip relaxation processes on the dot are present. As the relaxation time becomes shorter, the probability that the spin on the dot is flipped increases. Consequently, there appear a nonzero probability for electrons to tunnel through the spin-down energy level by spin-flip cotunneling processes. This results in an increase of differential conductance. Finally, in the limit of short relaxation time the spin-flip and non-spin-flip cotunneling contribute to the current on equal footing and the gap due to the suppression of spin-flip cotunneling disappears, irrespective of magnetic configuration, as shown in Fig. 4.24 in the case of $r = 1$. Moreover, the asymmetry with respect to the bias reversal in the antiparallel configuration also vanishes.

4.6.2   Asymmetrical Systems

An interesting situation occurs for quantum dots coupled asymmetrically to the left and right leads. For this situation we first present the results in the case of degenerate dot level and then we proceed with the discussion of transport properties in the case where the degeneracy is lifted.

Differential conductance for a system with one electrode nonmagnetic and the other one made of a ferromagnet with large spin polarization (in the following referred to as *strong* ferromagnet) is shown in Fig. 4.25. The parts (a) and (c) correspond to the cases when the dot is described by an asymmetric Anderson model ($|\varepsilon| \neq \varepsilon + U$). The difference between (a) and (c) is due to different position of the dot level ε, and consequently also $\varepsilon + U$, with respect to the Fermi level at equilibrium. More precisely, (a) and (c) are symmetrical in the sense that $|\varepsilon|$ in (a) is equal to $\varepsilon + U$ in (c), and vice-versa, $|\varepsilon|$ in (c) is equal to $\varepsilon + U$ in (a). Part (b), in turn, corresponds to the dot described by a symmetric Anderson model, with $|\varepsilon|$ equal to $\varepsilon + U$.

Consider first the situation in the absence of the spin relaxation on the dot (solid curves in Fig. 4.25). There is then a significant asymmetry of electric current with respect to the bias reversal (diode-like behavior) in the situations displayed in Fig. 4.25a and c, whereas no such an asymmetry occurs for symmetric Anderson model, as can be seen in Fig. 4.25b. Another feature of the curves shown in Fig. 4.25 is the presence of zero-bias anomaly in the case described by symmetric Anderson model [part (b)]. This anomaly is similar to that shown in Fig. 4.20a for antiparallel configuration. The anomaly, however, is less pronounced when the dot is described by asymmetric Anderson model, as clearly visible in Fig. 4.25a and c.

Let us discuss now the physical mechanism of the asymmetry with respect to the bias reversal, displayed in Fig. 4.25a and c. When $|eV| \gg k_{\mathrm{B}}T$, one can neglect the role of single-barrier cotunneling [104]. The cotunneling processes which transfer charge from one lead to the other take place *via* two possible
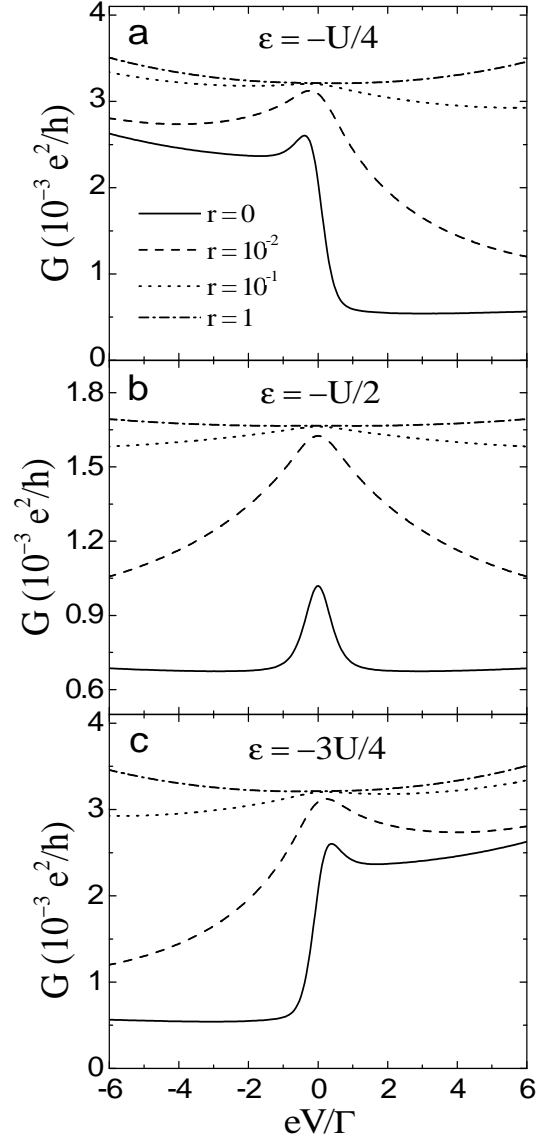
Figure 4.25: The differential conductance in the nonlinear response regime for the asymmetric (a,c) and symmetric (b) Anderson model for different spin relaxation. The parameters are: $k_BT = 0.2\Gamma$, $U = 60\Gamma$, $p_L = 0.95$ and $p_R = 0$.

virtual states – empty dot (an electron residing on the dot tunnels to one of the leads and another electron from the second lead enters the dot) and doubly occupied dot (an electron of opposite spin enters the dot while electron being originally on the dot leaves the dot). Both processes are coherent, consequently the corresponding amplitudes add to each other, see Eq. (B.2). Consider first the situation illustrated in Fig. 4.25a for positive bias ($eV > 0$, electrons flow from right to left, i.e., from normal metal to strong ferromagnet), and assume for clarity

of discussion that the strong ferromagnet is a half-metallic one with full spin polarization (only spin-up electrons can then tunnel to the left lead). When spin-down electron enters the dot, it has no possibility to leave the dot for a long time. The cotunneling processes which are then allowed are those taking place through virtual states with doubly occupied dot. In the absence of intrinsic spin relaxation on the dot, the only processes which can reverse the dot spin are the single-barrier cotunneling ones, which however play a minor role when $k_B T \ll |eV|$. Thus, the current flows due to non-spin-flip cotunneling *via* doubly-occupied dot virtual states, whereas cotunneling through empty-dot virtual states is suppressed. The situation is changed for negative bias (electrons flow from strong ferromagnet to normal metal). Now, the dot is mostly occupied by a spin-up electron (compare with Fig. 4.21), which suppresses cotunneling *via* doubly-occupied dot virtual state and the only contribution comes from cotunneling *via* empty-dot virtual state. The ratio of cotunneling rates through the empty-dot and doubly-occupied dot virtual states is approximately equal to $\xi = [\varepsilon/(\varepsilon + U)]^{-2}$, see Eq. (B.2). In the situation presented in Fig. 4.25a $\xi \ll 1$. Accordingly, the conductance for negative bias is much larger than for positive bias. In turn, in the case displayed in Fig. 4.25c the ratio of the respective cotunneling rates is exactly equal to the inverse of this ratio corresponding to the case shown in Fig. 4.25a. Thus, now we have $\xi \gg 1$, and the conductance is smaller for negative bias than for positive one. In turn, in the case presented in Fig. 4.25b ξ is equal to 1, consequently, both cotunneling rates are equal and the conductance is symmetrical with respect to the bias reversal.

When $|eV|$ becomes of the order of $k_B T$ or smaller, the rate of single-barrier cotunneling events is of the order of the rate of double-barrier cotunneling processes. Therefore, the single-barrier processes can play an important role in transport. More precisely, single-barrier cotunneling processes can reverse spin of an electron on the dot and, thus, can open the system for the fast cotunneling processes. This behavior can be observed in Fig. 4.25a and c. In the symmetric case shown in Fig. 4.25b, the single-barrier processes lead to zero-bias anomaly similar to that shown in Fig. 4.20a for antiparallel configuration in a system with two ferromagnetic electrodes coupled symmetrically to the dot. The mechanism of the anomaly is the same, i.e., the single-barrier cotunneling processes open the system for the fast spin-flip cotunneling, which occurs for $k_B T \gg |eV|$. This leads to an increase in conductance in the small range of the bias voltage. The zero-bias anomaly exists also in asymmetric cases illustrated in Fig. 4.25a and c. However, the maximum in conductance is slightly shifted away from $V = 0$ and is much less pronounced.

Intrinsic spin-flip processes on the dot have similar influence on electronic transport as in the symmetric case studied in the previous section. As before, relaxation processes remove the asymmetry with respect to the bias reversal and suppress the zero-bias anomaly. Thus, the diode-like behavior can appear only in the limit of slow spin relaxation, and is suppressed in the limit of fast spin

relaxation, as shown in Fig. 4.25 by the curves corresponding to $r = 1$.

Simple analytical formula for the conductance in the limit $|eV| \gg k_{\mathrm{B}}T$ can be obtained when assuming $p_{\mathrm{L}} = p$, $p_{\mathrm{R}} = 0$. One can then find approximative formulas for the differential conductance

$$G = \frac{e^2}{h} \frac{\Gamma^2}{2} \left[\frac{1}{(\varepsilon + U)^2} + \frac{(1 - p^2)U}{\varepsilon^2(\varepsilon + U)} + \frac{p^2 \varepsilon^2 U(\varepsilon + U)^3}{\left[\varepsilon^2(\varepsilon + U)^2 - eVU^2\Gamma^2\tau_{\mathrm{sf}}/(4h)\right]^2} \right] \quad (4.58)$$

for positive bias, and

$$G = \frac{e^2}{h} \frac{\Gamma^2}{2} \left[\frac{1}{\varepsilon^2} + \frac{(1 - p^2)U}{|\varepsilon|(\varepsilon + U)^2} + \frac{p^2 |\varepsilon|^3 U(\varepsilon + U)^2}{\left[\varepsilon^2(\varepsilon + U)^2 + eVU^2\Gamma^2\tau_{\mathrm{sf}}/(4h)\right]^2} \right] \quad (4.59)$$

for negative bias. In order to describe the diode operation it is useful to define a ratio of conductance for positive and negative bias voltage ζ. In the limit of long spin relaxation it is given by

$$\zeta = \frac{\varepsilon^2 + (1 - p^2)(\varepsilon + U)U}{(\varepsilon + U)^2 + (1 - p^2)|\varepsilon|U} \, . \quad (4.60)$$

It can be seen from the above expression that the operation of the diode can be tuned by varying the gate voltage (which shifts energy of the dot level).

Figure 4.26 illustrates the influence of spin splitting of the dot level due to applied magnetic field, $\varepsilon_{\uparrow} \neq \varepsilon_{\downarrow}$. The bias voltage dependence of the differential conductance is shown there for different values of the parameter r, for symmetric (b) and asymmetric (a,c) Anderson model. The parameters used in numerical calculations are the same as in Fig. 4.25, except for the dot level energy which was spin degenerate in Fig. 4.25 and now is spin-split.

Let us first focus on Fig. 4.26a, which corresponds to the case of asymmetric Anderson model, $\varepsilon = -U/4$. The two new features of the system conductance in the limit of no spin relaxation appear in this figure. First, the conductance is now suppressed above a certain finite positive value of the bias voltage and this is not for $eV > 0$ as it was in the case shown in Fig. 4.25a. Strictly speaking, the conductance drops when eV is equal to the level splitting Δ, $eV \approx \Delta$. The shift of the main slope in the conductance from $eV = 0$ to $eV \approx \Delta$ is due to the fact that the dot is blocked for cotunneling *via* the empty state by a spin-down electron only when eV exceeds the level splitting. Thus, in the case shown in Fig. 4.25a the main drop of the conductance was at $eV = 0$, whereas in Fig. 4.26a it is at $eV \approx \Delta$. When a spin-down electron appears on the dot, then, for $eV < \Delta$, it can always tunnel back to the source electrode and open the dot for fast cotunneling through the empty state.

The second feature visible in the case of no intrinsic spin relaxation on the dot is the peak in the conductance at $eV = \Delta$, and a shallow plateau in the conductance for $|eV| \leq \Delta$. The origin of the peak is similar to the origin of the zero-bias anomaly in the case of zero splitting of the dot level, i.e., the crucial role
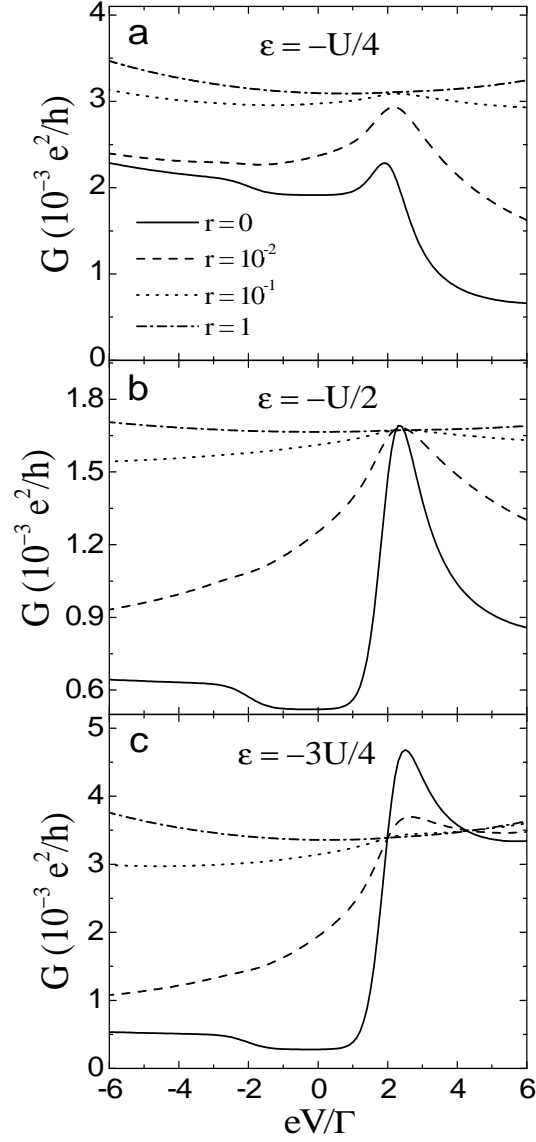
Figure 4.26: The differential conductance in the nonlinear response regime for different spin relaxation. The parameters are: $k_\mathrm{B}T = 0.2\Gamma$, $\varepsilon_\uparrow = \varepsilon - \Delta/2$, $\varepsilon_\downarrow = \varepsilon + \Delta/2$, $\Delta = 2\Gamma$, $U = 60\Gamma$, $p_\mathrm{L} = 0.95$ and $p_\mathrm{R} = 0$.

plays the single-barrier cotunneling, whereas the plateau in the small bias voltage range is due to suppression of the spin-flip cotunneling for $eV < \Delta$, similarly as in the case presented in Fig. 4.24. However, the plateau is now very weak and shallow. This is due to the minor role of spin-flip cotunneling, which follows from the strong spin polarization of the ferromagnetic electrode.

Qualitatively similar behavior may also be observed for the case when $\varepsilon = -3U/4$. This situation is shown in Fig. 4.26c and is analogous to the one illus-

trated in Fig. 4.25c. In the case of $\varepsilon = -U/2$ shown in Fig. 4.26b, the influence of magnetic field is qualitatively similar to that found in the case of a quantum dot coupled to two ferromagnetic leads in the antiparallel configuration, see Fig. 4.24.

Once the spin relaxation on the dot appears, all the features discussed above become suppressed by the relaxation processes and disappear in the limit of fast spin relaxation. This is shown by the curves corresponding to $r = 1$ in Fig. 4.26.

In this section the influence of intrinsic spin relaxation on the dot on the differential conductance and the TMR effect in the cotunneling regime was considered both numerically and analytically. It was shown that the spin-flip processes can decrease and eventually suppress totally both the zero-bias anomaly in the antiparallel magnetic configuration and the minimum in tunnel magnetoresistance at zero bias. Moreover, in the limit of short spin relaxation time the TMR effect may become negative.

It was also shown that the zero-bias anomaly exists in systems with only one ferromagnetic electrode (the second one may be nonmagnetic). Such devices have transport characteristics typical of diodes. This behavior exists also when the system is in an external magnetic field, but the operation range is changed, i.e., the bias at which the conductance drops depends on the level splitting. This behavior is strongly suppressed by intrinsic spin relaxation processes on the dot.

Finally, it is interesting to note that spin relaxation effects do not play any role in the case of Coulomb blockade valleys with even number of electrons on the dot, because the dot is unpolarized.

Chapter 5

Transport through Quantum Dots Coupled to Ferromagnetic Leads with Noncollinear Magnetizations

Previous chapters dealt with spin-polarized transport through quantum dots coupled to ferromagnetic leads in the case when the magnetic moments of the leads were aligned collinearly with respect to each other. In the following, we consider spin-dependent cotunneling transport in the case when the leads' magnetizations can form arbitrary magnetic configurations [106, 131]. Spin-polarized transport through quantum dots coupled to ferromagnetic electrodes with non-collinear magnetic moments is still not fully explored, although a couple of papers have already been reported [93, 94, 95, 132, 133, 134, 135, 136, 137].

5.1   Description of Model and Method

The system consists of a single-level quantum dot coupled through tunnel barriers to two external ferromagnetic leads, whose magnetizations are oriented arbitrarily in the plane of the structure. The dot is assumed to be deposited on a ferromagnetic substrate which strongly interacts with the dot and leads to spin-splitting of the dot level. The splitting is assumed to be larger than the level splitting due to exchange interaction between the dot and electrodes. The exchange interaction results from tunneling processes and is of the first order in the dot-lead coupling strength Γ [93, 94]. When neglecting the exchange coupling between the dot and leads, one may assume that the level splitting is constant, i.e., independent of applied voltage.

Coupling of the dot to ferromagnetic substrate is described by an effective molecular field $\mathbf{B}_s$, lying in the plane of the structure. Thus, the magnetic mo-
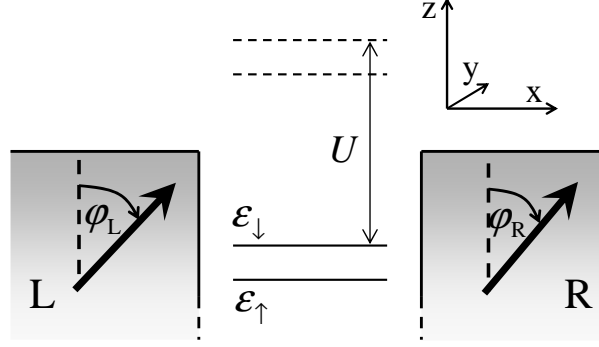
Figure 5.1: Schematic of a quantum dot coupled to ferromagnetic leads. The dot level is spin-split due an effective molecular field. Classical spin of the lead r ($r = \mathrm{L}, \mathrm{R}$) can form an arbitrary angle φ_r with the dot spin quantization axis (axis z), as indicated.

ments of the electrodes and the molecular field are all in a common plane. The effective molecular field determines the global quantization axis for electron spin on the dot (axis z antiparallel to the molecular field). In turn, the local quantization axis in the leads is determined by the corresponding local magnetization direction, and is parallel to the net spin of the lead (thus, being antiparallel to the local magnetic moment). Furthermore, it is assumed that the net spin of the left (right) lead forms an angle φ_L (φ_R) with the global quantization axis, as shown in Fig. 5.1. In previous chapters all the magnetic moments were collinear with respect to each other. In the case of noncollinear magnetic configurations, it is important to distinguish between different quantization directions. Thus, the majority (minority) spins in the local reference systems are labelled by $\sigma = +(-)$, while spin projection on the global quantization axis is denoted as $\sigma =\uparrow (\downarrow)$ for spin-up (spin-down) electrons.

Hamiltonian of the system has the general form, $H = H_\mathrm{L} + H_\mathrm{R} + H_\mathrm{D} + H_\mathrm{T}$, see Eq. (4.1). The lead Hamiltonians are diagonal in the respective local coordinate systems, $H_r = \sum_{\sigma=+,-} \sum_q \varepsilon_{rq\sigma} c_{rq\sigma}^\dagger c_{rq\sigma}$ (for $r = \mathrm{L}, \mathrm{R}$), with $\varepsilon_{rq\sigma}$ being the energy of a single electron with wavevector q and spin σ in the lead r, whereas $c_{rq\sigma}^\dagger$ and $c_{rq\sigma}$ denote the corresponding creation and annihilation operators.

The dot is described by the Anderson Hamiltonian, which in the global reference frame can be expressed as $H_\mathrm{D} = \sum_{\sigma=\uparrow,\downarrow} \varepsilon_\sigma d_\sigma^\dagger d_\sigma + U n_\uparrow n_\downarrow$, where ε_σ is the energy of an electron with spin σ, $\varepsilon_\sigma = \varepsilon \mp g\mu_B B_s$, and $d_\sigma^\dagger$ (d_σ) creates (annihilates) a spin-σ electron. Here, g is the Lande factor and ε is the dot level energy in the absence of magnetic electrodes and molecular field due to the substrate.

The tunnel Hamiltonian in the global reference system takes the form

$$H_{\mathrm{T}} = \sum_{r=\mathrm{L,R}} \sum_{q} [(t_{rq+} c_{rq+}^{\dagger} \cos \frac{\varphi_r}{2} - t_{rq-} c_{rq-}^{\dagger} \sin \frac{\varphi_r}{2}) d_{\uparrow}$$
$$+ (t_{rq+} c_{rq+}^{\dagger} \sin \frac{\varphi_r}{2} + t_{rq-} c_{rq-}^{\dagger} \cos \frac{\varphi_r}{2}) d_{\downarrow} + \mathrm{h.c.}] , \qquad (5.1)$$

with $t_{rq\sigma}$ denoting the tunnel matrix elements between the dot states and majority ($\sigma = +$) or minority ($\sigma = -$) electron states in the lead r when $\varphi_r = 0$.

As described in section 4.1, due to the coupling between dot and leads, the dot level acquires a finite width. When the magnetic moment of lead r and the molecular field acting on the dot are parallel, the corresponding contribution Γ_r^{σ} to the dot level width may be written as $\Gamma_r^{\sigma} = 2\pi |t_{r\sigma}|^2 \rho_{r\sigma}$, where $\rho_{r\sigma}$ is the spin-dependent density of states for the majority ($\sigma = +$) and minority ($\sigma = -$) electrons in the lead r. As previously, the coupling parameters are expressed in terms of spin polarization of the lead r, Eq. (1.4), as $\Gamma_r^{\pm} = \Gamma_r(1 \pm p_r)$, where $\Gamma_r = (\Gamma_r^+ + \Gamma_r^-)/2$. In the following, it is assumed that $\Gamma_{\mathrm{L}} = \Gamma_{\mathrm{R}} \equiv \Gamma/2$.

In the case of ferromagnetic leads, the coupling of the spin-up dot level is different from the coupling of the spin-down level, which is due to different densities of states for spin-majority and spin-minority electron bands in the leads. As pointed in the previous chapter, this may result in the splitting of the dot level [105, 138]. In this analysis it is assumed that the dot level splitting, $\Delta = \varepsilon_{\downarrow} - \varepsilon_{\uparrow}$, due to the molecular field is larger than the coupling parameters, $\Delta \gg \Gamma_r^{\pm}$. In other words, it is assumed that the exchange interaction between the dot and magnetic leads is much smaller than the Zeeman energy due to the molecular field and, thus, can be neglected. An electron residing on the dot has then either spin up or down. Thus, the corresponding density matrix in the global quantization system is diagonal in the spin space[1].

In that case, only the second-order processes (with respect to the tunneling Hamiltonian) have to be taken into account in the Coulomb blockade regime. When the above condition is not fulfilled, the exchange interaction cannot be ignored and therefore the first-order processes, which are responsible for the exchange coupling (and do not contribute to charge transport), have to be considered.

The electric current is calculated by means of the Averin-Nazarov approach, as described in section 4.3. In the case of noncollinearly magnetized leads, there are finite amplitudes for transitions between states that were forbidden in the case of collinearly magnetized leads. For the cotunneling rate for transition of electron from a spin-majority state in the lead r to a spin-minority state in the

---

[1]This follows directly from the general kinetic equation in the Liouville space for the density matrix elements, Eq. (4.10), derived within real-time diagrammatic technique [94].

lead r' one can write

$$\gamma_{rr'}^{+\Rightarrow-} = \frac{2\pi}{\hbar} \left| \sum_\nu \frac{\langle \Phi_r^+ | H_\mathrm{T} | \Phi_\nu \rangle \langle \Phi_\nu | H_\mathrm{T} | \Phi_{r'}^- \rangle}{\varepsilon_i - \varepsilon_\nu} \right|^2 \delta(\varepsilon_i - \varepsilon_f), \qquad (5.2)$$

where $|\Phi_r^+\rangle$ and $|\Phi_{r'}^-\rangle$ are the initial and final states of the system, whereas $|\Phi_\nu\rangle$ is a virtual state of the system. The corresponding energies are denoted as ε_i, ε_f, and ε_ν. The explicit expressions for cotunneling rates calculated within the second-order perturbation theory are given in appendix B.2.

In the following the two different situations are considered. The first one corresponds to an empty dot (due to particle-hole symmetry the results can be adapted to the case of doubly occupied dot). The second situation is the case of a singly occupied dot.

5.2   Cotunneling through Empty Dot

When the dot level is far above the Fermi energy of the leads, $\varepsilon_\sigma \gg k_\mathrm{B}T, \Gamma, |eV|$, there are no electrons on quantum dot and electric current can flow only due to non-spin-flip cotunneling processes. This situation corresponds to regime A, as illustrated in Fig. 4.4. Because of the particle-hole symmetry, a similar analysis can be directly performed for a doubly occupied dot (regime A'), when $\varepsilon_\sigma + U \ll 0$ and $|\varepsilon_\sigma + U| \gg k_\mathrm{B}T, \Gamma, |eV|$. As in the case of empty dot, the current can then flow only due to non-spin-flip cotunneling.

5.2.1   Theoretical Description

Electric current flowing from the left to right leads in the case of empty dot can be calculated from the following equation

$$I = -e\left(\gamma_{\mathrm{LR},0\Rightarrow0} - \gamma_{\mathrm{RL},0\Rightarrow0}\right), \qquad (5.3)$$

with $\gamma_{\mathrm{LR},0\Rightarrow0}$ being the non-spin-flip cotunneling rate for transition from the left to right leads, when the dot is in the state $|\chi = 0\rangle$. Similarly, $\gamma_{\mathrm{RL},0\Rightarrow0}$ is the non-spin-flip cotunneling rate for transition from the right to left electrodes. The explicit expressions for corresponding cotunneling rates are given in appendix B.2.1.

Having found all the cotunneling rates, one can calculate the electric current from Eq. (5.3), it is given by

$$\begin{aligned}
I = \frac{e\Gamma^2}{4h} \Big[& (1 + p_\mathrm{L}\cos\varphi_\mathrm{L})(1 + p_\mathrm{R}\cos\varphi_\mathrm{R})(\mathcal{B}_{2\mathrm{R}}^\uparrow - \mathcal{B}_{2\mathrm{L}}^\uparrow) \\
& + (1 - p_\mathrm{L}\cos\varphi_\mathrm{L})(1 - p_\mathrm{R}\cos\varphi_\mathrm{R})(\mathcal{B}_{2\mathrm{R}}^\downarrow - \mathcal{B}_{2\mathrm{L}}^\downarrow) \\
& + \frac{2p_\mathrm{L}p_\mathrm{R}\sin\varphi_\mathrm{L}\sin\varphi_\mathrm{R}}{\varepsilon_\downarrow - \varepsilon_\uparrow} \left(\mathcal{B}_{1\mathrm{R}}^\downarrow - \mathcal{B}_{1\mathrm{L}}^\downarrow - \mathcal{B}_{1\mathrm{R}}^\uparrow + \mathcal{B}_{1\mathrm{L}}^\uparrow \right) \Big],
\end{aligned} \qquad (5.4)$$

where the coefficients $\mathcal{B}_{1r}^{\sigma}$ and $\mathcal{B}_{2r}^{\sigma}$ are given by Eq. (B.9).

In the following, numerical results on electric current and the associated magnetoresistance are presented. In the case of systems with noncollinear magnetizations, the TMR effect is defined as

$$\text{TMR} = \frac{I_{\text{P}} - I(\varphi_{\text{L}}, \varphi_{\text{R}})}{I(\varphi_{\text{L}}, \varphi_{\text{R}})} \, , \qquad (5.5)$$

where $I(\varphi_{\text{L}}, \varphi_{\text{R}})$ is the current flowing in the noncollinear configuration described by the angles φ_{L} and φ_{R}, whereas I_{P} is the current flowing in the parallel configuration corresponding to $\varphi_{\text{L}} = \varphi_{\text{R}} = 0$.

5.2.2   Numerical Results

The formula (5.4) for electric current corresponds to the situation where the magnetic moments of the leads and the effective molecular field acting on the dot are oriented arbitrarily in the plane of the structure. Further numerical analysis is restricted, however, to the following two situations: (i) the magnetic moment of the left lead is parallel to the molecular field acting on the dot ($\varphi_{\text{L}} = 0$), while the magnetic moment of the right lead can have an arbitrary orientation, and (ii) the magnetic moments of both leads can rotate symmetrically in the opposite directions, $\varphi_{\text{R}} = -\varphi_{\text{L}}$. The case (i) corresponds to the situation when magnetic moment of one lead and magnetic moment of the layer producing the molecular field acting on the dot are fixed along the same direction. This can be achieved for instance by a common antiferromagnetic underlayer with strong exchange anisotropy at the antiferromagnet/ferromagnet interface. The situation (ii), in turn, corresponds to the case when both leads are equivalent and their magnetic moments can be rotated simultaneously by an external magnetic field.

In the first case, when $\varphi_{\text{L}} = 0$, the electric current is given by the formula

$$\begin{aligned}
I &= \frac{e\Gamma^2}{4h} \Big[(1 + p_{\text{L}})(1 + p_{\text{R}} \cos \varphi_{\text{R}})(\mathcal{B}_{2\text{R}}^{\uparrow} - \mathcal{B}_{2\text{L}}^{\uparrow}) \\
&\quad + (1 - p_{\text{L}})(1 - p_{\text{R}} \cos \varphi_{\text{R}})(\mathcal{B}_{2\text{R}}^{\downarrow} - \mathcal{B}_{2\text{L}}^{\downarrow}) \Big] \, , \qquad (5.6)
\end{aligned}$$

which follows directly from Eq. (5.4). In Figure 5.2 we show the current (a,c) flowing through the system and the corresponding TMR (b,d) as a function of the bias voltage for several values of angle φ_{R}, and as a function of the angle φ_{R} for several values of the bias voltage. It can be seen that the current decreases and TMR increases as the angle φ_{R} varies from $\varphi_{\text{R}} = 0$ to $\varphi_{\text{R}} = \pi$, which corresponds to the transition from parallel to antiparallel magnetic configurations. Parts (c) and (d) show explicitly this angular dependence. Both the current and TMR vary monotonically with φ_{R} (for $0 \leq \varphi_{\text{R}} \leq \pi$) and electric current reaches minimum, while TMR maximum, at $\varphi_{\text{R}} = \pi$, i.e., in the antiparallel configuration. Such
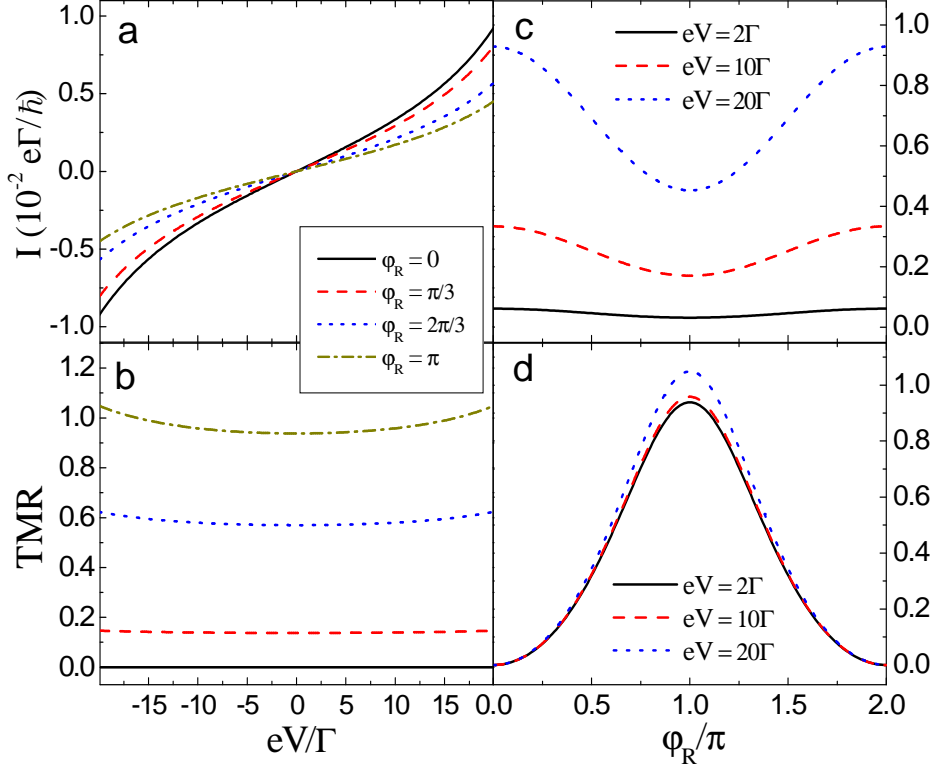
Figure 5.2: The cotunneling current (a,c) and the TMR effect (b,d) as a function of the bias voltage (left column) and the angle φ_R (right column). The parameters assumed for calculations are: $k_B T = \Gamma$, $\varepsilon_\uparrow = 18\Gamma$, $\varepsilon_\downarrow = 22\Gamma$, $p_L = p_R = 0.5$, and $\varphi_L = 0$.

behavior is typical of normal spin valves and results from spin asymmetry in tunneling processes. It is also worth noting that TMR is only weakly dependent on the bias voltage, as shown in Fig. 5.2b.

Assuming the same spin polarization of the leads, $p_L = p_R = p$, one can find the following explicit formula for TMR in the case of empty dot in the zero bias and zero temperature limits

$$\text{TMR} = \frac{(1 - \cos\varphi_R)p\left[(1+p)\varepsilon_\downarrow^2 - (1-p)\varepsilon_\uparrow^2\right]}{(1+p)(1+p\cos\varphi_R)\varepsilon_\downarrow^2 + (1-p)(1-p\cos\varphi_R)\varepsilon_\uparrow^2}. \qquad (5.7)$$

The above formula describes the angular variation of TMR and shows explicitly that TMR reaches maximum for $\varphi = \pi$. This maximum value is given by the expression

$$\text{TMR}_{\text{max}} = \frac{2p}{1 - p^2}\left[p + \frac{\varepsilon_\downarrow^2 - \varepsilon_\uparrow^2}{\varepsilon_\uparrow^2 + \varepsilon_\downarrow^2}\right]. \qquad (5.8)$$
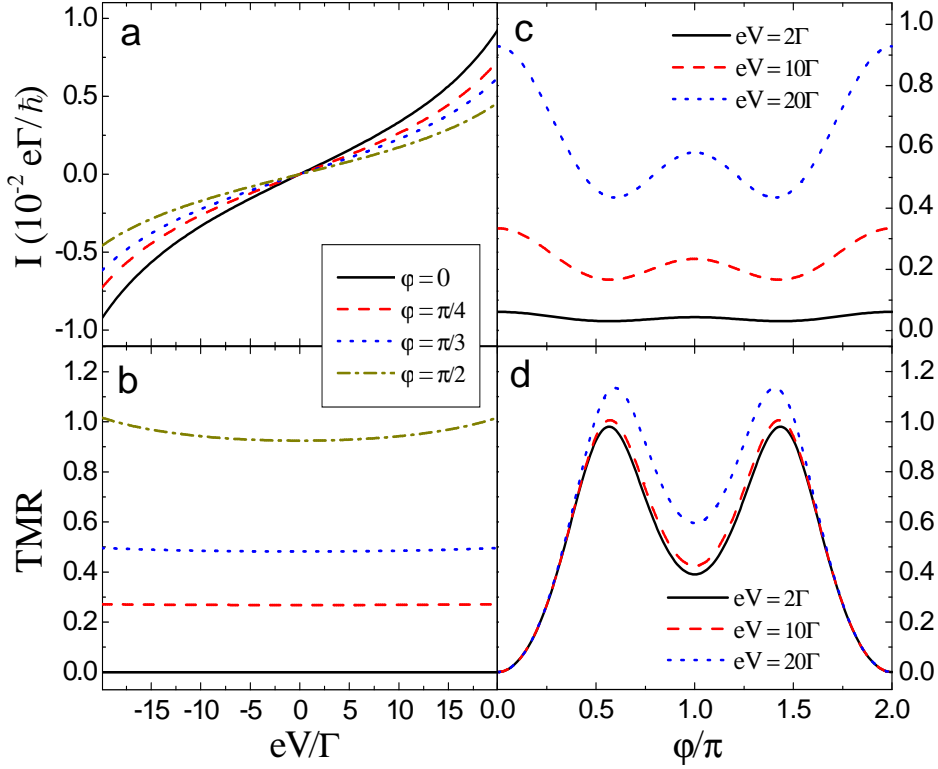
Figure 5.3: The cotunneling current (a,c) and the TMR effect (b,d) as a function of the bias voltage (left column) and as a function of $\varphi = \varphi_R = -\varphi_L$ (right column). The other parameters are the same as in Fig. 5.2.

The first term in the bracket of the above equation gives the Jullière's value of TMR, see Eq. (1.5), whereas the second term describes enhancement of the tunnel magnetoresistance due to the level splitting. Such an enhancement of TMR may be of some interest from the application point of view. Furthermore, it is worth noting that by changing the sign of the level splitting from Δ to $-\Delta$ (by changing the direction of the molecular field), one can either enhance or suppress the TMR effect, as can also be seen in Figs. 4.15 and 4.16.

Consider now the situation (ii), when $\varphi_R = -\varphi_L \equiv \varphi$. The magnetic moment of the left lead rotates now together with the magnetic moment of the right lead, but in the opposite direction. The electric current is then given by Eq. (5.4) with $\varphi_R = \varphi$ and $\varphi_L = -\varphi$. The corresponding bias and angular dependence of the cotunneling current and TMR is displayed in Fig. 5.3.

It is interesting to note that the angular dependence of electric current and TMR differs now from that found above for the situation (i). In order to understand this difference one should take into account the fact that $\varphi_R = \varphi_L = 0$ corresponds to the parallel configuration, whereas the situation with $\varphi_R = -\varphi_L = \pi/2$

corresponds to the antiparallel configuration with magnetic moments oriented perpendicularly to the molecular field acting on the dot. It is also worth noting that electric current reaches minimum and TMR maximum not exactly at $\varphi_R = -\varphi_L = \pi/2$, but for the configuration which is close to the antiparallel one. Moreover, position of these minima and maxima depends on the bias voltage, as shown in Fig. 5.3c and d. In turn, the case $\varphi_R = -\varphi_L = \pi$ corresponds again to the parallel configuration, but with the magnetic moments of the electrodes being antiparallel to the molecular field. This leads to a local maximum of electric current (minimum in TMR) at $\varphi_R = -\varphi_L = \pi$. It is interesting to note that the two parallel configurations (aligned and anti-aligned with respect to the molecular field) are not equivalent, and consequently the corresponding currents and also TMR values are not equal.

When assuming equal spin polarizations of the leads and low bias and temperature limits, one finds that the TMR effect at $\varphi_R = -\varphi_L = \pi$ (which corresponds to its local minimum) is given by

$$\text{TMR}_{\min} = \frac{4p(\varepsilon_\downarrow^2 - \varepsilon_\uparrow^2)}{(1+p)^2\varepsilon_\uparrow^2 + (1-p)^2\varepsilon_\downarrow^2} \,. \tag{5.9}$$

In the same limit and for a nonzero spin polarization p, one can show that the two maxima of TMR appear at $\varphi = \arccos\phi$ and $\varphi = 2\pi - \arccos\phi$, with $\phi = -\Delta/p(\varepsilon_\uparrow + \varepsilon_\downarrow)$. In the limit of $p = 0$ TMR vanishes by definition. On the other hand, in the case when $|\Delta| < p(\varepsilon_\uparrow + \varepsilon_\downarrow)$, the maxima appear approximately at $\varphi_R = -\varphi_L = \pi/2$ and $\varphi_R = -\varphi_L = 3\pi/2$. The corresponding TMR value is then equal

$$\text{TMR}_{\max} = \frac{p\left[(2+p)\varepsilon_\downarrow - (2-p)\varepsilon_\uparrow\right](\varepsilon_\uparrow + \varepsilon_\downarrow)}{\varepsilon_\uparrow^2 + \varepsilon_\downarrow^2 - 2p^2\varepsilon_\uparrow\varepsilon_\downarrow} \,. \tag{5.10}$$

5.3   Cotunneling through Singly-Occupied Dot

By applying an external gate voltage to the dot, one can tune position of the level energy and this way also the dot occupation. When ε_σ is negative and $\varepsilon_\sigma + U$ positive, the dot is singly occupied at equilibrium for $\Gamma, k_B T \ll |\varepsilon_\sigma|, |\varepsilon_\sigma + U|$, and the system is in the Coulomb blockade regime, see regime B in Fig. 4.4. As before, the two situations (i) and (ii) defined in the previous section are considered.

5.3.1   Theoretical Description

In the case studied in the preceding section the dot was empty, and the second-order current was mediated only by non-spin-flip cotunneling processes. When the dot is singly occupied, the cotunneling current can also flow due to spin-flip cotunneling, in which the electrons tunneling to and off the dot have opposite
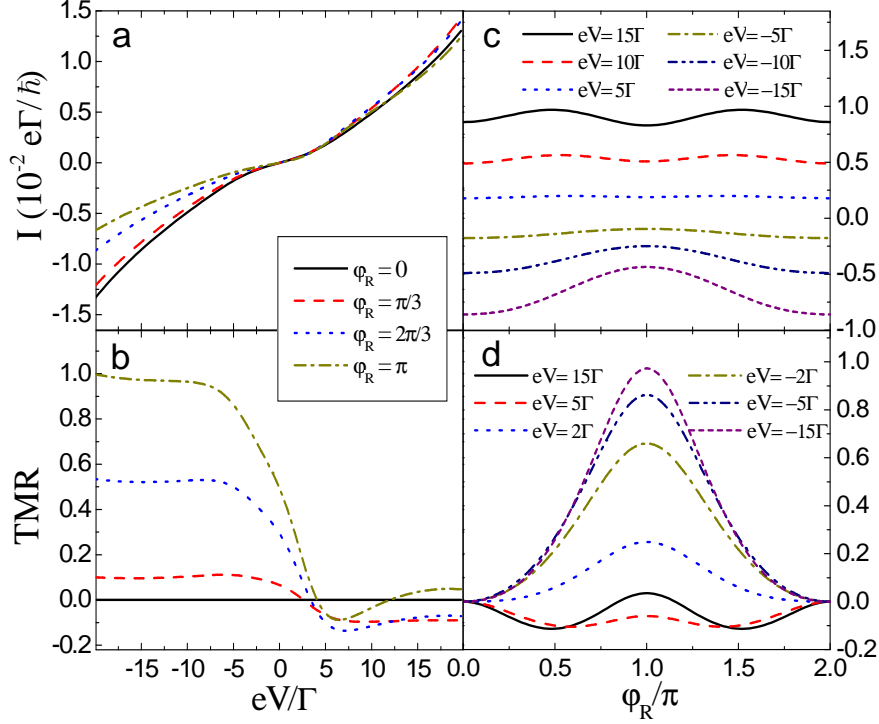
Figure 5.4: The cotunneling current (a,c) and the TMR effect (b,d) as a function of the bias voltage (left column) and the angle φ_R (the right column). The parameters assumed for calculations are: $k_B T = \Gamma$, $\varepsilon_\uparrow = -22\Gamma$, $\varepsilon_\downarrow = -18\Gamma$, $U = 40\Gamma$, $p_L = p_R = 0.5$, $\varphi_L = 0$.

spin orientations (and consequently also different energies due to the level spin-splitting), as discussed in previous chapter. These spin-flip cotunneling processes determine the occupation numbers of the dot.

The probabilities $P_\uparrow$ and $P_\downarrow$, that the dot is occupied either by a spin-up or spin-down electron, can be calculated from the master equation given by Eq. (4.28). The corresponding spin-flip and non-spin-flip second-order transition rates are listed in appendix B.2.2. Having calculated the cotunneling rates and the occupation probabilities, one can determine the current flowing from the left to right leads from Eq. (4.30).

5.3.2 Numerical Results

In the case when the magnetic moment of the left electrode is fixed ($\varphi_L = 0$) and the magnetic moment of the right lead is free to rotate, situation (i), the angular and bias dependence of electric current and the TMR effect is shown in Fig. 5.4. Except for the parallel configuration, the current-voltage curves are now asymmetric with respect to the bias reversal, see Fig. 5.4a. This asymmetry
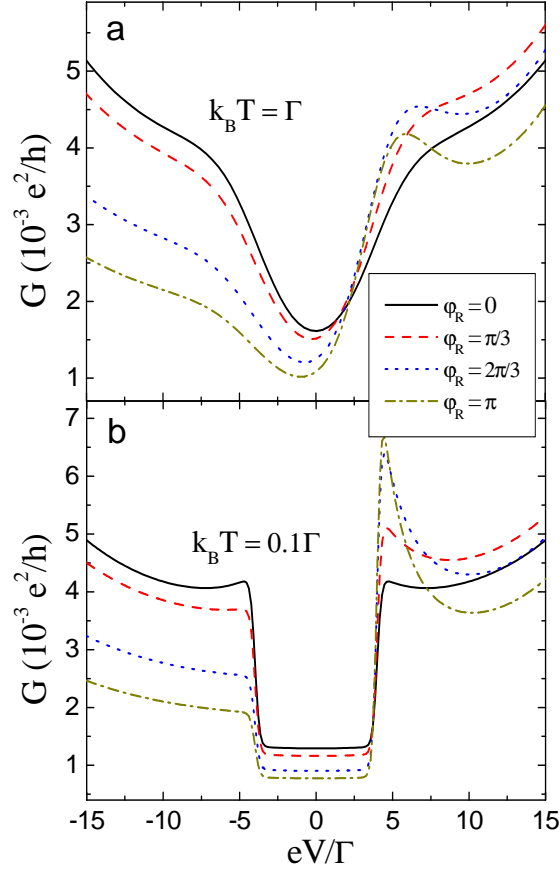
Figure 5.5:   Differential conductance corresponding to the situation shown in Fig. 5.4a, calculated for two different temperatures: (a) $k_BT = \Gamma$ and (b) $k_BT = 0.1\Gamma$.

also leads to related asymmetric behavior of TMR, as illustrated in Fig. 5.4b. Moreover, for positive bias voltage, the TMR effect can change sign and become negative in a certain range of the bias and angle values. Such an asymmetry in transport characteristics with respect to the bias reversal is of some importance for applications, particularly when the current is significantly suppressed for one bias polarization (diode behavior).

In order to account for the bias asymmetry, let us consider only the antiparallel configuration. One should then realize that owing to the level splitting, $\varepsilon_\uparrow < \varepsilon_\downarrow$, the single-barrier spin-flip cotunneling processes can occur only when the dot is occupied by a spin-down electron, see also subsection 4.5.3. As a consequence, the current can flow due to the double-barrier cotunneling processes assisted by the single-barrier processes. The fastest double-barrier cotunneling can occur when the dot is occupied by a spin-down electron for negative bias and by a spin-up electron for positive bias, thus, leading to respective suppression or
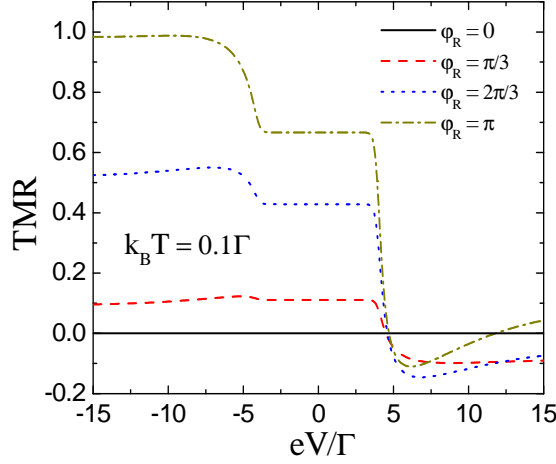
Figure 5.6: The TMR effect as a function of the bias voltage for $k_{\mathrm{B}}T = 0.1\Gamma$ and for different angles φ_{R}. The other parameters are the same as in Fig. 5.4.

enhancement of the current, as shown in Fig. 5.4a. The above described mechanism of the asymmetry with respect to the bias reversal does not hold when magnetic moments of the two leads are parallel, consequently, the corresponding current-voltage curve is symmetrical.

In order to demonstrate the above described asymmetry more clearly, the corresponding differential conductance is displayed in Fig. 5.5a. The asymmetry for $\varphi_{\mathrm{R}} > 0$ is clearly evident. Besides the asymmetry, an additional interesting feature of the differential conductance is also visible, namely, a characteristic plateau in the small bias voltage regime. This plateau is a consequence of the suppression of spin-flip double-barrier cotunneling events when $|eV| < |\Delta|$. For $|eV| > |\Delta|$, the spin-flip cotunneling processes are allowed, leading to an enhanced conductance, as discussed in previous chapter. The asymmetry and zero-bias anomaly are even more evident at lower temperature, as shown in Fig. 5.5b.

Furthermore, the effect of suppression of spin-flip cotunneling can be also visible in the TMR effect – it displays a plateau for $|eV| < |\Delta|$, as illustrated in Fig. 5.6. For the angular dependence of this plateau, we have found in the low temperature limit

$$\mathrm{TMR} = \frac{2p^2 \sin^2 \frac{\varphi_{\mathrm{R}}}{2}}{1 + p^2 \cos \varphi_{\mathrm{R}}} , \tag{5.11}$$

which for $\varphi_{\mathrm{R}} = \pi$ gives the Jullière's value. Equation (5.11) shows the explicit dependence of TMR in the linear response on the angle φ_{R}.

The angular variation of electric current and TMR reveals further new features. For negative bias there is a maximum of absolute value of electric current in the parallel configuration and a minimum in the antiparallel configuration. For positive bias, however, the electric current has a maximum for noncollinear
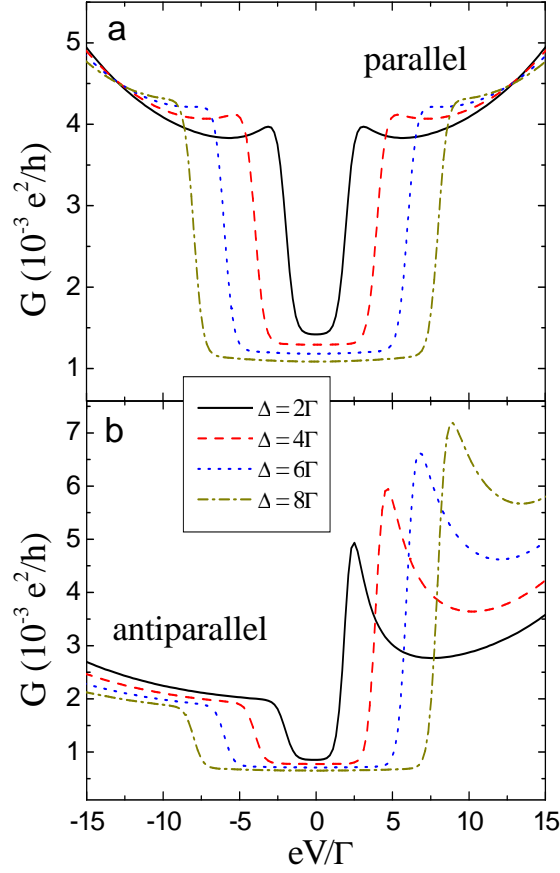
Figure 5.7: Differential conductance for different values of the level splitting for the parallel (a) and antiparallel (b) magnetic configurations. The parameters are: $k_BT = 0.2\Gamma$, $\varepsilon_\uparrow = \varepsilon - \Delta/2$, $\varepsilon_\downarrow = \varepsilon + \Delta/2$, $\varepsilon = -20\Gamma$, $U = 40\Gamma$, and $p_L = p_R = 0.5$.

configuration, as displayed in Fig. 5.4c. The nonmonotonic variation of electric current with the angle φ_R leads to the corresponding nonmonotonic variation of TMR, shown in Fig. 5.4d. Furthermore, TMR may now become negative, as already mentioned before.

Numerical results presented so far have been shown for a single value of the level splitting, $\Delta = 4\Gamma$. From the experimental point of view, variation of the conductance as a function of the level splitting (induced for instance by a strong external magnetic field), allows one to determine some interesting transport and spectroscopic characteristics. Therefore, the differential conductance for different splitting of the dot level in the parallel and antiparallel configurations is shown in Fig. 5.7. By measuring width of the conductance dip, one can determine for instance the spectroscopic g-factor [98].

In the case of a deep Coulomb blockade regime and $|eV|, k_BT \ll |\Delta|$, one can derive an approximate formula for the plateau in differential conductance due to

the suppression of spin-flip cotunneling. Writing $\varepsilon_\uparrow = \varepsilon - \Delta/2$ and $\varepsilon_\downarrow = \varepsilon + \Delta/2$, one finds then the following expression

$$
\begin{aligned}
G \;=\; \frac{\Gamma^2 e^2}{4h} &\left[\frac{(1 + p_{\mathrm{L}}\cos\varphi_{\mathrm{L}})(1 + p_{\mathrm{R}}\cos\varphi_{\mathrm{R}})}{(\varepsilon - \Delta/2)^2} \right.\\
&+ \frac{(1 - p_{\mathrm{L}}\cos\varphi_{\mathrm{L}})(1 - p_{\mathrm{R}}\cos\varphi_{\mathrm{R}})}{(\varepsilon + U + \Delta/2)^2} \\
&\left. - \frac{8 p_{\mathrm{L}} p_{\mathrm{R}} \sin\varphi_{\mathrm{L}} \sin\varphi_{\mathrm{R}}}{(\varepsilon - \Delta/2)(\varepsilon + U + \Delta/2)} \right] .
\end{aligned}
\tag{5.12}
$$

The above equation is valid for an arbitrary magnetic configuration and is a generalization of Eqs. (4.48) and (4.49). Formula (5.12) approximates the plateaus shown in Fig. 5.5. When assuming $\varphi_{\mathrm{L}} = \varphi_{\mathrm{R}} = 0$ (which corresponds to the parallel configuration), Eq. (5.12) simplifies to the following form

$$
G^{\mathrm{P}} = \frac{\Gamma^2 e^2}{4h} \left[\frac{(1 + p_{\mathrm{L}})(1 + p_{\mathrm{R}})}{(\varepsilon - \Delta/2)^2} + \frac{(1 - p_{\mathrm{L}})(1 - p_{\mathrm{R}})}{(\varepsilon + U + \Delta/2)^2} \right] ,
\tag{5.13}
$$

whereas for the antiparallel alignment ($\varphi_{\mathrm{L}} = 0$, $\varphi_{\mathrm{R}} = \pi$) it becomes

$$
G^{\mathrm{AP}} = \frac{\Gamma^2 e^2}{4h} \left[\frac{(1 + p_{\mathrm{L}})(1 - p_{\mathrm{R}})}{(\varepsilon - \Delta/2)^2} + \frac{(1 - p_{\mathrm{L}})(1 + p_{\mathrm{R}})}{(\varepsilon + U + \Delta/2)^2} \right] .
\tag{5.14}
$$

The above two expressions describe the plateaus in differential conductance shown in Fig. 5.7. It is also worth noting that generally $G^{\mathrm{P}} > G^{\mathrm{AP}}$. Furthermore, both G^{P} and G^{AP} vary monotonically with spin polarization of the leads – in the case of nonmagnetic leads ($p_{\mathrm{L}} = p_{\mathrm{R}} = 0$) $G^{\mathrm{P}} = G^{\mathrm{AP}}$, whereas for $p_{\mathrm{L}} = p_{\mathrm{R}} = 1$ (which corresponds to half-metallic leads) G^{P} is maximal and $G^{\mathrm{AP}} = 0$.

Transport characteristics in the second situation, i.e., for the case when $\varphi_{\mathrm{R}} = -\varphi_{\mathrm{L}} = \varphi$, are displayed in Fig. 5.8. One can note that the current is now almost independent of the magnetic configuration, see Fig. 5.8a and c. Nevertheless, the angular dependence of the current becomes more visible in the corresponding differential conductance, plotted in Fig. 5.9a for different values of the angle φ, and also in Fig. 5.9b for the same situation, but for much lower temperature. The cotunneling gap due to suppression of the spin-flip processes is also clearly visible. The plateau in differential conductance for $|eV| \ll k_{\mathrm{B}}T, |\Delta|$ is described by Eq. (5.12). Since the system is now symmetric, the current-voltage curves (and consequently also the differential conductance) are symmetric with respect to the bias reversal.

The TMR effect reaches maximum in the zero-bias limit, $V = 0$, as shown in Fig. 5.8b. At low temperatures this maximum develops into a broad plateau, whose width is conditioned by the onset of sequential tunneling. This situation is illustrated in Fig. 5.10, which presents the bias voltage dependence of the TMR
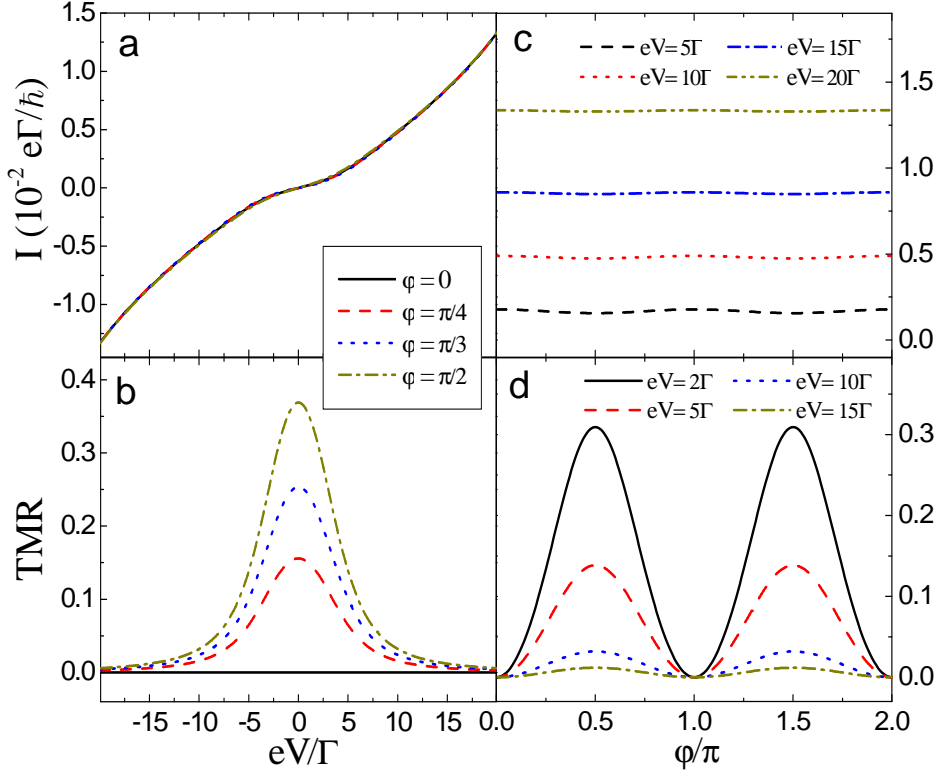
Figure 5.8: The cotunneling current (a,c) and the TMR effect (b,d) as a function of the bias voltage (left column) and $\varphi = \varphi_R = -\varphi_L$ (right column). The other parameters are the same as in Fig. 5.4.

effect for several values of angle φ. In the low temperature limit the plateau in TMR at low bias voltage can be approximated by the following formula

$$\text{TMR} = \frac{[1 - \cos(\varphi_L - \varphi_R)]\, p_L p_R}{1 + p_L p_R \cos(\varphi_L - \varphi_R)} \ . \tag{5.15}$$

The above expression describes the linear response TMR for arbitrary angles φ_L and φ_R, and presents, thereby, a generalization of Eq. (5.11). For $\varphi_R = -\varphi_L = \pi/2$, TMR is given by the Jullière's value. This is due to the fact that for $|\Delta| \gg k_B T, |eV|$ the current is mediated only by non-spin-flip cotunneling, which is fully coherent, thus, leading to the TMR of a single ferromagnetic tunnel junction, see Eq. (1.5).

The angular variation of TMR, shown in Fig. 5.8d, reveals two maxima (and also two minima), similarly as it was in the case of empty dot, but now the maxima appear strictly for $\varphi = \pi/2$ and $\varphi = 3\pi/2$. On the other hand, one minimum of TMR occurs at $\varphi_R = \varphi_L = 0$, where TMR vanishes by definition. Tunnel magnetoresistance vanishes also in the second parallel configuration, when
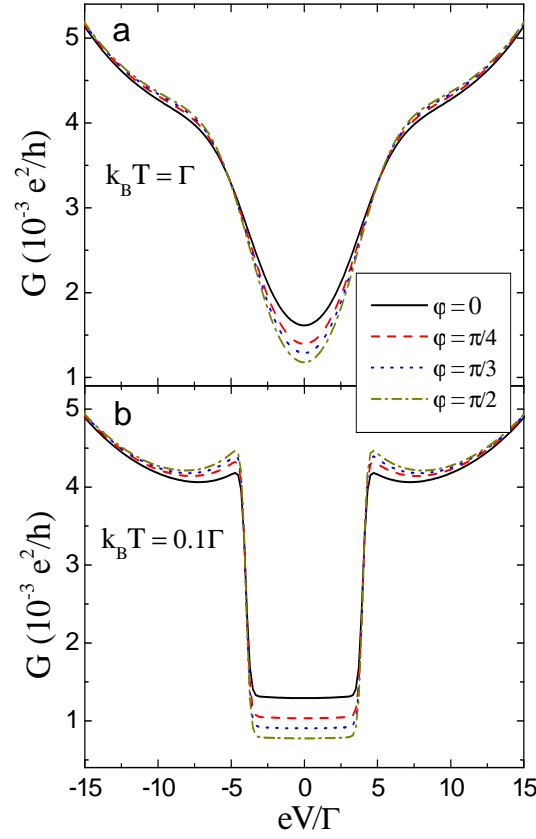
Figure 5.9: Differential conductance for the situation shown in Fig. 5.8a, calculated for two indicated temperatures: (a) $k_B T = \Gamma$ and (b) $k_B T = 0.1\Gamma$.
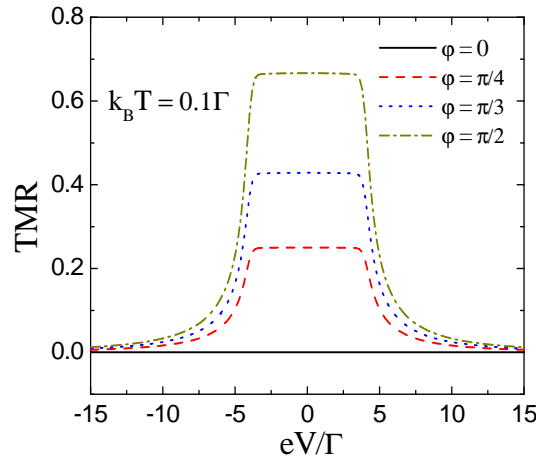

Figure 5.10: The TMR effect as a function of the bias voltage for $k_B T = 0.1\Gamma$ and for different angles $\varphi = \varphi_R = -\varphi_L$. The other parameters are the same as in Fig. 5.4.
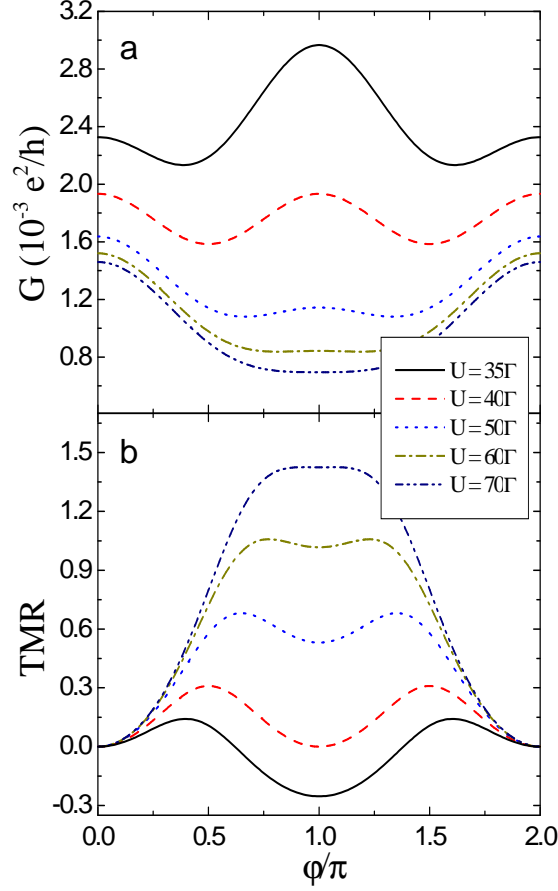
Figure 5.11: The angular dependence of the differential conductance and tunnel magnetoresistance for several values of the Coulomb interaction parameter U at the bias voltage $eV = 2\Gamma$. The other parameters are the same as in Fig. 5.8.

both magnetizations are antiparallel to the molecular field ($\varphi_{\mathrm{R}} = -\varphi_{\mathrm{L}} = \pi$). This is due to the fact that the parameters assumed for numerical calculations correspond to a symmetric Anderson model, i.e., $U = -\varepsilon_\uparrow - \varepsilon_\downarrow$. When the system becomes asymmetric, e.g., when U increases (decreases) while the other parameters are constant, the minimum in TMR at $\varphi = \pi$ is shifted down (up) and, when $U \gg -\varepsilon_\uparrow - \varepsilon_\downarrow$, TMR has only one maximum at $\varphi = \pi$, as shown in Fig. 5.11b. On the other hand, if $U < -\varepsilon_\uparrow - \varepsilon_\downarrow$, the minimum in tunnel magnetoresistance at $\varphi = \pi$ becomes negative, which is illustrated in Fig. 5.11b for $U = 35\Gamma$. Thus, by changing the model parameters one may significantly enhance or reduce the TMR effect.

In the limit of $|eV|, k_{\mathrm{B}}T \ll |\Delta|$ and for $p_{\mathrm{L}} = p_{\mathrm{R}} = p$, the TMR ratio for

$\varphi_\mathrm{R} = -\varphi_\mathrm{L} = \pi$ can be expressed as

$$\mathrm{TMR} = \frac{4p(2\varepsilon + U)(U + \Delta)}{(1 - p)^2(\varepsilon + U + \Delta/2)^2 + (1 + p)^2(\varepsilon - \Delta/2)^2} \, . \qquad (5.16)$$

From the above expression it can be seen that the sign of TMR at $\varphi = \pi$ depends on the ratio ε/U. If $U = -2\varepsilon$, TMR vanishes, whereas for $U > -2\varepsilon$ TMR is positive, while for $U < -2\varepsilon$ TMR becomes negative. In the case of $U \gg -2\varepsilon$, the TMR effect is given by $4p/(1 - p)^2$.

The corresponding angular dependence of the differential conductance is shown in Fig. 5.11a. Now, the maximum in the conductance at $\varphi = \pi$ for a symmetric model changes into a minimum for $U \gg -\varepsilon_\uparrow - \varepsilon_\downarrow$.

In this chapter the cotunneling current and associated tunnel magnetoresistance through a single-level quantum dot coupled to two external ferromagnetic leads with noncollinear magnetizations was considered both numerically and analytically. The dot level was assumed to be spin-split due to an effective molecular field originating from a magnetic substrate on which the dot is deposited, and the splitting was assumed to be larger than the characteristic parameter Γ (level width) describing the dot-lead interaction. Several interesting features in the angular and bias dependence of transport characteristics were found. In the case of empty dot, TMR was found to be roughly independent of the bias voltage, but strongly dependent on the angle between magnetic moments. When magnetic moments of both leads rotate in opposite directions, both electric current and TMR vary nonmonotonously with increasing angle between the magnetic moments of the leads, and maximum of TMR may occur at a noncollinear configuration. For a singly occupied dot and for the case (i) ($\varphi_\mathrm{L} = 0$), strong asymmetry in electric current and TMR with respect to the bias reversal was found, which disappears for the case (ii) ($\varphi_\mathrm{R} = -\varphi_\mathrm{L}$). This diode-like behavior of the current-voltage characteristics may be of some interest from the application point of view. Moreover, the asymmetry in current-voltage curves leads to associated asymmetry in TMR which may become even negative for one bias polarization. An important and interesting result is also an enhancement of TMR due to the dot level splitting. Finally, the evolution of the cotunneling gap with the splitting of the dot level and magnetic configuration of the system was also demonstrated numerically and analytically.

Chapter 6

Conclusions

In this dissertation the spin-dependent electronic transport in magnetic nanostructures with Coulomb blockade was considered. Several novel features and effects were predicted for the case of ferromagnetic single-electron devices as well as quantum dots coupled to ferromagnetic leads both in the sequential tunneling and cotunneling regimes. The thesis was divided into two parts: the first part concerned the spin-polarized transport in single-electron devices, including ferromagnetic single-electron transistors and double-island devices, whereas in the second part transport through quantum dots coupled to ferromagnetic leads was analyzed.

The introduction and the review of basic phenomena and concepts in single-electron tunneling was presented in chapter 1. In chapter 2 the results on spin-polarized transport in ferromagnetic single-electron transistors in both the presence and absence of nonequilibrium spin accumulation on the island were presented. In particular, it was shown that in the case of transistors with nonmagnetic islands the spin accumulation is crucial for observation of a nonzero TMR effect.

The transport properties of ferromagnetic double-island devices were considered in chapter 3. In section 3.2 the spin-polarized transport in a device built of two ferromagnetic islands in the absence of spin accumulation was analyzed. It was shown that such systems can serve as magnetoresistive elements with the gate-controlled magnitude of tunnel magnetoresistance. The results in the presence of spin accumulation on the islands for various configurations of the system were presented in section 3.3. In particular, it was demonstrated that spin accumulation induced on the islands may considerably influence the dependence of both the conductance and the TMR effect. First of all, it was shown that in the case of nonmagnetic islands a finite TMR occurs due to spin accumulation. Furthermore, the TMR oscillates between positive and negative values as a function of the bias voltage. In turn, if the islands are ferromagnetic, spin accumulation may lead to negative differential conductance. This nontrivial behavior of differential conductance strongly depends on the parameters of the system and may

occur in both the parallel and antiparallel magnetic configurations. In addition, the dependence of the above mentioned features on the spin relaxation time was also analyzed. It was shown that when the relaxation time is shortened, both the negative tunnel magnetoresistance and negative differential conductance become suppressed and eventually vanish in the limit of fast spin relaxation. Moreover, in section 3.4 it was demonstrated that ferromagnetic double-island devices can be used for pumping of single electrons with a given spin orientation.

Transport through quantum dots coupled to ferromagnetic leads in the first-order and second-order tunneling regimes was considered in the second part of the thesis. In chapter 4 the case of quantum dots coupled to ferromagnetic leads with collinear alignment of magnetic moments was analyzed. The model of the system was described in section 4.1, whereas the real-time diagrammatic technique used in calculations was presented in section 4.2. Within this technique it was possible to calculate the current through the system in the full range of parameters. In the deep Coulomb blockade regime where the second-processes dominate, however, transport can be alternatively calculated within the Averin-Nazarov approach. This method was outlined in section 4.3.

The relevant numerical results on conductance and the TMR effect were presented and discussed in section 4.4. In particular, a parity effect was found in the TMR in the linear response regime. More precisely, it was shown that TMR reaches the Jullière's value for Coulomb blockade valleys with even number of electrons on the dot, whereas in the case of an odd dot electron number, the TMR is much reduced as compared to the Jullière's TMR. In the nonlinear response regime, in turn, TMR exhibits a minimum in the zero-bias limit. This minimum is a consequence of a maximum in differential conductance in the antiparallel configuration of the leads' magnetizations. The main properties and mechanism of this zero-bias anomaly were the subject of section 4.5. It was shown that the anomaly results from the interplay of the single-barrier and double-barrier cotunneling processes. The zero-bias peak exists in the antiparallel configuration and vanishes when the leads' magnetizations are parallel. Moreover, the influence of external magnetic filed was also analyzed. In the case of spin-split dot level the spin-flip cotunneling processes are suppressed for $|eV| < |\Delta|$ and the current is mediated only by non-spin-flip cotunneling. This effectively leads to a deep plateau in differential conductance which is present in both magnetic configurations.

The influence of the intrinsic spin relaxation processes in the dot on transport characteristics in the Coulomb blockade valley with odd number of electrons on the dot was considered in section 4.6. First, the case of symmetric systems was analyzed. It was shown that both the zero-bias anomaly in differential conductance and the minimum in TMR at low bias voltage become suppressed in the limit of fast spin relaxation on the dot. Furthermore, the TMR effect was found to be negative in this limit. In the case of quantum dots asymmetrically coupled to the leads the system exhibits a diode-like behavior. Moreover, it was shown

that the zero-bias anomaly found previously in differential conductance may also exist in systems with only one ferromagnetic electrode, while the other one is nonmagnetic. In the limit of fast spin relaxation on the dot, however, both the asymmetry with respect to the bias reversal and the zero-bias peak disappear.

Transport through quantum dots coupled to ferromagnetic leads with non-collinear alignment of magnetizations was considered in chapter 5. The method and model were described in section 5.1. It was assumed that the dot level was spin-split due to the interaction with molecular field exerted by ferromagnetic background. The current through the system was calculated with the aid of the Averin-Nazarov approach. The numerical results in the case of empty dot were presented in section 5.2. In this situation the TMR effect was found to be strongly dependent on the angle between the leads' magnetizations. The angular dependence of conductance and the TMR in the case of singly-occupied dot was analyzed in section 5.3. In particular, the dependence of the asymmetry with respect to the bias voltage on the relative angle between leads' magnetic moments was presented. Furthermore, it was shown that the TMR effect may be enhanced due to the spin splitting of the dot level. In addition, the impact of the system magnetic configuration and splitting of the dot level on the gap in differential conductance due to the suppression of spin-flip cotunneling was also analyzed.

Streszczenie

Niniejsza rozprawa przedstawia teoretyczną analizę spinowo spolaryzowanego transportu w magnetycznych nanostrukturach z blokadą kulombowską. Praca składa się z dwóch części: pierwsza dotyczy transportu sekwencyjnego w tranzystorach jednoelektronowych i układach zbudowanych z dwóch nanoskopowych wysp, natomiast w części drugiej rozpatrzono problem tunelowania sekwencyjnego oraz kotunelowania przez kropki kwantowe sprzężone z ferromagnetycznymi elektrodami. Otrzymane charakterystyki transportowe zawierają szereg nowych, interesujących rezultatów, wynikających z połączenia efektów związanych z dyskretnością ładunku elektrycznego oraz ferromagnetyzmu.

Rozdział 1 zawiera ogólne wprowadzenie do problematyki tunelowania przez nanostruktury. Przedstawiono w nim podstawowe efekty charakterystyczne dla układów analizowanych w niniejszej rozprawie, a związane z dyskretnym ładowaniem pojedynczymi elektronami. Efekty ładowania występują wtedy, gdy energia związana z dodaniem do nanostruktury jednego elektronu jest znacznie większa od energii termicznej. Ponadto, w rozdziale 1 opisany został model Jullière'a tunelowego magnetooporu dla pojedynczego złącza magnetycznego.

W rozdziale 2 przedstawiono wyniki dotyczące sekwencyjnego transportu w ferromagnetycznych tranzystorach jednoelektronowych. Analizę przeprowadzono w oparciu o metodę równania typu "master", a poszczególne częstotliwości tunelowania obliczono ze złotej reguły Fermiego. Najpierw rozpatrzony został układ zbudowany z magnetycznych elektrod i magnetycznej wyspy. Otrzymane charakterystyki prądowo-napięciowe ukazują charakterystyczną schodkową zależność prądu od napięcia transportowego, tzw. schodki kulombowskie, oraz oscylacje kulombowskie prądu w funkcji napięcia bramkującego. Ponadto, pokazano, iż prąd tunelowy płynący przez układ zależy od wzajemnego ustawienia momentów magnetycznych elektrod: w konfiguracji równoległej prąd jest większy niż w konfiguracji antyrównoległej. Fakt ten prowadzi do pojawienia się niezerowego efektu tunelowego magnetooporu, który wykazuje oscylacyjny charakter w funkcji napięcia transportowego. Otrzymane wyniki teoretyczne są zgodne z danymi eksperymentalnymi. Kolejnym układem przeanalizowanym w rozdziale 2 jest tranzystor jednoelektronowy zbudowany z magnetycznych elektrod oraz niemagnetycznej wyspy. Tego typu układy mogą wykazywać efekt tunelowego magnetooporu tylko wtedy, gdy czas spinowej relaksacji na wyspie jest dłuższy od czasu

pomiędzy kolejnymi aktami tunelowania. Jeżeli spełniony jest powyższy warunek, na wyspie indukuje się nierównowagowy moment magnetyczny. Spinowa akumulacja z kolei prowadzi do wystąpienia tunelowego magnetooporu, który oscyluje w funkcji napięcia transportowego. Natomiast w granicy krótkiego czasu spinowej relaksacji zarówno spinowa akumulacja, jak i tunelowy magnetoopór znikają.

W rozdziale 3 zaprezentowano wyniki numeryczne dotyczące transportu przez układy zbudowane z dwóch wysp, sprzężonych z sobą i z zewnętrznymi elektrodami za pomocą barier tunelowych. Analizę przeprowadzono w oparciu o metodę opisaną w rozdziale 2. W szczególności, w podrozdziale 3.2 rozpatrzono transport przez układ złożony z dwóch ferromagnetycznych wysp oraz niemagnetycznych elektrod w limicie krótkiego czasu relaksacji spinowej na wyspach. Pokazano między innymi, że tego typu układy mogą służyć jako elementy magnetooporowe, w których wielkość tunelowego magnetooporu jest kontrolowana przez przyłożone napięcia bramkujące. Jeżeli czas spinowej relaksacji jest dłuższy niż czas pomiędzy sukcesywnymi aktami tunelowania, na wyspie może pojawić się spinowa akumulacja. W analizie spinowa akumulacja na wyspach została policzona metodą samozgodną z odpowiedniego równania balansu dla prądów spinowych. Wyniki numeryczne dla szeregu różnych konfiguracji układu zostały przedstawione i omówione w podrozdziale 3.3. W szczególności, w przypadku układu złożonego z niemagnetycznych wysp i magnetycznych elektrod pokazano, że spinowa akumulacja na wyspach prowadzi do różnicy między prądami płynącymi przez układ w konfiguracji równoległej i antyrównoległej, która jest źródłem wystąpienia tunelowego magnetooporu. Tunelowy magnetoopór oscyluje w funkcji napięcia transportowego, zmieniając znak w zależności od przyłożonego napięcia. Ponadto, amplituda tych oscylacji maleje wraz ze wzrostem napięcia. Wartością tunelowego magnetooporu można dodatkowo sterować poprzez odpowiednio przyłożone napięcia bramek. Charakterystyki transportowe układu składającego się z dwóch magnetycznych wysp i niemagnetycznych elektrod w limicie długiego czasu relaksacji spinowej wykazują kolejne ciekawe efekty, mianowicie nierównowagowa akumulacja spinowa prowadzi do pojawienia się ujemnej konduktancji różniczkowej. Jak pokazano w podrozdziale 3.3, ujemna konduktancja różniczkowa może wystąpić zarówno w konfiguracji równoległej, jak i antyrównoległej, ponadto konduktancję można zmieniać przez przyłożenie napięć bramkujących. Badania eksperymentalne przeprowadzone w ostatnich latach [42, 43, 54, 69, 80] pokazały, że w strukturach granularnych, które teoretycznie mogą być modelowane między innymi przez potrójne złącza tunelowe, pojawia się efekt ujemnej kondunktancji różniczkowej oraz oscylacje tunelowego magnetooporu między ujemnymi i dodatnimi wartościami w funkcji napięcia transportowego. Zasugerowano, iż efekty te mogą wynikać z nierównowagowej akumulacji spinowej. Wyniki numeryczne przedstawione w podrozdziale 3.3 pokazują, że w występowaniu wyżej wymienionych efektów zasadniczą rolę odgrywa właśnie akumulacja spinowa. Jeżeli czas relaksacji spinowej staje się krótszy od czasu pomiędzy kolejnymi aktami tunelowania, zarówno ujemna kondunktancja różniczkowa, jak i ujemne wartości

tunelowego magnetooporu znikają. Dodatkowo, w podrozdziale 3.4 pokazano, że układy zbudowane z dwóch sprzężonych z sobą wysp mogą służyć do pompowania elektronów z określoną orientacją spinu. Proces pompowania można otrzymać poprzez przyłożenie zmiennych w czasie napięć bramkujących, przesuniętych odpowiednio w fazie.

Spinowo spolaryzowany transport przez jednopoziomowe kropki kwantowe sprzężone z ferromagnetycznymi elektrodami został przeanalizowany w drugiej części niniejszej rozprawy. W rozdziale 4 przedstawiono wyniki dotyczące sytuacji, gdy momenty magnetyczne zewnętrznych elektrod są ustawione kolinearnie. Natomiast teoretyczna analiza transportu przez kropki kwantowe w przypadku, gdy magnetyzacje elektrod są ustawione pod dowolnym kątem względem siebie, jest zawarta w rozdziale 5.

W przypadku konfiguracji kolinearnych model analizowanego układu został przedstawiony w podrozdziale 4.1. Rozważania zostały przeprowadzone w oparciu o technikę diagramową, którą opisano w podrozdziale 4.2. Technika diagramowa uwzględnia poprawnie efekty związane z renormalizacją poziomu energetycznego kropki kwantowej, jego sprzężenia z elektrodami, oraz pozwala na analizę transportu w pełnym zakresie parametrów, zarówno w obszarze liniowej, jak i nieliniowej odpowiedzi. W obliczeniach uwzględniono energie własne pierwszego i drugiego rzędu ze względu na procesy tunelowe. Wyrażenia analityczne na odpowiednie energie własne zostały przedstawione w dodatku A. Ponadto, pokazano, iż w obszarze głębokiej blokady kulombowskiej, gdzie dominujący wkład do prądu pochodzi od procesów tunelowych drugiego rzędu, transport może być alternatywnie policzony przy pomocy metody Averina-Nazarova. Metoda ta polega na obliczeniu częstotliwości tunelowania ze złotej reguły Fermiego w drugim rzędzie rachunku zaburzeń, podczas gdy prawdopodobieństwa obsadzenia poziomu kropki kwantowej są liczone z odpowiedniego równania typu "master". Metoda Averina-Nazarova opisana została w podrozdziale 4.3.

Wyniki numeryczne ukazujące zależność prawdopodobieństwa obsadzenia poziomu kropki kwantowej, prądu, konduktancji różniczkowej oraz tunelowego magnetooporu od przyłożonego napięcia transportowego oraz położenia poziomu kropki przedstawiono w podrozdziale 4.4. W celu pokazania wpływu procesów kotunelowania na charakterystyki transportowe, pokrótce przeanalizowany został przypadek kropki kwantowej sprzężonej z niemagnetycznymi elektrodami. Na otrzymanych rysunkach wyraźnie widać, że, po pierwsze, procesy tunelowe drugiego rzędu dają niezerowy wkład do konduktancji w obszarze blokady kulombowskiej. Po drugie, powodują one renormalizację położenia poziomu energetycznego kropki oraz, po trzecie, prowadzą do lekkiego rozmycia schodków kulombowskich. Podobne efekty występują także w sytuacji, gdy zewnętrzne elektrody są magnetyczne. Jednakże w tym przypadku układ wykazuje szereg kolejnych efektów związanych z dodatkowym, spinowym stopniem swobody. W szczególności, pokazano, że w obszarze liniowej odpowiedzi poziom kropki może ulec efektywnemu rozszczepieniu. Dla symetrycznego układu rozszczepienie to

występuje w konfiguracji równoległej i jest wynikiem różnicy w sprzężeniu poziomu kropki kwantowej dla elektronów o różnych kierunkach spinów. Rozszczepienie poziomu kropki jest widoczne w prawdopodobieństwie obsadzenia kropki kwantowej po uwzględnieniu procesów tunelowych drugiego rzędu.

Ponadto, pokazano, że uwzględnienie procesów tunelowych drugiego rzędu prowadzi do znacznej modyfikacji tunelowego magnetooporu w obszarze blokady kulombowskiej. W szczególności, tunelowy magnetoopór w obszarze liniowej odpowiedzi zależy od liczby elektronów obsadzających kropkę kwantową: dla nieparzystej liczby elektronów tunelowy magnetoopór jest znacznie mniejszy w porównaniu z tunelowym magnetooporem w przypadku, gdy kropka jest obsadzona przez parzystą liczbę elektronów, gdzie tunelowy magnetoopór osiąga wartość odpowiadającą wartości Jullière'a. Tak duża wartość tunelowego magnetooporu wynika stąd, że w przypadku parzystej liczby elektronów na kropce prąd płynie głównie dzięki procesom elastycznym, które są w pełni koherentne i nie zmieniają stanu kropki kwantowej. Natomiast w przypadku kropki obsadzonej nieparzystą liczbą elektronów, prąd płynie nie tylko dzięki procesom elastycznym, ale także wskutek procesów nieelastycznych, które prowadzą do obniżenia wartości tunelowego magnetooporu. Efekt parzystości tunelowego magnetooporu jest stosunkowo ciekawy z aplikacyjnego punktu widzenia. Poprzez przyłożenie napięcia bramkującego możliwa jest zmiana liczby elektronów obsadzających kropkę oraz, konsekwentnie, tunelowego magnetooporu. Z kolei w obszarze nieliniowej odpowiedzi tunelowy magnetoopór wykazuje charakterystyczne minimum w zakresie niskiego napięcia transportowego i wzrasta wraz ze wzrostem napięcia osiągając wartość Jullière'a dla $|eV| \gg k_\mathrm{B}T$. Minimum w tunelowym magnetooporze wynika bezpośrednio z anomalnego zachowania konduktancji różniczkowej w konfiguracji antyrównoległej, która wykazuje maksimum w limicie zerowego napięcia transportowego.

Podstawowe własności i charakterystyki dotyczące anomalii w konduktancji różniczkowej w przypadku, gdy magnetyzacje elektrod tworzą konfigurację antyrównoległą, są tematem podrozdziału 4.5. Maksimum w konduktancji różniczkowej występuje w konfiguracji antyrównoległej i znika w konfiguracji równoległej. Anomalne zachowanie konduktancji różniczkowej wynika z wzajemnego oddziaływania oraz pewnego rodzaju współzawodnictwa pomiędzy jednozłączowymi a dwuzłączowymi procesami kotunelowania. W limicie niskiego napięcia transportowego procesy jednozłączowe redukują spinową akumulację i powodują odblokowanie kanału przewodnictwa dla szybkich procesów dwuzłączowych, w których udział biorą tylko elektrony większościowe. Fakt ten prowadzi efektywnie do wzrostu konduktancji różniczkowej dla $|eV| < k_\mathrm{B}T$. Jeżeli natomiast $|eV| > k_\mathrm{B}T$, procesy jednozłączowe pełnią znikomą rolę, co prowadzi do spadku konduktancji. Gdy układ znajduje się w zewnętrznym polu magnetycznym, poziom kropki kwantowej ulega rozszczepieniu. W takim przypadku procesy drugiego rzędu powodujące zmianę stanu kropki są zablokowane dla $|eV| < |\Delta|$, co wynika z zasady zachowania energii. Prąd płynie zatem wtedy głównie dzięki procesom

elastycznym, które pozostawiają stan kropki niezmieniony. W efekcie w konduktancji różniczkowej widoczne jest głębokie i szerokie minimum, które jest obecne bez względu na konfigurację magnetyczną układu. Jeżeli energia dostarczona przez zródło napięcia jest porównywalna z energią rozszczepienia poziomu kropki kwantowej, procesy nieelastyczne zaczynają również dawać wkład do prądu, wskutek czego konduktancja wzrasta.

W podrozdziale 4.6 przeanalizowano wpływ procesów relaksacji na kropce kwantowej na charakterystyki transportowe w obszarze blokady kulombowskiej. Obliczenia oparto o metodę Averina-Nazarova, a poszczególne wyrażenia analityczne na odpowiednie częstotliwości tunelowania przedstawiono w dodatku B.1. Rozpatrzone zostały dwa przypadki: pierwszy dotyczy kropki kwantowej symetrycznie sprzężonej z elektrodami, drugi natomiast – kropki kwantowej niesymetrycznie sprzężonej z elektrodami zewnętrznymi. W pierwszej sytuacji pokazano, że zarówno anomalne zachowanie konduktancji różniczkowej w konfiguracji antyrównoległej, jak i minimum w tunelowym magnetooporze zależą od czasu relaksacji spinowej na kropce i w limicie szybkiego czasu relaksacji wyżej wymienione efekty znikają. Ponadto, w granicy szybkiej relaksacji tunelowy magnetoopór osiąga ujemną wartość. Jeżeli kropka kwantowa jest niesymetrycznie sprzężona z elektrodami, charakterystyki transportowe wykazują cechy typowe dla diod: konduktancja jest silnie asymetryczna względem zerowego napięcia transportowego. Ponadto, pokazano, że jeśli chodzi o układy niesymetryczne, maksimum w kondunktancji różniczkowej istnieje także w przypadku, gdy tylko jedna z elektrod jest magnetyczna, podczas gdy druga jest niemagnetyczna. Natomiast w limicie szybkiej relaksacji spinowej zarówno asymetria względem zerowego napięcia transportowego, jak i anomalne zachowanie kondunktancji różniczkowej znikają.

Spinowo spolaryzowany transport w obszarze blokady kulombowskiej przez kropki kwantowe sprzężone z ferromagnetycznymi elektrodami, których magnetyzacje tworzą dowolną konfigurację, został przeanalizowany w rozdziale 5. Rozważania zostały przeprowadzone w oparciu o metodę Averina-Nazarova, którą opisano w podrozdziale 5.1. Wzory analityczne wyrażające odpowiednie częstotliwości tunelowania przedstawiono w dodatku B.2. W obliczeniach założono, że poziom kropki kwantowej jest rozszczepiony wskutek oddziaływania z polem molekularnym pochodzącym od magnetycznego podłoża, co pozwoliło zaniedbać wkład pochodzący od procesów pierwszego rzędu odpowiedzialnych za oddziaływanie wymienne. Wyniki numeryczne dotyczące transportu drugiego rzędu w przypadku, gdy kropka kwantowa jest pusta, zostały przedstawione w podrozdziale 5.2. Pokazano, że efekt tunelowego magnetooporu silnie zależy od kąta pomiędzy magnetyzacjami zewnętrznych elektrod. Z kolei zależność kątową tunelowego magnetooporu oraz konduktancji różniczkowej w przypadku kropki kwantowej obsadzonej przez jeden elektron przeanalizowano w podrozdziale 5.3. W szczególności, przedstawiono zależność asymetrii względem zerowego napięcia transportowego od wzajemnego ustawienia magnetyzacji elektrod. Ponadto, pokazano, że efekt tunelowego magnetooporu może zostać zwiększony poprzez rozszcze-

pienie poziomu kropki kwantowej. Ponadto, szczegółowo przeanalizowano wpływ konfiguracji magnetycznej układu i rozszczepienia poziomu kropki kwantowej na kondunktancję różniczkową i efekt blokady procesów nieelastycznych dla $|eV| < |\Delta|$.

Appendix A

Self-Energies in the First and Second Order

In order to find the zeroth-order and first-order probabilities, one needs to determine all the self-energies of the first and second order in the dot-lead coupling strength Γ. In this appendix we present the explicit expressions for the first-order and second-order self-energies. Furthermore, an exemplary calculation of one of the second-order self-energies, namely, $\Sigma^{(2)}_{\bar{\sigma}\sigma}$ is also demonstrated.

A.1 First-Order Self-Energies

Using the diagrammatic rules in energy space listed in subsection 4.2.4, for the self-energies in the first order in the dot-lead coupling strength Γ one finds

$$\Sigma^{(1)}_{00} = -2\pi i \sum_{\sigma} \sum_{r} \gamma_r^{+\sigma}(\varepsilon_\sigma) \,, \tag{A.1}$$

$$\Sigma^{(1)}_{0\sigma} = 2\pi i \sum_{r} \gamma_r^{-\sigma}(\varepsilon_\sigma) \,, \tag{A.2}$$

$$\Sigma^{(1)}_{\sigma 0} = 2\pi i \sum_{r} \gamma_r^{+\sigma}(\varepsilon_\sigma) \,, \tag{A.3}$$

$$\Sigma^{(1)}_{\sigma\sigma} = -2\pi i \sum_{r} \left[\gamma_r^{-\sigma}(\varepsilon_\sigma) + \gamma_r^{+\bar{\sigma}}(\varepsilon_{\bar{\sigma}} + U) \right] \,, \tag{A.4}$$

$$\Sigma^{(1)}_{\sigma \mathrm{d}} = 2\pi i \sum_{r} \gamma_r^{-\bar{\sigma}}(\varepsilon_{\bar{\sigma}} + U) \,, \tag{A.5}$$

$$\Sigma^{(1)}_{\mathrm{d}\sigma} = 2\pi i \sum_{r} \gamma_r^{+\bar{\sigma}}(\varepsilon_{\bar{\sigma}} + U) \,, \tag{A.6}$$

$$\Sigma^{(1)}_{\mathrm{dd}} = -2\pi i \sum_{\sigma} \sum_{r} \gamma_r^{-\bar{\sigma}}(\varepsilon_{\bar{\sigma}} + U) \,, \tag{A.7}$$

119

for $r = \mathrm{L}, \mathrm{R}$. The other first-order self-energies, namely, $\Sigma_{0\mathrm{d}}^{(1)}$, $\Sigma_{\mathrm{d}0}^{(1)}$ and $\Sigma_{\bar{\sigma}\sigma}^{(1)}$ are equal to zero. This is because transitions between the states $|0\rangle$ and $|\mathrm{d}\rangle$, $|\sigma\rangle$ and $|\bar{\sigma}\rangle$ can take place only by higher-order tunneling processes. A useful identity for calculating the self-energies is $\sum_{\chi} \Sigma_{\chi\chi'} = 0$.

From the self-energies contributing to electric current only $\Sigma_{0\sigma}^{\mathrm{I}(1)}$, $\Sigma_{\sigma0}^{\mathrm{I}(1)}$, $\Sigma_{\sigma\mathrm{d}}^{\mathrm{I}(1)}$, $\Sigma_{\mathrm{d}\sigma}^{\mathrm{I}(1)}$ give nonzero contributions. They are given by

$$\Sigma_{\sigma0}^{\mathrm{I}(1)} = 2\pi i \left[\gamma_{\mathrm{L}}^{+\sigma}(\varepsilon_\sigma) - \gamma_{\mathrm{R}}^{+\sigma}(\varepsilon_\sigma) \right] , \tag{A.8}$$

$$\Sigma_{0\sigma}^{\mathrm{I}(1)} = -2\pi i \left[\gamma_{\mathrm{L}}^{-\sigma}(\varepsilon_\sigma) - \gamma_{\mathrm{R}}^{-\sigma}(\varepsilon_\sigma) \right] , \tag{A.9}$$

$$\Sigma_{\mathrm{d}\sigma}^{\mathrm{I}(1)} = 2\pi i \left[\gamma_{\mathrm{L}}^{+\bar{\sigma}}(\varepsilon_{\bar{\sigma}} + U) - \gamma_{\mathrm{R}}^{+\bar{\sigma}}(\varepsilon_{\bar{\sigma}} + U) \right] , \tag{A.10}$$

$$\Sigma_{\sigma\mathrm{d}}^{\mathrm{I}(1)} = -2\pi i \left[\gamma_{\mathrm{L}}^{-\bar{\sigma}}(\varepsilon_{\bar{\sigma}} + U) - \gamma_{\mathrm{R}}^{-\bar{\sigma}}(\varepsilon_{\bar{\sigma}} + U) \right] . \tag{A.11}$$

Using the above expressions one can calculate the zeroth-order occupation probabilities from Eq. (4.15) and then the current using Eq. (4.18).

A.2   Second-Order Self-Energies

In the following, we present an exemplary calculation of the second-order self-energy $\Sigma_{\bar{\sigma}\sigma}^{(2)}$. The equation for $\Sigma_{\bar{\sigma}\sigma}^{(2)}$ can be graphically expressed as

$$\tag{A.12}$$

To calculate the self-energy, it is necessary to evaluate each contributing diagram. As an example, we demonstrate the calculation of the third diagram of Eq. (A.12). Following the general rules described in subsection 4.2.4, the corresponding contribution, denoted as Λ_3, is given by

$$\Lambda_3 = (-1)^{2+1}(-1)^1 \sum_{r,r'=\mathrm{L},\mathrm{R}} \iint d\omega_1 d\omega_2 \gamma_r^{-\sigma}(\omega_1) \gamma_{r'}^{+\bar{\sigma}}(\omega_2) \frac{1}{\omega_1 - \varepsilon_\sigma + i0^+}$$

$$\times \frac{1}{\omega_1 + \omega_2 - \varepsilon_\sigma - \varepsilon_{\bar{\sigma}} - U + i0^+} \frac{1}{\omega_2 - \varepsilon_{\bar{\sigma}} + i0^+} , \tag{A.13}$$

The first (second) factor on the right-hand side follows from the rule 4 (5) and there are also three resolvents according to the rule 3, see subsection 4.2.4. Among various diagrams contributing to $\Sigma_{\bar{\sigma}\sigma}^{(2)}$, there is a diagram, eleventh in Eq. (A.12), whose contribution is equal to minus complex conjugate of the contribution due to the third diagram, $\Lambda_{11} = -\mathrm{Re}(\Lambda_3) + i\mathrm{Im}(\Lambda_3)$. This can be shown by interchanging the backward and forward propagators and changing the direction of tunneling lines. As a consequence, the real parts of these diagrams cancel, whereas the imaginary parts add to each other. Thus, it is necessary to determine only the imaginary part of one of those two diagrams, $\Lambda_3 + \Lambda_{11} = 2i\mathrm{Im}(\Lambda_3)$. Finally, after calculating contributions of all diagrams appearing in Eq. (A.12), one gets

$$
\begin{aligned}
\Sigma_{\bar{\sigma}\sigma}^{(2)} \;=\; & -2\pi i \sum_{r,r'} \Bigg\{ \gamma_r^{-\sigma}(\varepsilon_\sigma)B_{2r'}^{+\bar{\sigma}} + \gamma_r^{+\bar{\sigma}}(\varepsilon_{\bar{\sigma}})B_{2r'}^{-\sigma} \\
& + \gamma_r^{-\sigma}(\varepsilon_\sigma + U)C_{2r'}^{+\bar{\sigma}} + \gamma_r^{+\bar{\sigma}}(\varepsilon_{\bar{\sigma}} + U)C_{2r'}^{-\sigma} \\
& + (2\pi)^{-1} f_{\mathrm{B}}(\varepsilon_{\bar{\sigma}} - \varepsilon_\sigma + \mu_r - \mu_{r'}) \left[\Gamma_r^\sigma \left(B_{2r'}^{+\bar{\sigma}} + C_{2r'}^{+\bar{\sigma}} + 2U^{-1}A_{1r'}^{+\bar{\sigma}} \right) \right. \\
& \left. - \Gamma_{r'}^{\bar{\sigma}} \left(B_{2r}^{+\sigma} + C_{2r}^{+\sigma} + 2U^{-1}A_{1r}^{+\sigma} \right) \right] \Bigg\} ,
\end{aligned}
\tag{A.14}
$$

with $f_{\mathrm{B}}(x)$ being the Bose-Einstein distribution function, $f_{\mathrm{B}}(x) = 1/\left[\exp(x/k_{\mathrm{B}}T) - 1\right]$. The corresponding coefficients are defined as, $A_{nr}^{\pm\sigma} = B_{nr}^{\pm\sigma} - C_{nr}^{\pm\sigma}$, and

$$
B_{nr}^{\pm\sigma} = \frac{\Gamma_r^\sigma}{2\pi} \int d\omega \frac{f^{\pm}(\omega - \mu_r)}{(\omega - \varepsilon_\sigma)^n} ,
\tag{A.15}
$$

$$
C_{nr}^{\pm\sigma} = \frac{\Gamma_r^\sigma}{2\pi} \int d\omega \frac{f^{\pm}(\omega - \mu_r)}{(\omega - \varepsilon_\sigma - U)^n} ,
\tag{A.16}
$$

with f^+ being the Fermi function and $f^- = 1 - f^+$. The above integrals can be solved using the contour integration technique and the Lorentzian cutoff function of the form

$$
g_r(\omega) = \mathrm{W}^2 / \left[(\omega - \mu_r)^2 + \mathrm{W}^2 \right] ,
\tag{A.17}
$$

with W being the cutoff parameter, see appendix B.1. Equations (A.15) and (A.15) can be then expressed as

$$
B_{n+1r}^{\pm\sigma} = \pm \frac{\Gamma_r^\sigma}{2\pi} \frac{d^{(n)}}{d\varepsilon_\sigma^{(n)}} \mathrm{Re}\left[\Psi\left(\frac{1}{2} + i\frac{\varepsilon_\sigma - \mu_r}{2\pi k_{\mathrm{B}}T} \right) - \ln\left(\frac{\mathrm{W}}{2\pi k_{\mathrm{B}}T} \right) \right],
\tag{A.18}
$$

$$
C_{n+1r}^{\pm\sigma} = \pm \frac{\Gamma_r^\sigma}{2\pi} \frac{d^{(n)}}{d\varepsilon_\sigma^{(n)}} \mathrm{Re}\left[\Psi\left(\frac{1}{2} + i\frac{\varepsilon_\sigma + U - \mu_r}{2\pi k_{\mathrm{B}}T} \right) - \ln\left(\frac{\mathrm{W}}{2\pi k_{\mathrm{B}}T} \right) \right],
\tag{A.19}
$$

where $\Psi(z)$ is the digamma function. As contribution coming from a single diagram may depend on W, the final result does not. In the calculations the cutoff parameter was taken to be equal to 100Γ.

In order to calculate the occupation probabilities and the second-order current, one needs to find all the corresponding self-energies of the second order in tunneling processes. The other second-order self-energies are given by

$$
\begin{aligned}
\Sigma_{00}^{(2)} &= -2\pi i \sum_{\sigma} \sum_{r,r'} \Bigg\{ \left[(2\pi)^{-1}\Gamma_r^{\sigma} + \gamma_r^{+\bar{\sigma}}(\varepsilon_{\bar{\sigma}}) \right] B_{2r'}^{+\sigma} - \gamma_r^{+\sigma}(\varepsilon_{\sigma}) C_{2r'}^{+\bar{\sigma}} \\
&\quad - \left\{ \partial \left[\gamma_r^{+\sigma}(\varepsilon_{\sigma}) \right] + 2U^{-1}\gamma_r^{+\sigma}(\varepsilon_{\sigma}) \right\} A_{1r'}^{+\bar{\sigma}} - (2\pi)^{-1} f_{\mathrm{B}}(\varepsilon_{\mathrm{d}} - \mu_r - \mu_{r'}) \\
&\quad \times \left[\Gamma_r^{\sigma} \left(C_{2r'}^{+\bar{\sigma}} + U^{-1} A_{1r'}^{+\bar{\sigma}} \right) + \Gamma_{r'}^{\bar{\sigma}} \left(B_{2r}^{+\sigma} + U^{-1} A_{1r}^{+\sigma} \right) \right] \Bigg\},
\end{aligned}
\tag{A.20}
$$

$$
\begin{aligned}
\Sigma_{\sigma 0}^{(2)} &= 2\pi i \sum_{r,r'} \Bigg\{ \left[(2\pi)^{-1}\Gamma_r^{\sigma} + \gamma_r^{+\bar{\sigma}}(\varepsilon_{\bar{\sigma}}) + \gamma_r^{+\bar{\sigma}}(\varepsilon_{\bar{\sigma}} + U) \right] B_{2r'}^{+\sigma} \\
&\quad - \left\{ \partial \left[\gamma_r^{+\sigma}(\varepsilon_{\sigma}) \right] + 2U^{-1}\gamma_r^{+\sigma}(\varepsilon_{\sigma}) \right\} A_{1r'}^{+\bar{\sigma}} \Bigg\},
\end{aligned}
\tag{A.21}
$$

$$
\begin{aligned}
\Sigma_{\mathrm{d}0}^{(2)} &= -2\pi i \sum_{\sigma} \sum_{r,r'} \Bigg\{ \gamma_r^{+\bar{\sigma}}(\varepsilon_{\bar{\sigma}} + U) B_{2r'}^{+\sigma} + \gamma_r^{+\sigma}(\varepsilon_{\sigma}) C_{2r'}^{+\bar{\sigma}} + (2\pi)^{-1} f_{\mathrm{B}}(\varepsilon_{\mathrm{d}} - \mu_r - \mu_{r'}) \\
&\quad \times \left[\Gamma_r^{\sigma} \left(C_{2r'}^{+\bar{\sigma}} + U^{-1} A_{1r'}^{+\bar{\sigma}} \right) + \Gamma_{r'}^{\bar{\sigma}} \left(B_{2r}^{+\sigma} + U^{-1} A_{1r}^{+\sigma} \right) \right] \Bigg\},
\end{aligned}
\tag{A.22}
$$

$$
\begin{aligned}
\Sigma_{0\mathrm{d}}^{(2)} &= -2\pi i \sum_{\sigma} \sum_{r,r'} \Bigg\{ \gamma_r^{-\sigma}(\varepsilon_{\sigma} + U) B_{2r'}^{-\bar{\sigma}} + \gamma_r^{-\bar{\sigma}}(\varepsilon_{\bar{\sigma}}) C_{2r'}^{-\sigma} - (2\pi)^{-1} f_{\mathrm{B}}(\mu_r + \mu_{r'} - \varepsilon_{\mathrm{d}}) \\
&\quad \times \left[\Gamma_r^{\sigma} \left(C_{2r'}^{+\bar{\sigma}} + U^{-1} A_{1r'}^{+\bar{\sigma}} \right) + \Gamma_{r'}^{\bar{\sigma}} \left(B_{2r}^{+\sigma} + U^{-1} A_{1r}^{+\sigma} \right) \right] \Bigg\},
\end{aligned}
\tag{A.23}
$$

$$
\begin{aligned}
\Sigma_{\sigma \mathrm{d}}^{(2)} &= 2\pi i \sum_{r,r'} \Bigg\{ \left[(2\pi)^{-1}\Gamma_r^{\bar{\sigma}} + \gamma_r^{-\sigma}(\varepsilon_{\sigma}) + \gamma_r^{-\sigma}(\varepsilon_{\sigma} + U) \right] C_{2r'}^{-\bar{\sigma}} \\
&\quad + \left\{ \partial \left[\gamma_r^{-\bar{\sigma}}(\varepsilon_{\bar{\sigma}} + U) \right] - 2U^{-1}\gamma_r^{-\bar{\sigma}}(\varepsilon_{\bar{\sigma}} + U) \right\} A_{1r'}^{-\sigma} \Bigg\},
\end{aligned}
\tag{A.24}
$$

$$
\begin{aligned}
\Sigma_{\mathrm{dd}}^{(2)} &= -2\pi i \sum_{\sigma} \sum_{r,r'} \Bigg\{ \left[(2\pi)^{-1}\Gamma_r^{\bar{\sigma}} + \gamma_r^{-\sigma}(\varepsilon_{\sigma} + U) \right] C_{2r'}^{-\bar{\sigma}} - \gamma_r^{-\sigma}(\varepsilon_{\sigma} + U) B_{2r'}^{-\bar{\sigma}} \\
&\quad + \left\{ \partial \left[\gamma_r^{-\sigma}(\varepsilon_{\sigma} + U) \right] - 2U^{-1}\gamma_r^{-\sigma}(\varepsilon_{\sigma} + U) \right\} A_{1r'}^{-\bar{\sigma}} + (2\pi)^{-1} f_{\mathrm{B}}(\mu_r + \mu_{r'} - \varepsilon_{\mathrm{d}}) \\
&\quad \times \left[\Gamma_r^{\sigma} \left(C_{2r'}^{+\bar{\sigma}} + U^{-1} A_{1r'}^{+\bar{\sigma}} \right) + \Gamma_{r'}^{\bar{\sigma}} \left(B_{2r}^{+\sigma} + U^{-1} A_{1r}^{+\sigma} \right) \right] \Bigg\},
\end{aligned}
\tag{A.25}
$$

$$
\begin{aligned}
\Sigma_{0\sigma}^{(2)} \;=\; 2\pi i \sum_{r,r'} \Big\{ &\left[(2\pi)^{-1}\Gamma_r^\sigma + \gamma_r^{+\bar\sigma}(\varepsilon_{\bar\sigma}) + \gamma_r^{+\bar\sigma}(\varepsilon_{\bar\sigma}+U) \right] B_{2r'}^{-\sigma} \\
&- \left\{ \partial\left[\gamma_r^{-\sigma}(\varepsilon_\sigma) \right] + 2U^{-1}\gamma_r^{-\sigma}(\varepsilon_\sigma) \right\} A_{1r'}^{+\bar\sigma} \Big\},
\end{aligned}
\tag{A.26}
$$

$$
\begin{aligned}
\Sigma_{\sigma\sigma}^{(2)} \;=\; -2\pi i \sum_{r,r'} \Big\{ &(2\pi)^{-1}\Gamma_r^\sigma B_{2r'}^{-\sigma} + (2\pi)^{-1}\Gamma_r^{\bar\sigma} C_{2r'}^{+\bar\sigma} + \gamma_r^{+\bar\sigma}(\varepsilon_{\bar\sigma}+U)A_{2r'}^{-\sigma} - \gamma_r^{-\sigma}(\varepsilon_\sigma)A_{2r'}^{+\bar\sigma} \\
&+ \left\{ \partial\left[\gamma_r^{+\bar\sigma}(\varepsilon_{\bar\sigma}+U) \right] - 2U^{-1}\gamma_r^{+\bar\sigma}(\varepsilon_{\bar\sigma}+U) \right\} A_{1r'}^{-\sigma} \\
&- \left\{ \partial\left[\gamma_r^{-\sigma}(\varepsilon_\sigma) \right] + 2U^{-1}\gamma_r^{-\sigma}(\varepsilon_\sigma) \right\} A_{1r'}^{+\bar\sigma} \\
&- (2\pi)^{-1}f_{\mathrm{B}}(\varepsilon_{\bar\sigma}-\varepsilon_\sigma+\mu_r-\mu_{r'}) \left[\Gamma_r^\sigma \left(B_{2r'}^{+\bar\sigma}+C_{2r'}^{+\bar\sigma}+2U^{-1}A_{1r'}^{+\bar\sigma} \right) \right. \\
&\left. - \Gamma_{r'}^{\bar\sigma} \left(B_{2r}^{+\sigma}+C_{2r}^{+\sigma}+2U^{-1}A_{1r}^{+\sigma} \right) \right] \Big\},
\end{aligned}
\tag{A.27}
$$

$$
\begin{aligned}
\Sigma_{\mathrm{d}\sigma}^{(2)} \;=\; 2\pi i \sum_{r,r'} \Big\{ &\left[(2\pi)^{-1}\Gamma_r^{\bar\sigma} + \gamma_r^{-\sigma}(\varepsilon_\sigma) + \gamma_r^{-\sigma}(\varepsilon_\sigma+U) \right] C_{2r'}^{+\bar\sigma} \\
&+ \left\{ \partial\left[\gamma_r^{+\bar\sigma}(\varepsilon_{\bar\sigma}+U) \right] - 2U^{-1}\gamma_r^{+\bar\sigma}(\varepsilon_{\bar\sigma}+U) \right\} A_{1r'}^{-\sigma} \Big\}.
\end{aligned}
\tag{A.28}
$$

In the case of the second-order self-energies that contribute to the current we found $\Sigma_{\chi\chi}^{\mathrm{I}(2)}=0$, for $\chi=0,\uparrow,\downarrow,\mathrm{d}$. This is however only the case for the current operator defined as $\hat{I}=(\hat{I}_{\mathrm{R}}-\hat{I}_{\mathrm{L}})/2$, where $\hat{I}_r$ is the current operator for electrons tunneling to the lead r. The other self-energies contributing to electric current read

$$
\begin{aligned}
\Sigma_{\sigma 0}^{\mathrm{I}(2)} \;=\; 2\pi i \sum_{r} \Big\{ &\left[(2\pi)^{-1}\Gamma_r^\sigma + \gamma_r^{+\bar\sigma}(\varepsilon_{\bar\sigma}) + \gamma_r^{+\bar\sigma}(\varepsilon_{\bar\sigma}+U) \right] \left(B_{2\mathrm{L}}^{+\sigma} - B_{2\mathrm{R}}^{+\sigma} \right) \\
&- \left\{ \partial\left[\gamma_{\mathrm{L}}^{+\sigma}(\varepsilon_\sigma) - \gamma_{\mathrm{R}}^{+\sigma}(\varepsilon_\sigma) \right] \right. \\
&\left. + 2U^{-1}\left[\gamma_{\mathrm{L}}^{+\sigma}(\varepsilon_\sigma) - \gamma_{\mathrm{R}}^{+\sigma}(\varepsilon_\sigma) \right] \right\} A_{1r}^{+\bar\sigma} \Big\},
\end{aligned}
\tag{A.29}
$$

$$
\Sigma_{0\sigma}^{\mathrm{I}(2)} \;=\; \Sigma_{\sigma 0}^{\mathrm{I}(2)} + 2iU^{-1}\sum_{r}\left(\Gamma_{\mathrm{L}}^\sigma - \Gamma_{\mathrm{R}}^\sigma \right) A_{1r}^{+\bar\sigma},
\tag{A.30}
$$

$$
\begin{aligned}
\Sigma_{\mathrm{d}\sigma}^{\mathrm{I}(2)} \;=\; 2\pi i \sum_{r} \Big\{ &\left[(2\pi)^{-1}\Gamma_r^{\bar\sigma} + \gamma_r^{-\sigma}(\varepsilon_\sigma) + \gamma_r^{-\sigma}(\varepsilon_\sigma+U) \right] \left(C_{2\mathrm{L}}^{+\bar\sigma} - C_{2\mathrm{R}}^{+\bar\sigma} \right) \\
&+ \left\{ \partial\left[\gamma_{\mathrm{L}}^{+\bar\sigma}(\varepsilon_{\bar\sigma}+U) - \gamma_{\mathrm{R}}^{+\bar\sigma}(\varepsilon_{\bar\sigma}+U) \right] \right. \\
&\left. - 2U^{-1}\left[\gamma_{\mathrm{L}}^{+\bar\sigma}(\varepsilon_{\bar\sigma}+U) - \gamma_{\mathrm{R}}^{+\bar\sigma}(\varepsilon_{\bar\sigma}+U) \right] \right\} A_{1r}^{-\sigma} \Big\},
\end{aligned}
\tag{A.31}
$$

$$\Sigma_{\sigma d}^{I(2)} = \Sigma_{d\sigma}^{I(2)} + 2iU^{-1}\sum_r \left(\Gamma_L^{\bar{\sigma}} - \Gamma_R^{\bar{\sigma}}\right) A_{1r}^{-\sigma}, \tag{A.32}$$

$$\begin{aligned}
\Sigma_{d0}^{I(2)} =\ & -4\pi i \sum_\sigma \Bigg\{ \gamma_L^{+\bar{\sigma}}(\varepsilon_{\bar{\sigma}} + U)B_{2L}^{+\sigma} - \gamma_R^{+\bar{\sigma}}(\varepsilon_{\bar{\sigma}} + U)B_{2R}^{+\sigma} + \gamma_L^{+\sigma}(\varepsilon_\sigma)C_{2L}^{+\bar{\sigma}} - \gamma_R^{+\sigma}(\varepsilon_\sigma)C_{2R}^{+\bar{\sigma}} \\
& + (2\pi)^{-1}f_B(\varepsilon_d - 2\mu_L)\left[\Gamma_L^\sigma\left(B_{2L}^{+\bar{\sigma}} + C_{2L}^{+\bar{\sigma}}\right) + 2U^{-1}\Gamma_L^\sigma A_{1L}^{+\bar{\sigma}}\right] \\
& - (2\pi)^{-1}f_B(\varepsilon_d - 2\mu_R)\left[\Gamma_R^\sigma\left(B_{2R}^{+\bar{\sigma}} + C_{2R}^{+\bar{\sigma}}\right) + 2U^{-1}\Gamma_R^\sigma A_{1R}^{+\bar{\sigma}}\right] \Bigg\}, \tag{A.33}
\end{aligned}$$

$$\begin{aligned}
\Sigma_{0d}^{I(2)} =\ & -4\pi i \sum_\sigma \Bigg\{ \gamma_R^{-\sigma}(\varepsilon_\sigma + U)B_{2R}^{-\bar{\sigma}} - \gamma_L^{-\sigma}(\varepsilon_\sigma + U)B_{2L}^{-\bar{\sigma}} + \gamma_R^{-\sigma}(\varepsilon_{\bar{\sigma}})C_{2R}^{-\sigma} - \gamma_L^{-\sigma}(\varepsilon_{\bar{\sigma}})C_{2L}^{-\sigma} \\
& + (2\pi)^{-1}f_B(2\mu_L - \varepsilon_d)\left[\Gamma_L^\sigma\left(B_{2L}^{+\bar{\sigma}} + C_{2L}^{+\bar{\sigma}}\right) + 2U^{-1}\Gamma_L^\sigma A_{1L}^{+\bar{\sigma}}\right] \\
& - (2\pi)^{-1}f_B(2\mu_R - \varepsilon_d)\left[\Gamma_R^\sigma\left(B_{2R}^{+\bar{\sigma}} + C_{2R}^{+\bar{\sigma}}\right) + 2U^{-1}\Gamma_R^\sigma A_{1R}^{+\bar{\sigma}}\right] \Bigg\}, \tag{A.34}
\end{aligned}$$

$$\begin{aligned}
\Sigma_{\bar{\sigma}\sigma}^{I(2)} =\ & -4\pi i \Bigg\{ \gamma_R^{-\sigma}(\varepsilon_\sigma)B_{2L}^{+\bar{\sigma}} - \gamma_L^{-\sigma}(\varepsilon_\sigma)B_{2R}^{+\bar{\sigma}} + \gamma_L^{+\bar{\sigma}}(\varepsilon_{\bar{\sigma}})B_{2R}^{-\sigma} - \gamma_R^{+\bar{\sigma}}(\varepsilon_{\bar{\sigma}})B_{2L}^{-\sigma} \\
& + \gamma_L^{+\bar{\sigma}}(\varepsilon_{\bar{\sigma}} + U)C_{2R}^{-\sigma} - \gamma_R^{+\bar{\sigma}}(\varepsilon_{\bar{\sigma}} + U)C_{2L}^{-\sigma} + \gamma_R^{-\sigma}(\varepsilon_\sigma + U)C_{2L}^{+\bar{\sigma}} - \gamma_L^{-\sigma}(\varepsilon_\sigma + U)C_{2R}^{+\bar{\sigma}} \\
& + (2\pi)^{-1}f_B(\varepsilon_{\bar{\sigma}} - \varepsilon_\sigma + \mu_L - \mu_R)\left[\Gamma_R^{\bar{\sigma}}\left(B_{2L}^{+\sigma} + C_{2L}^{+\sigma} + 2U^{-1}A_{1L}^{+\sigma}\right)\right. \\
& \left. - \Gamma_L^\sigma\left(B_{2R}^{+\bar{\sigma}} + C_{2R}^{+\bar{\sigma}} + 2U^{-1}A_{1R}^{+\bar{\sigma}}\right)\right] \\
& - (2\pi)^{-1}f_B(\varepsilon_{\bar{\sigma}} - \varepsilon_\sigma + \mu_R - \mu_L)\left[\Gamma_L^{\bar{\sigma}}\left(B_{2R}^{+\sigma} + C_{2R}^{+\sigma} + 2U^{-1}A_{1R}^{+\sigma}\right)\right. \\
& \left. - \Gamma_R^\sigma\left(B_{2L}^{+\bar{\sigma}} + C_{2L}^{+\bar{\sigma}} + 2U^{-1}A_{1L}^{+\bar{\sigma}}\right)\right] \Bigg\}. \tag{A.35}
\end{aligned}$$

Having determined the expressions for the first-order and second-order self-energies, one can solve the master equations, Eqs. (4.15) and (4.16), to get the corresponding zeroth-order and first-order occupation probabilities. Then, the result can be plugged into Eqs. (4.18) and (4.19) to calculate the first-order and second-order electric current flowing through the system.

Appendix B

Cotunneling Rates

In this appendix we present the explicit expressions for cotunneling rates determined within the second-order perturbation theory. Using the calculated rates one can find the corresponding occupation probabilities from the appropriate master equation, Eq. (4.28). This approach may be used alternatively to the real-time diagrammatic technique in the case of deep Coulomb blockade regime, i.e., when the effects due to the first-order processes are exponentially suppressed.

B.1 Collinear Magnetic Configurations

The spin-flip cotunneling processes can take place through one of the two virtual states in which the dot is either empty ($|0\rangle$) or doubly occupied ($|d\rangle$), respectively. The corresponding energies are $\varepsilon_0 = 0$ for the empty state and $\varepsilon_d = \varepsilon_\uparrow + \varepsilon_\downarrow + U$ for the doubly occupied state. The spin-flip cotunneling rate for transition from lead r to lead r' with a change of the dot state from $|\sigma\rangle$ to $|\bar\sigma\rangle$ is given by

$$
\begin{aligned}
\gamma_{rr',\sigma\Rightarrow\bar\sigma} &= \frac{2\pi}{\hbar} \iint d\omega_1 d\omega_2 \rho_{r\bar\sigma}\rho_{r'\sigma}|t_{r\bar\sigma}|^2|t_{r'\sigma}|^2 f(\omega_1)[1 - f(\omega_2)] \\
&\times \left[\frac{1}{\omega_2 - \varepsilon_\sigma + \mu_{r'}} - \frac{1}{\omega_1 - \varepsilon_{\bar\sigma} - U + \mu_r} \right]^2 \\
&\times \delta(\omega_1 - \omega_2 + \varepsilon_\sigma - \varepsilon_{\bar\sigma} + \mu_r - \mu_{r'}).
\end{aligned} \tag{B.1}
$$

Using Eq. (4.4) and properties of the delta function Eq. (B.1) becomes

$$
\begin{aligned}
\gamma_{rr',\sigma\Rightarrow\bar\sigma} &= \frac{\Gamma_r^{\bar\sigma}\Gamma_{r'}^{\sigma}}{2\pi\hbar} \int d\omega\, f(\omega)[1 - f(\omega + \varepsilon_\sigma - \varepsilon_{\bar\sigma} + \mu_r - \mu_{r'})] \\
&\times \left[\frac{1}{\omega - \varepsilon_{\bar\sigma} + \mu_r} - \frac{1}{\omega - \varepsilon_{\bar\sigma} - U + \mu_r} \right]^2.
\end{aligned} \tag{B.2}
$$

Then, by taking into account the identity

$$
f(\omega)[1 - f(\omega + \xi')] = f_B(-\xi')[f(\omega + \xi') - f(\omega)], \tag{B.3}
$$

Eq. (B.2) can be rewritten as a sum of integrals of type $\int d\omega f(\omega)/(\omega - \xi)^n$ $(n = 1, 2, \dots)$. In principal, it is necessary to determine the integrals for $n = 1$, whereas the ones for $n > 1$ can be found from the following identity

$$\int d\omega \frac{f(\omega)}{(\omega - \xi)^{n+1}} = \frac{1}{n!} \frac{d^{(n)}}{d^{(n)}\xi} \int d\omega \frac{f(\omega)}{\omega - \xi} . \tag{B.4}$$

Below we demonstrate the calculation of one of the summands, namely

$$J = \int d\omega \frac{f(\omega)}{\omega - \varepsilon_{\bar{\sigma}} + \mu_r} . \tag{B.5}$$

To calculate this integral we use the Lorentzian cutoff given by Eq. (A.17). Consequently, Eq. (B.5) can be expressed as

$$\begin{aligned} J &= \frac{W}{2i} \int d\omega \frac{f(\omega)}{(\omega - \varepsilon_{\bar{\sigma}} + \mu_r)(\omega - \mu_r - iW)} \\ &\quad - \frac{W}{2i} \int d\omega \frac{f(\omega)}{(\omega - \varepsilon_{\bar{\sigma}} + \mu_r)(\omega - \mu_r + iW)} . \end{aligned} \tag{B.6}$$

The first (second) integral in the above formula has poles at $\omega = \varepsilon_{\bar{\sigma}} - \mu_r$, $\omega = \mu_r + (-)iW$, and $\omega = i(2m+1)\pi$, with $m = 0, 1, 2, \dots$. However, because we are interested in the deep Coulomb blockade regime (where the second-order processes dominate), it is justifiable to assume $\omega \ll \varepsilon_{\bar{\sigma}}$ and this way neglect the contribution of the first pole. Then, by means of the contour integration and assuming W to be the largest energy scale, one gets

$$J = \text{Re}\Psi\left(\frac{1}{2} + i\frac{\varepsilon_{\bar{\sigma}} - \mu_r}{2\pi k_{\text{B}}T}\right) - \ln\left(\frac{W}{2\pi k_{\text{B}}T}\right) . \tag{B.7}$$

As a single integral depends on the cutoff parameter, the total rate does not. The expressions depending on W cancel in pairs, which can be simply seen from Eq. (B.3). The other summands of Eq. (B.2) can be found in a similar way with the aid of the above mentioned identities. Then, the spin-flip cotunneling rate reads

$$\begin{aligned} \gamma_{rr',\sigma\Rightarrow\bar{\sigma}} &= \frac{\Gamma_r^{\bar{\sigma}}\Gamma_{r'}^{\sigma}}{2\pi\hbar} f_B(\mu_{r'} - \mu_r - \varepsilon_{\sigma} + \varepsilon_{\bar{\sigma}})\left[\mathcal{B}_{2r'}^{\sigma} - \mathcal{B}_{2r}^{\bar{\sigma}} + \mathcal{C}_{2r'}^{\sigma} - \mathcal{C}_{2r}^{\bar{\sigma}} \right. \\ &\quad \left. + 2U^{-1}\left(\mathcal{B}_{1r'}^{\sigma} - \mathcal{B}_{1r}^{\bar{\sigma}} - \mathcal{C}_{1r'}^{\sigma} + \mathcal{C}_{1r}^{\bar{\sigma}}\right)\right] , \end{aligned} \tag{B.8}$$

with the coefficients defined as

$$\mathcal{B}_{n+1r}^{\sigma} = \frac{d^{(n)}}{d\varepsilon_{\sigma}^{(n)}}\text{Re}\Psi\left(\frac{1}{2} + i\frac{\varepsilon_{\sigma} - \mu_r}{2\pi k_{\text{B}}T}\right) , \tag{B.9}$$

$$\mathcal{C}_{n+1r}^{\sigma} = \frac{d^{(n)}}{d\varepsilon_{\sigma}^{(n)}}\text{Re}\Psi\left(\frac{1}{2} + i\frac{\varepsilon_{\sigma} + U - \mu_r}{2\pi k_{\text{B}}T}\right) . \tag{B.10}$$

126

The rate of a non-spin-flip process when the dot is in the state $|\sigma\rangle$ and an electron with spin σ co-tunnels through the system is given by

$$\gamma^{\sigma}_{rr',\sigma\Rightarrow\sigma} = \frac{\Gamma^{\sigma}_{r}\Gamma^{\sigma}_{r'}}{2\pi\hbar} \int d\omega f(\omega)[1 - f(\omega + \mu_r - \mu_{r'})] \left(\frac{1}{\omega - \varepsilon_{\sigma} + \mu_r}\right)^2, \quad \text{(B.11)}$$

whereas the rate in the case when a single electron with spin σ resides on the dot while another one with spin $\bar{\sigma}$ co-tunnels through the system reads

$$\gamma^{\bar{\sigma}}_{rr',\sigma\Rightarrow\sigma} = \frac{\Gamma^{\bar{\sigma}}_{r}\Gamma^{\bar{\sigma}}_{r'}}{2\pi\hbar} \int d\omega f(\omega)[1 - f(\omega + \mu_r - \mu_{r'})] \left(\frac{1}{\omega - \varepsilon_{\bar{\sigma}} + U + \mu_r}\right)^2. \quad \text{(B.12)}$$

The above expressions can be calculated in a similar way as Eq. (B.2), then, the non-spin-flip cotunneling rate when the dot is in state $|\sigma\rangle$ is

$$\gamma_{rr',\sigma\Rightarrow\sigma} = \frac{f_B(\mu_{r'} - \mu_r)}{2\pi\hbar} \left[\Gamma^{\sigma}_{r}\Gamma^{\sigma}_{r'} (\mathcal{B}^{\sigma}_{2r'} - \mathcal{B}^{\sigma}_{2r}) + \Gamma^{\bar{\sigma}}_{r}\Gamma^{\bar{\sigma}}_{r'} (\mathcal{C}^{\bar{\sigma}}_{2r'} - \mathcal{C}^{\bar{\sigma}}_{2r})\right]. \quad \text{(B.13)}$$

Using the calculated rates one can determine the occupation probabilities from Eq. (4.28) and then the electric current from Eq. (4.30).

B.2   Noncollinear Magnetic Configurations

In this section we present the cotunneling rates in the case when the leads are magnetized noncollinearly. In this situation, there may be nonzero matrix elements for transitions that were not allowed in the case when the magnetic moments of the leads formed a collinear configuration.

B.2.1   Case of Empty Dot

In the case of empty dot the current is mediated only by non-spin-flip cotunneling processes. The transition rate for electrons tunneling from the majority spin band in the lead r to the majority spin band in the lead r' is given by

$$\begin{aligned} \gamma^{+\Rightarrow+}_{rr',0\Rightarrow0} &= \frac{\Gamma^{+}_{r}\Gamma^{+}_{r'}}{2\pi\hbar} \int d\omega f(\omega)[1 - f(\omega + \mu_r - \mu_{r'})] \\ &\times \left[\frac{\cos\left(\varphi_r/2\right)\cos\left(\varphi_{r'}/2\right)}{\omega + \mu_r - \varepsilon_{\uparrow}} + \frac{\sin\left(\varphi_r/2\right)\sin\left(\varphi_{r'}/2\right)}{\omega + \mu_r - \varepsilon_{\downarrow}}\right]^2, \quad \text{(B.14)} \end{aligned}$$

The integrals in Eq. (B.14) can be calculated quite easily using the contour integration method, as described in previous section. Following this procedure one finds

$$\begin{aligned} \gamma^{+\Rightarrow+}_{rr',0\Rightarrow0} &= \frac{\Gamma^{+}_{r}\Gamma^{+}_{r'}}{2\pi\hbar} f_B(\mu_{r'} - \mu_r) \left[\cos^2\frac{\varphi_r}{2}\cos^2\frac{\varphi_{r'}}{2}(\mathcal{B}^{\uparrow}_{2r'} - \mathcal{B}^{\uparrow}_{2r}) \right. \\ &+ \sin^2\frac{\varphi_r}{2}\sin^2\frac{\varphi_{r'}}{2}(\mathcal{B}^{\downarrow}_{2r'} - \mathcal{B}^{\downarrow}_{2r}) \\ &\left. + \frac{\sin\varphi_r\sin\varphi_{r'}}{2(\varepsilon_{\uparrow} - \varepsilon_{\downarrow})}\left(\mathcal{B}^{\uparrow}_{1r'} - \mathcal{B}^{\uparrow}_{1r} - \mathcal{B}^{\downarrow}_{1r'} + \mathcal{B}^{\downarrow}_{1r}\right)\right], \quad \text{(B.15)} \end{aligned}$$

127

with the coefficients given by Eqs. (B.9) and (B.10). The other cotunneling rates when a majority ($\sigma = +$) or minority ($\sigma = -$) electron of the lead r co-tunnels to the majority ($\sigma = +$) or minority ($\sigma = -$) electron band of the lead r' are given by

$$
\begin{aligned}
\gamma_{rr',0\Rightarrow0}^{+\Rightarrow-} = &\ \frac{\Gamma_r^+ \Gamma_{r'}^-}{2\pi\hbar} f_{\mathrm{B}}(\mu_{r'} - \mu_r) \left[\cos^2 \frac{\varphi_r}{2} \sin^2 \frac{\varphi_{r'}}{2} (\mathcal{B}_{2r'}^\uparrow - \mathcal{B}_{2r}^\uparrow) \right. \\
&+ \sin^2 \frac{\varphi_r}{2} \cos^2 \frac{\varphi_{r'}}{2} (\mathcal{B}_{2r'}^\downarrow - \mathcal{B}_{2r}^\downarrow) \\
&\left. - \frac{\sin\varphi_r \sin\varphi_{r'}}{2(\varepsilon_\uparrow - \varepsilon_\downarrow)} \left(\mathcal{B}_{1r'}^\uparrow - \mathcal{B}_{1r}^\uparrow - \mathcal{B}_{1r'}^\downarrow + \mathcal{B}_{1r}^\downarrow \right) \right] ,
\end{aligned}
\tag{B.16}
$$

$$
\begin{aligned}
\gamma_{rr',0\Rightarrow0}^{-\Rightarrow+} = &\ \frac{\Gamma_r^- \Gamma_{r'}^+}{2\pi\hbar} f_{\mathrm{B}}(\mu_{r'} - \mu_r) \left[\sin^2 \frac{\varphi_r}{2} \cos^2 \frac{\varphi_{r'}}{2} (\mathcal{B}_{2r'}^\uparrow - \mathcal{B}_{2r}^\uparrow) \right. \\
&+ \cos^2 \frac{\varphi_r}{2} \sin^2 \frac{\varphi_{r'}}{2} (\mathcal{B}_{2r'}^\downarrow - \mathcal{B}_{2r}^\downarrow) \\
&\left. - \frac{\sin\varphi_r \sin\varphi_{r'}}{2(\varepsilon_\uparrow - \varepsilon_\downarrow)} \left(\mathcal{B}_{1r'}^\uparrow - \mathcal{B}_{1r}^\uparrow - \mathcal{B}_{1r'}^\downarrow + \mathcal{B}_{1r}^\downarrow \right) \right] ,
\end{aligned}
\tag{B.17}
$$

$$
\begin{aligned}
\gamma_{rr',0\Rightarrow0}^{-\Rightarrow-} = &\ \frac{\Gamma_r^- \Gamma_{r'}^-}{2\pi\hbar} f_{\mathrm{B}}(\mu_{r'} - \mu_r) \left[\sin^2 \frac{\varphi_r}{2} \sin^2 \frac{\varphi_{r'}}{2} (\mathcal{B}_{2r'}^\uparrow - \mathcal{B}_{2r}^\uparrow) \right. \\
&+ \cos^2 \frac{\varphi_r}{2} \cos^2 \frac{\varphi_{r'}}{2} (\mathcal{B}_{2r'}^\downarrow - \mathcal{B}_{2r}^\downarrow) \\
&\left. + \frac{\sin\varphi_r \sin\varphi_{r'}}{2(\varepsilon_\uparrow - \varepsilon_\downarrow)} \left(\mathcal{B}_{1r'}^\uparrow - \mathcal{B}_{1r}^\uparrow - \mathcal{B}_{1r'}^\downarrow + \mathcal{B}_{1r}^\downarrow \right) \right] .
\end{aligned}
\tag{B.18}
$$

The total rate is then given by

$$
\gamma_{rr',0\Rightarrow0} = \sum_{\sigma,\sigma'=+,-} \gamma_{rr',0\Rightarrow0}^{\sigma\Rightarrow\sigma'} .
\tag{B.19}
$$

B.2.2   Case of Singly-Occupied Dot

In the case when the dot is occupied by a single electron, the current can flow due to both the spin-flip and non-spin-flip cotunneling processes. The corresponding cotunneling rates can be calculated in a similar way as described in previous sections.

The rate of a spin-flip process which transfer a spin-majority electron from the lead r to the spin-down level of the dot and a spin-up electron from the dot to the spin-majority electron band in the lead r' is given by

$$
\begin{aligned}
\gamma_{rr',\uparrow\Rightarrow\downarrow}^{+\Rightarrow+} = &\ \frac{\Gamma_r^+ \Gamma_{r'}^+}{2\pi\hbar} \sin^2 \frac{\varphi_r}{2} \cos^2 \frac{\varphi_{r'}}{2} \int d\omega f(\omega)[1 - f(\omega + \varepsilon_\uparrow - \varepsilon_\downarrow + \mu_r - \mu_{r'})] \\
&\times \left(\frac{1}{\omega - \varepsilon_\downarrow + \mu_r} - \frac{1}{\omega - \varepsilon_\downarrow - U + \mu_r} \right)^2 .
\end{aligned}
\tag{B.20}
$$

The total rate of spin-flip cotunneling which changes the dot state from $|\uparrow\rangle$ to $|\downarrow\rangle$ can be found by summing up over the spin-majority and spin-minority electrons

$$\gamma_{rr',\uparrow\Rightarrow\downarrow} = \sum_{\sigma,\sigma'=+,-} \gamma_{rr',\uparrow\Rightarrow\downarrow}^{\sigma\Rightarrow\sigma'}, \tag{B.21}$$

then, one gets

$$
\begin{aligned}
\gamma_{rr',\uparrow\Rightarrow\downarrow} &= \frac{f_{\mathrm{B}}(\mu_{r'} - \mu_r - \varepsilon_\uparrow + \varepsilon_\downarrow)}{2\pi\hbar} \left[\Gamma_r^+ \Gamma_{r'}^+ \sin^2 \frac{\varphi_r}{2} \cos^2 \frac{\varphi_{r'}}{2} + \Gamma_r^+ \Gamma_{r'}^- \sin^2 \frac{\varphi_r}{2} \sin^2 \frac{\varphi_{r'}}{2} \right. \\
&\quad \left. + \Gamma_r^- \Gamma_{r'}^+ \cos^2 \frac{\varphi_r}{2} \cos^2 \frac{\varphi_{r'}}{2} + \Gamma_r^- \Gamma_{r'}^- \cos^2 \frac{\varphi_r}{2} \sin^2 \frac{\varphi_{r'}}{2} \right] \\
&\quad \times \left[\mathcal{B}_{2r'}^\uparrow - \mathcal{B}_{2r}^\downarrow + \mathcal{C}_{2r'}^\uparrow - \mathcal{C}_{2r}^\downarrow + 2U^{-1} \left(\mathcal{B}_{1r'}^\uparrow - \mathcal{B}_{1r}^\downarrow - \mathcal{C}_{1r'}^\uparrow + \mathcal{C}_{1r}^\downarrow \right) \right]. \tag{B.22}
\end{aligned}
$$

For the cotunneling rate which changes the dot state from $|\downarrow\rangle$ to $|\uparrow\rangle$ one finds

$$
\begin{aligned}
\gamma_{rr',\downarrow\Rightarrow\uparrow} &= \frac{f_{\mathrm{B}}(\mu_{r'} - \mu_r + \varepsilon_\uparrow - \varepsilon_\downarrow)}{2\pi\hbar} \left[\Gamma_r^+ \Gamma_{r'}^+ \cos^2 \frac{\varphi_r}{2} \sin^2 \frac{\varphi_{r'}}{2} + \Gamma_r^+ \Gamma_{r'}^- \cos^2 \frac{\varphi_r}{2} \cos^2 \frac{\varphi_{r'}}{2} \right. \\
&\quad \left. + \Gamma_r^- \Gamma_{r'}^+ \sin^2 \frac{\varphi_r}{2} \sin^2 \frac{\varphi_{r'}}{2} + \Gamma_r^- \Gamma_{r'}^- \sin^2 \frac{\varphi_r}{2} \cos^2 \frac{\varphi_{r'}}{2} \right] \\
&\quad \times \left[\mathcal{B}_{2r'}^\downarrow - \mathcal{B}_{2r}^\uparrow + \mathcal{C}_{2r'}^\downarrow - \mathcal{C}_{2r}^\uparrow + 2U^{-1} \left(\mathcal{B}_{1r'}^\downarrow - \mathcal{B}_{1r}^\uparrow - \mathcal{C}_{1r'}^\downarrow + \mathcal{C}_{1r}^\uparrow \right) \right]. \tag{B.23}
\end{aligned}
$$

The non-spin-flip cotunneling rate in the case when the dot is in the state $|\uparrow\rangle$ is given by

$$
\begin{aligned}
\gamma_{rr',\uparrow\Rightarrow\uparrow} &= \frac{f_{\mathrm{B}}(\mu_{r'} - \mu_r)}{2\pi\hbar} \left\{ \left(\mathcal{C}_{2r'}^\downarrow - \mathcal{C}_{2r}^\downarrow \right) \right. \\
&\quad \times \left[\Gamma_r^+ \Gamma_{r'}^+ \sin^2 \frac{\varphi_r}{2} \sin^2 \frac{\varphi_{r'}}{2} + \Gamma_r^+ \Gamma_{r'}^- \sin^2 \frac{\varphi_r}{2} \cos^2 \frac{\varphi_{r'}}{2} \right. \\
&\quad \left. + \Gamma_r^- \Gamma_{r'}^+ \cos^2 \frac{\varphi_r}{2} \sin^2 \frac{\varphi_{r'}}{2} + \Gamma_r^- \Gamma_{r'}^- \cos^2 \frac{\varphi_r}{2} \cos^2 \frac{\varphi_{r'}}{2} \right] \\
&\quad + \left(\mathcal{B}_{2r'}^\uparrow - \mathcal{B}_{2r}^\uparrow \right) \left[\Gamma_r^+ \Gamma_{r'}^+ \cos^2 \frac{\varphi_r}{2} \cos^2 \frac{\varphi_{r'}}{2} + \Gamma_r^+ \Gamma_{r'}^- \cos^2 \frac{\varphi_r}{2} \sin^2 \frac{\varphi_{r'}}{2} \right. \\
&\quad \left. + \Gamma_r^- \Gamma_{r'}^+ \sin^2 \frac{\varphi_r}{2} \cos^2 \frac{\varphi_{r'}}{2} + \Gamma_r^- \Gamma_{r'}^- \sin^2 \frac{\varphi_r}{2} \sin^2 \frac{\varphi_{r'}}{2} \right] \\
&\quad - \frac{\sin^2 \varphi_r \sin^2 \varphi_{r'}}{2 (\varepsilon_\downarrow - \varepsilon_\uparrow + U)} \left(\mathcal{C}_{1r'}^\downarrow - \mathcal{C}_{1r}^\downarrow - \mathcal{B}_{1r'}^\uparrow + \mathcal{B}_{1r}^\uparrow \right) \\
&\quad \left. \times \left(\Gamma_r^+ \Gamma_{r'}^+ - \Gamma_r^+ \Gamma_{r'}^- - \Gamma_r^- \Gamma_{r'}^+ + \Gamma_r^- \Gamma_{r'}^- \right) \right\}, \tag{B.24}
\end{aligned}
$$

whereas the non-spin-flip cotunneling rate in the case when the dot is in the state

$|\downarrow\rangle$ reads

$$
\begin{aligned}
\gamma_{rr',\downarrow\Rightarrow\downarrow} \;=\; & \frac{f_{\mathrm{B}}(\mu_{r'}-\mu_r)}{2\pi\hbar}\Bigg\{\left(\mathcal{C}^{\uparrow}_{2r'}-\mathcal{C}^{\uparrow}_{2r}\right) \\
& \times\Bigg[\Gamma^{+}_{r}\Gamma^{+}_{r'}\cos^2\frac{\varphi_r}{2}\cos^2\frac{\varphi_{r'}}{2}+\Gamma^{+}_{r}\Gamma^{-}_{r'}\cos^2\frac{\varphi_r}{2}\sin^2\frac{\varphi_{r'}}{2} \\
& +\Gamma^{-}_{r}\Gamma^{+}_{r'}\sin^2\frac{\varphi_r}{2}\cos^2\frac{\varphi_{r'}}{2}+\Gamma^{-}_{r}\Gamma^{-}_{r'}\sin^2\frac{\varphi_r}{2}\sin^2\frac{\varphi_{r'}}{2}\Bigg] \\
& +\left(\mathcal{B}^{\downarrow}_{2r'}-\mathcal{B}^{\downarrow}_{2r}\right)\Bigg[\Gamma^{+}_{r}\Gamma^{+}_{r'}\sin^2\frac{\varphi_r}{2}\sin^2\frac{\varphi_{r'}}{2}+\Gamma^{+}_{r}\Gamma^{-}_{r'}\sin^2\frac{\varphi_r}{2}\cos^2\frac{\varphi_{r'}}{2} \\
& +\Gamma^{-}_{r}\Gamma^{+}_{r'}\cos^2\frac{\varphi_r}{2}\sin^2\frac{\varphi_{r'}}{2}+\Gamma^{-}_{r}\Gamma^{-}_{r'}\cos^2\frac{\varphi_r}{2}\cos^2\frac{\varphi_{r'}}{2}\Bigg] \\
& -\frac{\sin^2\varphi_r\sin^2\varphi_{r'}}{2\left(\varepsilon_{\uparrow}-\varepsilon_{\downarrow}+U\right)}\left(\mathcal{C}^{\uparrow}_{1r'}-\mathcal{C}^{\uparrow}_{1r}-\mathcal{B}^{\downarrow}_{1r'}+\mathcal{B}^{\downarrow}_{1r}\right) \\
& \times\left(\Gamma^{+}_{r}\Gamma^{+}_{r'}-\Gamma^{+}_{r}\Gamma^{-}_{r'}-\Gamma^{-}_{r}\Gamma^{+}_{r'}+\Gamma^{-}_{r}\Gamma^{-}_{r'}\right)\Bigg\},
\end{aligned}
\tag{B.25}
$$

where the corresponding coefficients are given by Eqs. (B.9) and (B.10). Using the expressions for the second-order rates, one can calculate the occupation probabilities from Eq. (4.28) and, then, the electric current flowing through system from Eq. (4.30).

Bibliography

[1] J. J. Thomson, Philosophical Magazine **44**, 293 (1897).

[2] R. A. Millikan, Phys. Rev. **32**, 349 (1911).

[3] D. V. Averin, K. K. Likharev, in *Mesoscopic Phenomenon in Solids*, ed. by B. L. Altshuler, P. A. Lee, R. A. Webb (Amsterdam: North-Holland 1991).

[4] *Single Charge Tunneling: Coulomb Blockade Phenomena in Nanostructures*, NATO ASI Series B: Physics 294, ed. by H. Grabert, M. H. Devoret (Plenum Press, New York 1992).

[5] S. Datta, *Electronic Transport in Mesoscopic Systems* (Cambridge University Press, 1995).

[6] D. K. Ferry and S. M. Goodnick, *Transport in Nanostructures* (Cambridge University Press, 1997).

[7] L. P. Kouwenhoven, C. M. Marcus, P. L. McEuen, S. Tarucha, R. M. Westervelt, and N. S. Wingreen, in Proceedings of the NATO Advanced Study Institute on Mesoscopic Electron Transport, ed. by L. L. Sohn, L. P. Kouwenhoven, and G. Schön (Kluwer Series E345, 1997).

[8] G. Schön, in Chapter 3 of *Quantum Transport and Dissipation*, T. Dittrich, P. Haenggi, G. Ingold, B. Kramer, G. Schön and W. Zwerger (Wiley-VCH Verlag, 1998).

[9] K. K. Likharev, *Single-electron devices and their applications*, Proceedings of the IEEE **87**, 606 (1999).

[10] T. Heinzel, *Mesoscopic Electronics in Solid State Nanostructures* (Wiley-VCH, 2003).

[11] G. E. Uhlenbeck and S. Goudsmit, Naturwissenschaften **47**, 953 (1925).

[12] P. A. M. Dirac, Proc. Roy. Soc. A **117**, 610 (1928).

[13] S. A. Wolf, D. D. Awschalom, R. A. Buhrman, J. M. Daughton, S. von Molnar, M. L. Roukes, A. Y. Chtchelkanova, D. M. Treger, Science **294**, 1488 (2001).

[14] J. F. Gregg, I. Petej, E. Jouguelet, and C. Dennis, J. Phys. D: Appl. Phys. **35**, R121 (2002).

[15] S. Maekawa and T. Shinjo, *Spin Dependent Transport in Magnetic Nanostructures* (Taylor & Francis 2002).

[16] *Semiconductor Spintronics and Quantum Computation*, ed. by D. D. Awschalom, D. Loss, and N. Samarth (Springer, Berlin 2002).

[17] I. Zutic, J. Fabian, S. Das Sarma, Rev. Mod. Phys. **76**, 323 (2004).

[18] M. I. Dyakonov, in *Future Trends in Microelectronics: The Nano, the Giga, and the Ultra*, ed. by S. Luryi, J. Xu, A. Zaslavsky (Wiley-IEEE Press, 2004).

[19] T. Fulton and G. Dolan, Phys. Rev. Lett. **59**, 109 (1987).

[20] K. Mullen and E. Ben-Jacob, R. C. Jaklevic, Z. Schuss, Phys. Rev. B **37**, 98 (1988).

[21] K. K. Likharev, J. Res. Develop. **32**, 144 (1988).

[22] L. J. Geerligs, V. F. Anderegg, P. A. M. Holweg, and J. E. Mooij, H. Pothier, D. Esteve, C. Urbina, and M. H. Devoret, Phys. Rev. Lett. **64**, 2691 (1990).

[23] Y. Meir, N. S. Wingreen, and P. A. Lee, Phys. Rev. Lett. **66**, 3048 (1991).

[24] Y. Meir and N. S. Wingreen, Phys. Rev. Lett. **68**, 2512 (1992).

[25] M. H. Devoret, D. Esteve and C. Urbina, Nature **360**, 547 (1992).

[26] D. V. Averin and K. K. Likharev, J. Low Temp. Phys **62**, 345 (1986).

[27] C. W. J. Beenakker, Phys. Rev. B **44**, 1646 (1991).

[28] L. P. Kouwenhoven, A. T. Johnson, N. C. van der Vaart, C. J. P. M. Harmans, and C. T. Foxon, Phys. Rev. Lett. **67**, 1626 (1991).

[29] D. V. Averin and A. A. Odintsov, Phys. Lett. A **140**, 251 (1989).

[30] D. V. Averin and Yu. V. Nazarov, Phys. Rev. Lett. **65**, 2446 (1990).

[31] L. J. Geerligs, D. V. Averin, and J. E. Mooij, Phys. Rev. Lett. **65**, 3037 (1990).

[32] J. Barnaś and A. Fert, Phys. Rev. Lett. **80**, 1058 (1998).

[33] S. Takahashi and S. Maekawa, Phys. Rev. Lett. **80**, 1758 (1998).

[34] K. Ono, H. Shimada, S. Kobayashi, and Y. Ootuka, J. Phys. Soc. Japan **65**, 3449 (1996).

[35] K. Ono, H. Shimada, and Y. Ootuka, J. Phys. Soc. Japan **66**, 1261 (1997).

[36] M. Jullière, Phys. Lett. A **54**, 225 (1975).

[37] M. A. Kastner, Rev. Mod. Phys. **64**, 849 (1992).

[38] M. Devoret and Ch. Glatti, Physics World (Sept. 1998).

[39] Yu. A. Pashkin, Y. Nakamura, and J. S. Tsai, Appl. Phys. Lett. **76**, 2256 (2000).

[40] M. M. Deshmukh and D. C. Ralph, Phys. Rev. Lett. **89**, 266 803 (2002).

[41] F. Ernult, K. Yamane, S. Mitani, K. Yakushiji, K. Takanashi, Y. K. Takahashi, K. Hono, Appl. Phys. Lett. **84**, 3106 (2004).

[42] K. Takanashi, S. Mitani, J. Chiba, and H. Fujimori, J. Appl. Phys. **87**, 6331 (2000).

[43] K. Yakushiji, S. Mitani, K. Takanashi, H. Fujimori, J. Appl. Phys. **91**, 7038 (2002).

[44] I. Weymann, *Single Electron Tunneling Devices and Magnetic Effects in Single Electron Tunneling Transistor* (Master Thesis, UAM Poznań, 2001).

[45] M. Amman, R. Wilkins, E. Ben-Jacob, P. D. Maker, and R. C. Jaklevic, Phys. Rev. B **43**, 1146 (1991).

[46] A. E. Hanna and M. Tinkham, Phys. Rev. **44**, 5919 (1991).

[47] C. B. Whan, J. White, and T. P. Orladno, Appl. Phys. Lett. **68**, 2996 (1996).

[48] K. P. Hirvi, M. A. Paalanen, and J. P. Pekola, J. Appl. Phys. **80**, 256 (1996).

[49] J. A. Melsen, U. Hanke, H.-O. Müller, and K.-A. Chao, Phys. Rev. B **55**, 10 638 (1997).

[50] H. Park, J. Park, A. K. L. Lim, E. H. Anderson, A. P. Alivisatos and P. L. McEuen, Nature **407**, 57 (2000).

[51] G. Lientschnig, I. Weymann and P. Hadley, Jpn. J. Appl. Phys. **42**, 6467 (2003).

[52] J. S. Moodera, L. R. Kinder, T. M. Wong, and R. Meservey, Phys. Rev. Lett. **74**, 3273 (1995).

[53] J. S. Moodera and L. R. Kinder, J. Appl. Phys. **79**, 4724 (1996).

[54] H. Imamura, J. Chiba, S. Mitani, K. Takanashi, S. Takahashi, S. Maekawa, and H. Fujimori, Phys. Rev. B **61**, 46 (2000).

[55] J. Barnaś and A. Fert, Europhys. Lett. **44**, 85 (1998).

[56] K. Majumdar and S. Hershfield, Phys. Rev. B **57**, 11 521 (1998).

[57] A. Brataas, Yu. V. Nazarov, J. Inoue, and G. E. W. Bauer, Eur. Phys. J. B **9**, 421 (1999).

[58] A. N. Korotkov and V. I. Safarov, Phys. Rev. B **59**, 89 (1999).

[59] J. Martinek, J. Barnaś, S. Maekawa, H. Schöller, and G. Schön, Phys. Rev. B **66**, 014 402 (2002).

[60] I. Weymann and J. Barnaś, Phys. Stat. Sol. b **236**, 651 (2003).

[61] J. Wiśniewska, I. Weymann, and J. Barnaś, Mol. Phys. Rep. **40**, 187 (2004).

[62] J. Wiśniewska, I. Weymann, and J. Barnaś, Mat. Science **22, No. 4**, 461 (2004).

[63] S. Mitani, S. Takahashi, K. Takanashi, K. Yakashiji, S. Maekawa, and H. Fujimori, Phys. Rev. Lett. **81**, 2799 (1998).

[64] W. Kuo and C. D. Chen, Phys. Rev. B **65**, 104 427 (2002).

[65] I. Weymann, J. Barnaś, and J. Martinek, J. Supercond. **16**, 225 (2003).

[66] J. Barnaś, V. Dugaev, S. Krompiewski, J. Martinek, W. Rudziński, R. Świrkowicz, I. Weymann, and M. Wilczyński, Phys. Stat. Sol. b **236**, 246 (2003).

[67] J. Martinek, J. Barnaś, G. Michałek, B. R. Bułka, A. Fert, J. Magn. Magn. Mater. **207**, L1 (1999).

[68] J. Barnaś, J. Martinek, G. Michałek, B. R. Bułka, A. Fert, Phys. Rev. B **62**, 12 363 (2000).

[69] K. Yakushiji, F. Ernult, H. Imamura, K. Yamane, S. Mitani, K. Takanashi, S. Takahashi, S. Maekawa, H. Fujimori, Nature Materials **4**, 57 (2005).

[70] D. Lubzens and S. Schultz, Phys. Rev. Lett. **36**, 1104 (1976).

[71] M. Johnson and R. H. Silsbee, Phys. Rev. Lett. **55**, 1790 (1985).

[72] H. Imamura, S. Takahashi, and S. Maekawa, Phys. Rev. B **59**, 6017 (1999).

[73] J. Barnaś and A. Fert, J. Magn. Magn. Mater. **192**, 391 (1999).

[74] I. Weymann and J. Barnaś, submitted to Phys. Stat. Sol.

[75] I. Weymann and J. Barnaś, J. Magn. Magn. Mater. **272**, e1477 (2004).

[76] H. Shimada and Y. Ootuka, Phys. Rev. B **64**, 235 418 (2002).

[77] W. G. van der Wiel, S. De Franceschi and J. M. Elzerman, T. Fujisawa, S. Tarucha, L. P. Kouwenhoven, Rev. Mod. Phys. **75**, 1 (2003).

[78] V. Hung Nguyen, Lien Nguyen, H. Nam Nguyen, J. Appl. Phys. **96**, 3302 (2004).

[79] K. A. Matveev, L. I. Glazman, H. U. Baranger, Phys. Rev. B **65**, 5637 (1996).

[80] K. Yakushiji, S. Mitani, K. Takanashi, S. Takahashi, S. Maekawa, H. Imamura, H. Fujimori, Appl. Phys. Lett. **78**, 515 (2001).

[81] H. Nakashima and K. Uozumi, J. Vac. Sci. Technol. B **15 No. 4 Jul/Aug**, 1411 (1997).

[82] H. Pothier, P. Lafarge, C. Urbina, D. Esteve, and M. N. Devoret, Europhys. Lett. **17**, 249 (1992).

[83] K. Tsukagoshi, K. Nakazato, H. Ahmed, K. Gamo, Phys. Rev. B **56**, 3972 (1997).

[84] M. Kastner, Phys. Today **44**, 24 (1993).

[85] L. P. Kouwenhoven, Science **268**, 5216 (1995).

[86] L. Kouwenhoven and C. Marcus, Physics World 35 (June 1998).

[87] R. Hanson, B. Witkamp, L. M. K. Vandersypen, L. H. Willems van Beveren, J. M. Elzerman, and L. P. Kouvenhoven, Phys. Rev. Lett. **91**, 196 802 (2003).

[88] Y. Meir, N. S. Wingreen, and P. A. Lee, Phys. Rev. Lett. **70**, 2601 (1993).

[89] N. S. Wingreen and Y. Meir, Phys. Rev. B **49**, 11040 (1994).

[90] B. R. Bułka, Phys. Rev. B **62**, 1186 (2000).

[91] W. Rudziński and J. Barnaś, Phys. Rev. B **64**, 085 318 (2001).

[92] A. Cottet, W. Belzig, and C. Bruder, Phys. Rev. Lett. **92**, 206 801 (2004).

[93] J. König and J. Martinek, Phys. Rev. Lett. **90**, 166 602 (2003).

[94] M. Braun, J. König, J. Martinek, Phys. Rev. B **70**, 195 345 (2004).

[95] W. Rudziński, J. Barnaś, R. Świrkowicz, and M. Wilczyński, Phys. Rev. B **71**, 205 307 (2005).

[96] S. Braig and P. W. Brouwer, cond-mat/0412592.

[97] S. De Franceschi, S. Sasaki, J. M. Elzerman, W. G. van der Wiel, S. Tarucha, and L. P. Kouvenhoven, Phys. Rev. Lett. **86**, 878 (2001).

[98] A. Kogan, S. Amasha, D. Goldhaber-Gordon, G. Granger, M. A. Kastner, and H. Shtrikman, Phys. Rev. Lett. **93**, 166 602 (2004).

[99] D. M. Zumbühl, C. M. Marcus, M. P. Hanson, and A. C. Gossard, Phys. Rev. Lett. **93**, 256 801 (2004).

[100] M. Ciorga, M. Pioro-Ladrire, P. Zawadzki, J. Lapointe, Z. Wasilewski, and A. S. Sachrajda, cond-mat/0407071.

[101] K. Kang and B. I. Min, Phys. Rev. B **55**, 15 412 (1997).

[102] J. König, *Quantum Fluctuations in the Single-Electron Transistor* (Shaker, Aachen, 1999).

[103] U. Hartmann, F. K. Wilhelm, Phys. Rev. B **67**, 161 307 (2003).

[104] I. Weymann, J. Barnaś, J. König, J. Martinek, and G. Schön, Phys. Rev. B **72**, 113 301 (2005).

[105] I. Weymann, J. König, J. Martinek, J. Barnaś and G. Schön, to be published in Phys. Rev. B.

[106] I. Weymann and J. Barnaś, cond-mat/0505449; to be published in Eur. Phys. J. B **46**, 289 (2005).

[107] R. Świrkowicz, J. Barnaś, and M. Wilczyński, J. Phys.: Condens. Matter **14**, 2011 (2002).

[108] Y. Utsumi, J. Martinek, G. Schön, H. Imamura, S. Maekawa, cond-mat/0501172.

[109] A. N. Pasupathy, R. C. Bialczak, J. Martinek, J. E. Grose, L. A. K. Donev, P. L. McEuen, and D. C. Ralph, Science **306**, 86 (2004).

[110] S. M. Cronenwett, T. H. Oosterkamp, and L. P. Kouvenhoven, Science **281**, 540 (1998).

[111] J. Gores, D. Goldhaber-Gordon, S. Heemeyer, M. A. Kastner, H. Shtrikman, D. Mahalu, and U. Meirav, Phys. Rev. B **62**, 2188 (2000).

[112] S. Sasaki, S. De Franceschi, J. M. Elzerman, W. G. van der Wiel, M. Eto, S. Tarucha, and L. P. Kouvenhoven, Nature **405**, 764 (2000).

[113] J. Martinek, Y. Utsumi, H. Imamura, J. Barnaś, S. Maekawa, J. König, and G. Schön, Phys. Rev. Lett. **91**, 127 203 (2003).

[114] R. Lopez and D. Sanchez, Phys. Rev. Lett. **90**, 116 602 (2003).

[115] J. Kondo, Prog. Theor. Phys. **32**, 37 (1964).

[116] K. G. Wilson, Rev. Mod. Phys. **47**, 773 (1975).

[117] H. R. Krishna-Murthy, J. W. Wilkins, and K. G. Wilson, Phys. Rev. B **21**, 1003 (1980).

[118] H. R. Krishna-Murthy, J. W. Wilkins, and K. G. Wilson, Phys. Rev. B **21**, 1044 (1980).

[119] Y. Chye, M. E. White, E. Johnston-Halperin, B. D. Gerardot, D. D. Awschalom, and P. M. Petroff, Phys. Rev. B **66**, 201 301(R) (2002).

[120] K. Tsukagoshi, B. W. Alphenaar, and H. Ago, Nature **401**, 572 (1999).

[121] B. Zhao, I. Mönch, H. Vinzelberg, T. Mühl, and C. M. Schneider, Appl. Phys. Lett. **80**, 3144 (2002).

[122] B. Zhao, I. Mönch, H. Vinzelberg, T. Mühl, and C. M. Schneider, J. Appl. Phys. **91**, 7026 (2002).

[123] J. Nygard, W. F. Koehl, N. Mason, L. DiCarlo, and C. M. Marcus, cond-mat/0410467.

[124] M. J. Biercuk, S. Garaj, N. Mason, J. M. Chow, C. M. Marcus, cond-mat/0502634.

[125] P. W. Anderson, Phys. Rev. **124**, 41 (1961).

[126] H. Schoeller and G. Schön, Phys. Rev. B **50**, 18 436 (1994).

[127] J. König, J. Schmid, H. Schoeller, and G. Schön, Phys. Rev. B **54**, 16 820 (1996).

[128] J. König, H. Schoeller, and G. Schön, Phys. Rev. Lett. **76**, 1715 (1996).

[129] A. Thielmann, M. H. Hettler, J. König, and G. Schön, Phys. Rev. B **68**, 165 341 (2003).

[130] J. König, J. Martinek, J. Barnas, and G. Schön, in *CFN Lectures on Functional Nanostructures*, Eds. K. Busch et al., Lecture Notes in Physics **658**, Springer, 145 (2005).

[131] I. Weymann and J. Barnaś, to be published in Physica B.

[132] N. Sergueev, Qing-feng Sun, Hong Guo, B. G. Wang, and Jian Wang, Phys. Rev. B **65**, 165 303 (2002).

[133] J. N. Pedersen, J. Q. Thomassen, and K. Flensberg, cond-mat/0412145.

[134] W. Rudziński and J. Barnaś, J. Magn. Magn. Mater. **279**, 134 (2004).

[135] J. Fransson, cond-mat/0502288.

[136] W. Rudziński, J. Barnaś, R. Świrkowicz, and M. Wilczyński, Phys. Stat. Sol. b **242**, 342 (2005).

[137] M. Wilczyński, R. Świrkowicz, W. Rudziński, J. Barnaś, V. Dugaev, J. Magn. Magn. Mater. **290**, 209 (2005).

[138] J. Fransson, O. Eriksson, and I. Sandalov, Phys. Rev. Lett. **88**, 226 601 (2002).

List of Publications

[1] I. Weymann and J. Barnaś, *Transport characteristics of ferromagnetic single-electron transistors*, Phys. Stat. Sol. b **236**, 651 (2003).

[2] I. Weymann, J. Barnaś, and J. Martinek, *Nonequilibrium magnetic polarization and spin currents controlled by gate voltage in a ferromagnetic single-electron transistor*, J. Supercond. **16**, 225 (2003).

[3] G. Lientschnig, I. Weymann and P. Hadley, *Simulating Hybrid Circuits of Single-Electron Transistors and Field-Effect Transistors*, Jpn. J. Appl. Phys. **42**, 6467 (2003).

[4] J. Barnaś, V. Dugaev, S. Krompiewski, J. Martinek, W. Rudziński, R. Świrkowicz, I. Weymann, and M. Wilczyński, *Spin related effects in magnetic mesoscopic systems*, Phys. Stat. Sol. b **236**, 246 (2003).

[5] I. Weymann and J. Barnaś, *Spin polarized cotunneling through a quantum dot*, Phys. Stat. Sol. a **196**, 113 (2003).

[6] J. Barnaś, R. Świrkowicz, M. Wilczyński, I. Weymann, J. Martinek and V. Dugaev, *Spin Polarized Transport through Quantum Dots: Coulomb Blockade and Kondo Effect*, Acta Phys. Pol. A **104**, 165 (2003).

[7] I. Weymann and J. Barnaś, *Electronic transport in ferromagnetic double-island single-electron devices*, J. Magn. Magn. Mater. **272**, e1477 (2004).

[8] J. Wiśniewska, I. Weymann, and J. Barnaś, *Transport characteristics of ferromagnetic single-electron transistors*, Mol. Phys. Rep. **40**, 187 (2004).

[9] J. Wiśniewska, I. Weymann, and J. Barnaś, *Spin-dependent transport in ferromagnetic single-electron transistors with non-collinear magnetizations*, Mat. Science **22, No. 4**, 461 (2004).

[10] I. Weymann, J. Barnaś, J. König, J. Martinek, and G. Schön, *Zero-bias anomaly in cotunneling transport through quantum-dot spin valves*, Phys. Rev. B **72**, 113 301 (2005).

[11] I. Weymann, J. König, J. Martinek, J. Barnaś and G. Schön, *Tunnel Magnetoresistance of Quantum Dots Coupled to Ferromagnetic Leads in the Sequential and Cotunneling Regimes*, to be published in Phys. Rev. B.

[12] I. Weymann and J. Barnaś, *Cotunneling through a quantum dot coupled to ferromagnetic leads with noncollinear magnetizations*, Eur. Phys. J. B **46**, 289 (2005).

[13] J. Barnaś, A. Fert, M. Gmitra, I. Weymann and V. K. Dugaev, *Macroscopic description of current induced switching due to spin-transfer*, Phys. Rev. B **72**, 024 426 (2005).

[14] J. Barnaś, A. Fert, M. Gmitra, I. Weymann and V. K. Dugaev, *Macroscopic description of spin transfer torque*, presented at EMRS 2005 Spring Meeting, Strasbourg; to be published in Mat. Sci. Eng. B.

[15] I. Weymann and J. Barnaś, *Spin-dependent transport through double-island single-electron devices*, presented at The European Conference Physics of Magnetism 2005, Poznań; submitted to Phys. Stat. Sol.

[16] M. Gmitra, J. Barnaś, A. Fert, I. Weymann, and V. K. Dugaev, *Current induced switching due to spin-transfer in spin valves: macroscopic model*, presented at The European Conference Physics of Magnetism 2005, Poznań; submitted to Phys. Stat. Sol.

[17] I. Weymann and J. Barnaś, *Cotunneling through a magnetic quantum dot coupled to ferromagnetic leads with noncollinear magnetizations*, to be presented at The International Conference on Strongly Correlated Electron Systems 2005, Vienna; to be published in Physica B.